Technical University of Denmark

**DTU**

# Incoherent Optical Frequency Domain Reflectometry for Distributed Thermal Sensing

**Karamehmedovic, Emir; Jeppesen, Palle; Peucheret, Christophe; Bjarklev, Anders Overgaard**

*Publication date:*
2006

*Document Version*
Publisher's PDF, also known as Version of record

Link back to DTU Orbit

**DTU Library**
Technical Information Center of Denmark

# Incoherent Optical Frequency Domain Reflectometry for Distributed Thermal Sensing

Emir Karamehmedović

June 2006

**COM·DTU**
Department of Communications, Optics & Materials

Technical University of Denmark
Building 345V
2800 Kgs. Lyngby
DENMARK

# Abstract

This thesis reports the main results from an investigation of a fibre-optic distributed temperature sensor based on spontaneous Raman scattering. The technique used for spatial resolving is the incoherent optical frequency domain reflectometry, where a pump laser is sine-modulated with a stepwise increasing frequency, after which the inverse Fourier transform is applied to the signal from the backscattered light. This technique is compared with the more conventional optical time domain reflectometry, where a short pulse is sent through the fibre, and the location of the scattering section is determined by the time difference from the emission to the detection of light.

A temperature sensor with a range of 2-4km comprising a step-index multi-mode fibre and a high-power 980nm pump laser existed prior to the start of the PhD study. In this study, a sensor range of approximately 10km, and a spatial resolution of order 1m is strived to be achieved. These demands are attempted to be reached by employing a low-loss telecom-grade transmission single-mode fibre or an alternative fibre as the sensing fibre, and a pump laser operating in the low-loss region of silica.

An analysis of the optical module comprising a pump laser, optical filters, optical fibre and photo-detectors are presented. Limitations, trade-offs and optimisation processes are described for setups having different specifications with respect to range, resolution and accuracy.

The analysis is conducted using computer simulation programs developed and implemented in Matlab. The computer model is calibrated and tested, and describes the entire system with high precision. Noise analysis and digital processing of the detected signal are discussed as well. An equation describing the standard deviation of the measured

temperature is derived for the device, and shows the dependency of the accuracy on measurement time, resolution, range, attenuation and detector parameters.

Temperature measurements on 7.8km low-loss graded-index multi-mode fibre and 14km standard single-mode fibre with a spatial resolution varying from 0.5m to 6m are given as representative examples of the achieved accuracy (0.5$^o$C to 5$^o$C) and range, with measurement time of a few minutes. Measurements on 25km were conducted as well to demonstrate this possibility; with a short measurement time it was not possible to obtain a reasonable accuracy though.

In addition to the Raman based temperature sensor, a quasi-distributed fibre-optic temperature and strain sensor based on an array of fibre Bragg gratings interrogated by a tuneable laser is also developed and analysed. This type of fibre-sensor is particularly suitable for strain monitoring on large concrete constructions such as bridges. The sensor is built and tested in a field trial on a bridge, and the estimated accuracy of around $2\mu\varepsilon$ is achieved.

# Resumé

I denne rapport fremlægges hovedresultaterne fra en undersøgelse af en fiber-optisk distribueret temperatur sensor baseret på spontan Raman spredning. Teknikken der er anvendt til at opnå stedlig bestemmelse er den såkaldte "Incoherent Optical Frequency Domain Reflectometry", hvor en pumpelaser moduleres med en sinusfunktion med en trinvis stigende frekvens, hvorefter omvendt Fourier transformation udføres på det målte signal fra det tilbagespredte lys. Denne teknik sammenlignes med den mere konventionelle "Optical Time Domain Reflectometry", hvor en puls sendes gennem fiberen, og stedlig opløsning fås fra tidsforskellen mellem udsendelsen og modtagelsen af lyset.

En temperatursensor med en rækkevidde på 2-4km og bestående af en multi-mode step-indeks fiber og en pumpelaser med en bølgelængde på 980nm eksisterede allerede inden starten af dette studie. I studiet er det forsøgt at designe en sensor med en rækkevidde på omkring 10km og en stedopløsning på 1m. Det er blevet undersøgt om disse krav kan opfyldes ved at bruge en single-mode lavtabs transmissionsfiber, eller en anden type fiber, samt en pumpelaser, der fungerer i lavtabs bølgelængdeområdet for silica.

Der præsenteres en analyse af det optiske modul der består af pumpelaseren, den optiske fiber, optiske filtre og fotodetektorer. Begrænsninger og optimeringsprocessen er beskrevet for opstillinger med forskellige specifikationer hvad angår rækkevidde, opløsning og nøjagtighed.

Analysen er gennemført ved hjælp af computersimulationer, der er udviklet og implementeret i Matlab. Den numeriske model er udviklet, kalibreret og testet, og den beskriver systemet med stor nøjagtighed. Støjanalyse og digital behandling af de detekterede signaler er også omtalt. En ligning der beskriver standardafvigelsen af den målte tem-

peratur er udledt for apparatet, og den viser, hvorledes nøjagtigheden afhænger af måletid, opløsning, rækkevidde, dæmpning i fiberen og detektorparametre.

Temperaturmålinger på 7.8km lavtabs gradueret-indeks multi-mode fiber og 14km standard single-mode fiber med en stedlig opløsning der varierer fra 0.5m til 6m, er givet som repræsentative eksempler på den opnåede nøjagtighed ($0.5^oC$ to $5^oC$) og rækkevidde, med måletiden på et par minutter. Målinger på 25km er også blevet udført for at demonstrere muligheden for dette; nøjagtigheden var dog begrænset.

Ydermere, en kvasi-distribueret fiber-optisk temperatur- og stress sensor baseret på en række fiber Bragg gitre, som belyses med en tunebar laser, er også blevet udviklet og analyseret. Denne sensortype er specielt egnet til overvågning af stress på store betonbygninger og broer. Sensoren er opbygget og testet på en bro, og den opnåede nøjagtighed er vurderet til $2\mu\varepsilon$.

# Acknowledgements

I would like to start by expressing special gratitude to my supervisor from NKT Research and Innovation, Ph.D. Thomas Feuchter, who engaged in this project very actively, and with whom I made most of the experimental as well as theoretical work. Likewise, I would like to thank my supervisors from $COM \bullet DTU$ Professor Dr. Techn. Palle Jeppesen, Ph.D. Christophe Peucheret and Professor Dr. Techn. Anders Bjarklev for their continuous help during the project.

I am grateful to Professor Gang Ding Peng from University of New South Wales for supervising me and making my stay in his group an instructive and enjoyable experience.

Furthermore, I thank to people at Lios Technology GmbH, especially Ph.D. Ulrich Glombitza, Dipl.Ing. Jochen Kübler and the CEO Stefan Deiser for great collaboration, discussions and help in various systems tests during my visits there.

This study was supported by Photonics Academy Denmark (previously NKT Academy).

Finally, thanks to my good friends, Hans Christian, Darko, Beata, Rasmus, Torger, Jesper and others from the department for laughs, fun and collaboration, which made the days at $COM \bullet DTU$ unforgettable.

Kgs. Lyngby 26/06/2006
Emir Karamehmedović

# List of Figures

# List of Tables

# Contents

# Chapter 1

# Introduction

Optical fibres find use in other fields than telecommunications. A very promising and expanding field is the optical fibre sensing. Distributed fibre sensors make it possible to measure e.g. temperature, stress or strain along a line that may be several kilometres long, using only a single fibre as both the sensing and information-carrying medium. The physical quantity can be measured at virtually every point in the fibre.

In this thesis, distributed temperature sensor (DTS) based on temperature dependent spontaneous Raman scattering in single-mode and multi-mode optical fibres is presented.

Compared with standard electrical sensors, the fibre-optic solution offers several significant advantages. First, a single line, i.e. the optical fibre itself, accesses the vast number of multiplexed points, which can substitute several thousand of electrical point-detectors. Second, the information is carried in the optical domain rather than the electrical, rendering the electromagnetic interference harmless for the carried data. A third advantage is the total galvanic isolation of the transducer, i.e. the fibre, from the measured medium so that direct contact with the measured object is possible.

Distributed sensors exploit the principles of localization known from radar technology. The so-called LIDAR (LIght Detection And Ranging) systems can process the received signal in the time or frequency domain, the two most common techniques being Optical Time Domain Reflectometry (OTDR) and Incoherent Optical Frequency Domain Reflectometry (IOFDR), respectively. Both techniques have advantages

and drawbacks in terms of resolution, measurement time, cost and com-
plexity. The resolution here is defined as the spacing between distin-
guishable adjacent measurement points.

In OTDR the location of the scattering section is determined by
time difference from the emission to the detection of light. This tech-
nique requires a high peak-power pulsed laser and fast electronics if high
resolution and long range are to be obtained. In IOFDR on the other
hand, a narrow line-width laser diode operates in a virtually continuous
wave regime. The laser is modulated from DC to frequencies in $MHz$
region, and a stationary modulated signal is received in the detector
for each modulation frequency. Moreover, by using IOFDR combined
with lock-in techniques, the signal-to-noise ratio (SNR) can be improved
considerably compared to OTDR [1], but the technique introduces some
complications as well. Not only the amplitudes but also the phases
of the signals need to be recorded with minimal errors, posing special
demands on electronic components. Furthermore, a relatively complex
signal processing task follows the data acquisition.

## 1.1   Distributed Temperature Sensors

A number of technologies for fibre-optic distributed temperature mea-
surements exist. For example, LIDAR systems based on OTDR Raman
scattering with a range of $10 - 30km$ and a resolution of $4 - 20m$ have
been reported [2] [3]. Simplicity of design, the availability of short-pulsed
high power lasers and photon-counting techniques make this scheme at-
tractive.

Distributed sensors based on Brillouin scattering have also been pro-
posed and tested [4]. Here, it is the frequency shift of the scattered light
that is temperature dependent. Especially the possibility to operate in
low-loss region of the silica fibre and possible use of EDFA amplifiers
make this scheme favourable in long-range systems. Ranges up to $85km$
and resolutions of $20m$ have been achieved.

Quasi-distributed combined temperature and strain sensors employ-
ing arrays of fibre Bragg gratings are already commonly used for some
applications [5]. In this scheme, the reflected or transmitted wavelength
spectrum depends on the temperature and strain.

Methods to exploit Rayleigh scattering for distributed temperature

sensing have also been found. By analysis of the reflection spectrum of the Rayleigh scattering using coherent OFDR, it is possible to detect temperature changes [6] [7].

Finally, there are fibres coated with temperature sensitive coatings, which change transmission characteristics when exposed to temperature changes [8].

All mentioned techniques have advantages and limitations compared to one another. In this work, the focus is on IOFDR spontaneous Raman systems, where it is attempted to achieve a range of approximately $10km$ and a resolution of around $1m$.

## 1.2 Overview

Chapter 2 gives the relevant properties and description of Raman scattering in optical fibres. Equations governing spontaneous and stimulated Raman scattering are developed, and there is a description of experiments conducted to measure the material parameters of various fibres.

IOFDR is described in Chapter 3. Expressions for the resolution, range and temperature profile are derived. Possible choice of channels is discussed as well.

The basic experimental setup which is used in most of the experiments is introduced in Chapter 4. Main sources of noise are identified and their respective influences on temperature measurements are determined. An important result here is the deduction of the accuracy, or standard temperature deviation of a system based on IOFDR. The technique is theoretically compared to the rivalling OTDR.

Development of the numerical model which is used to optimise the system is presented in Chapter 5. Some digital signal processing techniques used to improve the signals are described as well.

Optimisation of the optical module of the distributed temperature sensor are presented in Chapter 6. Wavelength and power of the pump laser, fibre type and modulation format are considered.

Some actual representative measurements are compared with the predictions and analysis in Chapter 7. Note, however, that some of the results were obtained prior to the optimisations.

Chapter 8 deals with fibre-optic strain and temperature sensing based on fibre Bragg gratings interrogated by a tuneable laser. The chapter

summarises development and test of the device.

Finally, main conclusions and prospectives for future work are given in Chapter 9.

The appendices contain some lengthy derivations, figures of the setup with its characteristics, descriptions and results from some less essential experiments. A part of the developed simulation program code is also given in the appendices.

# Chapter 2

# Raman Scattering

This chapter introduces the process on which the temperature fibre sensor is based i.e. the Raman scattering. Spontaneous and stimulated Raman scattering are described, and how the processes depend on temperature. The relevant material parameters for silica fibres are experimentally determined.

## 2.1 Scattering of light in a nonlinear medium

Electromagnetic waves interact in many ways with the medium in which they propagate. Maxwell's equations explain behaviour of electromagnetic waves in a medium, while the material parameters, permittivity and permeability, $\bar{\bar{\varepsilon}}$ and $\bar{\bar{\mu}}$, describe the medium. Macroscopically, it is possible to describe any material by its permittivity and permeability; for nonlinear, lossy, isotropic, homogeneous media, such as standard optical fibres, these are complex functions of wavelength or frequency are reduced to [9]:

$$
\begin{aligned}
\mu &= \mu_r(\omega) \cdot \mu_0 & (2.1) \\
\varepsilon(\omega) &= \varepsilon_0 \cdot (1 + \chi^{(1)}(\omega) + \frac{3}{4}\chi^{(3)}|E|^2) & (2.2)
\end{aligned}
$$

where $\chi^{(n)}$ is the $n^{th}$ order susceptibility. In this model, the complex function $\chi^{(1)}(\omega)$ holds information about the linear refractive index $n(\omega)$ and attenuation coefficient $\alpha(\omega)$ [10], while $\chi^{(3)}$, which is also complex,

accounts for the nonlinear part of the dielectric constant, i.e., it is dependent on the power of the propagating light.

Nonlinear interaction between light and matter is characterized by change in the frequency spectrum of the involved light, i.e., new frequency components appear in the spectrum. As contrast, linear processes, such as dispersion and attenuation, affect the propagating light only in the time domain.

The most important and common nonlinear processes in fibre-optics are self-phase modulation, four wave mixing, self-steepening, stimulated Brillouin scattering and stimulated Raman scattering. In optical fibres, the intensity and power of light do not need to be as high as in bulk materials to observe the non-linear processes. Light is confined to small core area, and the length of interaction between the medium and light may be kilometers.

In the nonlinear processes, photons exchange energy with other photons, electrons, atoms and molecules. For all processes, conservation of energy is necessary. Parametric processes maintain energy in the optical domain, while in non-parametric processes some energy is transferred to other forms. For example, in Raman and Brillouin scattering, which are forms of inelastic scattering, the energy difference is contained in optical and acoustic phonons, respectively. In this work, the Raman scattering is of particular interest.

## 2.2   The Raman effect

The possibility of occurrence of the Raman effect was predicted in 1925 by Heisenberg and Kramers [11], assuming that the irradiating particles - electrons, atoms and molecules, are in motion while scattering, or interacting with the incident light. During the interaction, exchange of energy is possible, and light at new optical frequencies may appear. The effect was confirmed experimentally in 1928 by Raman and Krishnan [12] independently of the prediction, and acquired its name Raman scattering. Mandelstam and Landsberg also independently observed the effect of inelastic light scattering [13] even earlier than Raman and Krishnan.

Mandelstam and Landsberg reported that some crystals scatter light in a way that several new lines appear in the frequency spectrum. And if the wavelength of the incident excitation light shifts, so do the excited

lines at the same rate (i.e. by the same frequency shift). This is a fundamentally different behaviour from fluorescent lines where the frequency shift is determined exclusively by the potential energy difference in electron bands of atoms. For example, potassium and mercury fluorescent lines are well defined and independent of the excitation frequency.

In the case of the Raman effect, the energy difference between the vibrational modes of the medium correspond to the energy shift of the scattered light. A pump photon can either absorb or generate an optical phonon, which adds or subtracts the phonon quantum energy to the pump photon energy, thus creating lines in the spectrum of the scattered light at lower and higher frequencies than the pump. The power contained in the optical domain is, thus, not conserved in the process. Lower frequency lines are called the Stokes lines, while the opposite lines are the anti-Stokes lines. The process is illustrated in figure 2.1.
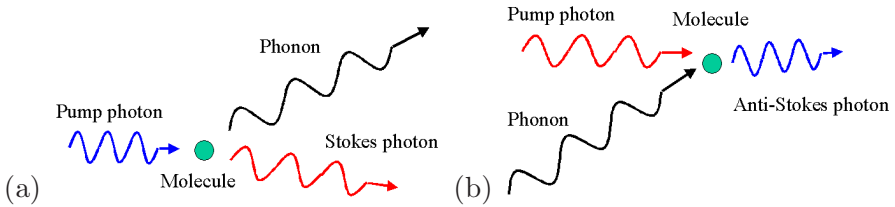


**Figure 2.1:** (a) Raman Stokes scattering, (b) Raman anti-Stokes scattering.

The probability of a Stokes photon being generated is greater than the probability of generation of an anti-Stokes photon, as a phonon of right energy and phase is required for the latter process to occur. Raman scattering can be spontaneous, where Stokes and anti-Stokes photons are created independently of other photons, or stimulated, where the transfer of photons from one line to another is due to photons already in the line of destination.

In an amorphous solid, such as fused silica, the Raman lines smear into bands (inhomogeneous broadening). The Raman gain spectrum of fused silica is shown in Figure 2.2. The Raman gain spectrum of silica peaks at the frequency shift of $13.2THz$ from the pump light, and extends almost $40THz$ in width. The Raman gain coefficient $g_R(\omega)$ is proportional to the imaginary part of the third order susceptibility $\chi_I^{(3)}(\omega)$ by which the effect is usually described [14] [15]. The Raman
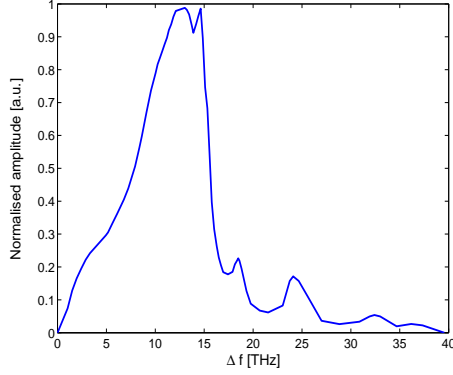
**Figure 2.2:** Normalised Raman gain spectrum in silica fibre as a function of the frequency shift from the pump [9]. The maximum is at a frequency shift of 13.2THz.

time response shows that the time-scale of Raman scattering is below $1ps$ [15]. It can therefore be assumed instantaneous for the purposes of this work.

The Raman gain spectrum of glasses is often approximated by a Lorentzian function $L(\omega)$ [15]

$$L(\omega) = A_0 \frac{\Delta\omega^2}{\Delta\omega[(\omega_0 - \omega)^2 + (\Delta\omega/2)^2]} \tag{2.3}$$

with the central frequency around $f_0 = 10.5THz$ for fused silica. This would correspond to a medium with a single vibrational mode. However, there are a number of vibrational modes in fused silica. If each of them is represented with one peak, linear combination yields the total Raman spectrum. A combination of pure Lorentzian or pure Gaussian peaks does not fit the measured curve well. But if each peak is a convolution of Gauss and Lorentz functions, the Raman gain spectrum $g(\omega)$ is matched more precisely [17]

$$g(\omega) = \sum_{j=1}^{J} \frac{a_j}{2\omega_{r,j}} \int_0^\infty [\cos((\omega_{r,j} - \omega)t) - \cos((\omega_{r,j} + \omega)t)e^{-\gamma_j t}e^{-\Gamma_j^2 t^2/4}dt \tag{2.4}$$

where $a_j$ are amplitudes, $\gamma_j$ and $\Gamma_j$ Lorentzian and Gaussian line widths of specific resonance. Sum of the first 13 resonances of silica give a good approximation of the actual Raman gain spectrum [15].

By introducing a dopant into the propagation medium, not only the refractive index is changed. The added molecules have their vibrational states and may also alter the Raman spectrum. However, in the low-loss fibres, which are of interest here, dopants have little influence on the spontaneous Raman scattering [19], as their concentration is very low and thus add oscillators with insignificant amplitude. The change of the refractive index, on the other hand, does influence some nonlinear effects, since the confinement, and thus the intensity, of light may change significantly. This issue is discussed in Chapter 6.

## 2.3 Spontaneous Raman Scattering

Equations describing the spontaneous Raman scattering are developed in the following. Spontaneously Raman scattered light depends on the power of the excitation beam $P_P$ at wavelength $\lambda_P$, and the temperature and Raman gain spectrum of the scattering medium. The probability of spontaneous Raman scattering is independent of the electromagnetic field intensity and has no preferred direction. The emission is therefore nearly isotropic [20]. The power of the scattered light $P_s$ at $\lambda_s$ can be written as

$$P_s(\lambda_s, T) = \frac{\lambda_P}{\lambda_s} P_P \cdot \Psi \cdot N(\Delta f, T) \qquad (2.5)$$

where $\Psi$ is the material dependent proportionality constant and $N(\Delta f, T)$, where $\Delta f$ equals the oscillation frequency of the phonon $\omega_{ph}/2\pi$ is proportional to the number of phonons available for interaction at temperature $T$. Usually, it is necessary to include polarization dependence of the Raman scattering. If the excitation beam is linearly polarised (or decomposed into linearly polarised components) one can define [21]

$$\Psi \propto \frac{\pi^2}{2\hbar\varepsilon_0^2} \frac{n_s}{n_P} \frac{1}{\lambda_s^3 \lambda_P} \Big( M_{||}(\Delta f)\cos^2(\theta) + M_{\perp}(\Delta f)\sin^2(\theta) \Big) \qquad (2.6)$$

where $\theta$ is the angle between the direction of the electric fields of the excitation and the scattered light. $n_P$ and $n_s$ are refractive indices at the pump and scattered light wavelengths. Introduction of $M_{||}$ and $M_{\perp}$ accounts for the difference in the parallel and perpendicular portion of the scattered light. In the following, however, scattering media will be

fibres which do not maintain polarisation, and the scattered signal is thus not differentiated with respect to the polarisation.

In silica fibres which do not preserve the polarisation, the scattering cross-section is by an order of magnitude higher for polarisation parallel to the excitation light $P_{||}$ than for the perpendicular $P_\perp$, i.e., $M_{||} >> M_\perp$ [21]. The average of the two coefficients is taken, and it is in silica fibres with good approximation $M_{||}/2$.

Having the simplification of disregarding the polarisation dependence, equation (2.5) becomes

$$P_s(\lambda_s, T) = \frac{\kappa n_s}{n_P \lambda_s^4} P_P \cdot N(\Delta f, T) \qquad (2.7)$$

where $\kappa$ is a material specific constant related to the scattering cross-section.

The polarisation, phase and direction of the scattered photons are not preserved.

### 2.3.1 Temperature Dependence of Spontaneous Raman Scattering

Particular attention is placed on the temperature dependence of the spontaneous Raman scattering. A solid (silica which constitutes the fiber-core) at a certain absolute temperature $T$ can be regarded as comprised of quantized harmonic oscillators in equilibrium with a gas of phonons [22]. The phonons and the harmonic oscillators of comparable energy can freely exchange energy but the mean number of phonons is constant at a given temperature. Phonons may be described as quasi-particles that obey the Bose-Einstein distribution [23] rendering the probability of phonon creation or annihilation temperature dependent. The mean number of phonons $\overline{n}(\omega_p, T)$ at a given temperature $T$ is thus proportional to the probability of existence of a boson possessing the energy $\hbar\omega_p$

$$\overline{n}(\omega_p, T) \propto \frac{1}{e^{\frac{\hbar\omega_p}{k_B T}} - 1} \qquad (2.8)$$

where $\omega_p$ is the harmonic frequency of the involved phonon, $k_B$ is the Boltzmann's constant and $\hbar$ is the Planck's constant ($\hbar = h/2\pi$).

The power of light spontaneously scattered in the Stokes band, $P_S$, at a given wavelength $\lambda_S$ is directly proportional to the power of the excitation light, $P_P$, to the refractive index $n_S$ at $\lambda_S$, and to the probability of creation of a new phonon at frequency $\omega_p$. This probability is proportional to $\overline{n} + 1$ [24]. Using equation (2.7),

$$P_S \propto \frac{P_0 n_S}{\lambda_S^4} \frac{e^{\frac{\hbar\omega_p}{k_B T}}}{e^{\frac{\hbar\omega_p}{k_B T}} - 1} \Gamma(\Delta f) \tag{2.9}$$

where $\Gamma(\Delta f)$ is proportional to the Raman spectrum shown in figure 2.2. Accordingly, for the power $P_{aS}$ contained in the anti-Stokes band, one can state

$$P_{aS} \propto \frac{P_0 n_{aS}}{\lambda_{aS}^4} \frac{1}{e^{\frac{\hbar\omega_p}{k_B T}} - 1} \Gamma(\Delta f) \tag{2.10}$$

where the probability of phonon annihilation is assumed to be proportional to $\overline{n}$ [25], and $n_{aS}$ is the refractive index at $\lambda_{aS}$.
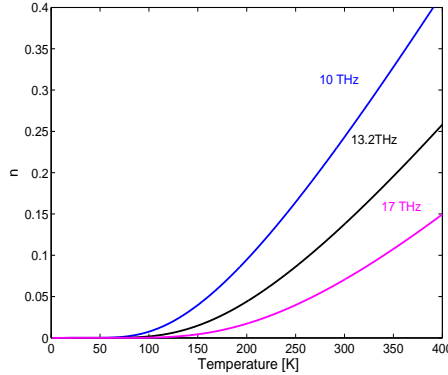


**Figure 2.3:** Mean number of phonons (with three different energies) as function of temperature.

The strength of both Stokes and anti-Stokes decreases with the temperature. At absolute zero temperature, there are no phonons in the medium, and thus no Raman anti-stokes scattering, whereas Raman Stokes scattering, with scattering probability proportional to $\overline{n} + 1$, approaches its finite minimum.

Assuming the created and absorbed phonons possess the same energy, i.e., have the same frequency, the ratio of the powers in the two

lines is

$$\frac{P_{aS}}{P_S} \propto \frac{n_{aS}\lambda_S^4}{n_S\lambda_{aS}^4} e^{-\frac{\hbar\omega_p}{k_B T}} \tag{2.11}$$

From equation (2.11) it is possible to isolate and determine the absolute temperature unambiguously when both $P_S$ and $P_{aS}$ are known, together with a calibration constant $\kappa$, previously determined at a known temperature.

$$T = \left( \frac{k_B}{\hbar\omega_p} \ln \left( \kappa \frac{P_S}{P_{aS}} \frac{n_{aS}\lambda_S^4}{n_S\lambda_{aS}^4} \right) \right)^{-1} \tag{2.12}$$

Also apparent from the equation (2.11) is the fact that, at thermal equilibrium, the spontaneous Stokes scattering is stronger than the spontaneous anti-Stokes scattering by approximately $exp(\hbar\omega_p/k_B T)$. That is, the probability of a photon being Raman Stokes scattered is always higher than that of being Raman anti-Stokes scattered, but this difference reduces as the temperature increases.

## 2.4 Stimulated Raman Scattering

Raman scattering is a very weak process unless the excitation light is intense. With the availability of lasers, the important process of stimulated Raman scattering (SRS) was observed in 1962 [26]. This is a strong nonlinear process that can shift a large fraction of the incident light to lower frequencies.

As opposed to spontaneous scattering, stimulated scattering results from fluctuations in the dielectric constant induced by the electromagnetic field (i.e. the light) in the medium. Thus, it is a process dependent on the intensity of the electromagnetic field in the fibre. The stimulated Raman scattering is emitted non-uniformly - the scattered photons adopt the properties of the stimulating photons. The radiation pattern follows roughly $cos^2(\theta)$ [9].

SRS is also polarisation dependent, where the gain coefficient can be divided into $g_{r||}$ and $g_{r\perp}$, with $g_{r||} >> g_{r\perp}$ [21]. However, also here, for the purposes of this work, it is sufficient to operate with the average Raman gain coefficient $g_r$.

Stimulated Raman scattering scales inversely with the pump wavelength $\lambda_P$. Finally, note that unlike spontaneous Raman scattering,

stimulated Raman scattering is not dependent on temperature [27]. The gain depends on the difference between stimulated emission and absorption which is constant with temperature.

## 2.5   Scattering in Fibres

Spontaneous Raman scattering is radiated in all directions. However, only a fraction of the total scattered photons are captured and guided in the fibre. The capture fraction $\nu$ is defined as the ratio between guided backscattered light $P_{BS}$, and total scattered light $P_{SC}$. There is
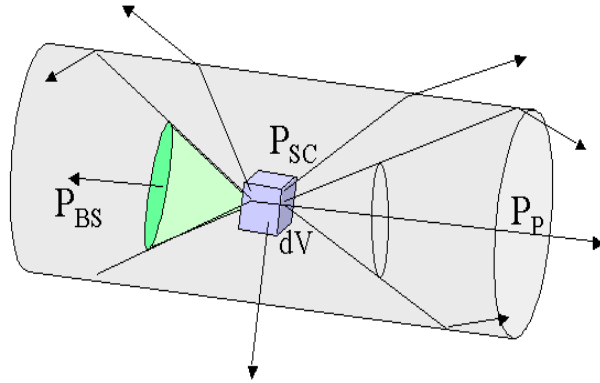


**Figure 2.4:** Capture fraction is defined as the ratio between guided backscattered light and total scattered light.

a cone from each scattering element $dV$ within the fibre core in which the light is captured and guided. Integrating the captured light, the capture fraction for a single-mode fibre is found to be [28] [29]

$$\frac{P_{BS}}{P_{SC}} \equiv \eta(\lambda) = \frac{3\lambda^2}{8\pi n^2(\lambda) A_{eff}(\lambda)} \tag{2.13}$$

The variation of refractive index with wavelength $n(\lambda)$ is modelled with Sellmeier's approximation (Appendix C), while the effective mode

area $A_{eff}$ of the single-mode fibre is approximated with the spot-size [9]

$$
\begin{aligned}
A_{eff} &\approx w^2 \pi \\
where \; w &= a(0.65 + 1.619V^{-3/2} + 2.879V^{-6}) \\
and \; V &= \frac{2\pi a n}{\lambda}\sqrt{2\Delta n}
\end{aligned}
\tag{2.14}
$$

where the core radius $a = 4\mu m$, and $\Delta n = 3 \times 10^{-3}$.

The capture fraction for a standard SMF is depicted in figure 2.5(a), where the Gaussian approximation of the field profile is assumed. Note that only a few per cent of scattered light is captured, and most of the light is dispersed and absorbed in fibre cladding and coating. The spot-size is shown in figure 2.5(b).



(a)                                             (b)
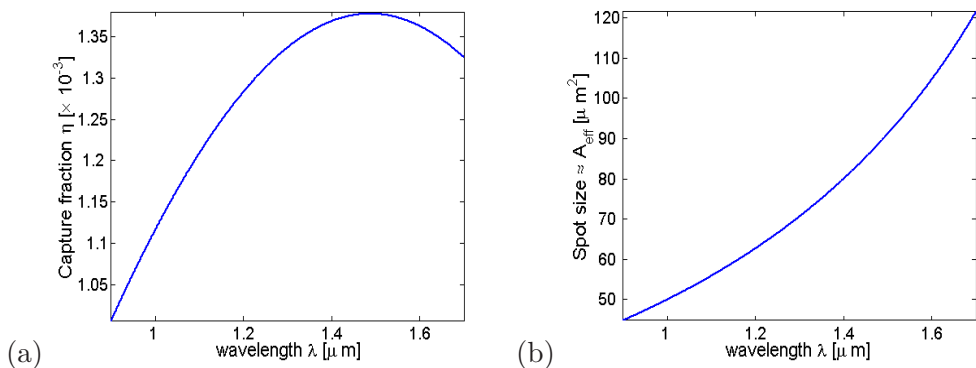
**Figure 2.5:** (a) Capture fraction of a standard SMF as a function of wavelength, (b) Spot-size as a function of wavelength in a standard SMF ($a = 4\mu m$ and $\Delta = 3 \times 10^{-3}$).

Fibres that support propagation of multiple modes usually have a higher capture fraction (or numerical aperture NA). Capture fraction is, in the following, incorporated in the scattering cross-section and is therefore an important factor in reflectometry.

## 2.6   Raman Scattering Experiments

After the equations governing the Raman scattering are established, it is important to quantify the material parameters for further investigation.

This section describes the procedure and apparatus for measurement of the spontaneous and stimulated Raman scattering coefficients in optical fibres. The results obtained for the standard single-mode fibre are used throughout the thesis.

### 2.6.1   Spontaneous Raman Scattering coefficient

The description of the spontaneous Raman scattering is simplified to

$$dP_R = P_P \chi_R(T, \lambda) dz \tag{2.15}$$

where $\chi_R(T, \lambda)$ is the scattering coefficient which includes proportionality constants, the capture fraction, and average of the contributions from the two polarisations. It has unit $m^{-1}$. The pump is thus unpolarised with fixed wavelength. $\chi_R$ is called the spontaneous Raman scattering coefficient in the following, and is determined separately for each fibre at room temperature. $\chi_R$ is not to be confused with the third order susceptibility $\chi^{(3)}$. $\chi_S$ is the spontaneous Raman scattering coefficient for the Stokes, $\chi_{aS}$ for the anti-Stokes band.

When measuring $\chi_R$, one must avoid generating excessive stimulated Raman scattering. Therefore, relatively low laser power is used in the following measurements. The setup of the experiment is shown in figure 2.6. It comprises a pump laser with an isolator, optical add/drop multiplexer, the optical fibre on which the measurement is taken and the optical spectrum analyser (OSA). The linewidth of the laser is around $1nm$, which is wide enough to suppress the stimulated Brillouin scattering, and narrow in comparison to features in the Raman spectrum. The optical add/drop filter separates the pump and Raman scattering. Furthermore, it filters the laser light entering the fibre so that no Rayleigh scattering, which is orders of magnitude stronger, occurs in the Raman band. Measurement on $11.2km$ standard SMF is performed with a pump laser with wavelength $\lambda_P = 1493nm$.

The detected spectrum at the OSA is shown in figure 2.7, clearly showing the features of Raman scattering shown in figure 2.2. According to (2.8), greatest deviations from figure 2.2 at finite temperature (room temperature) are expected at low frequency shifts.

Assuming that the pump power is so weak that no significant stimulated Raman scattering occurs, and that the attenuation and $\chi_R$ are
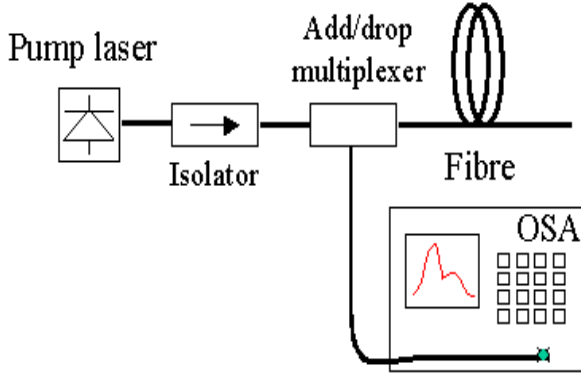
**Figure 2.6:** Setup for measurement of the spontaneous Raman scattering coefficient $\chi_R$.
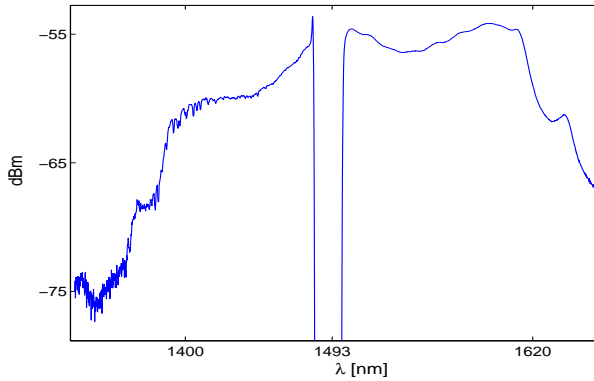


**Figure 2.7:** The optical signal detected by the optical spectrum analyser showing the anti-Stokes band ($\lambda < 1493nm$) and the Stokes band ($\lambda > 1493nm$).

uniform along the fibre, the scattering coefficient is found to be

$$\chi_R = P_R / \left( \psi_f \cdot P_0 \cdot \int_0^L e^{-(\alpha_P + \alpha_R)z} dz \right) \qquad (2.16)$$

$\psi_f$ accounts for the insertion loss in the optical filters. The power is integrated in the wavelength interval $1540 - 1610nm$ for Stokes and $1380 - 1440nm$ anti-Stokes scattering, and inserted into the equation (2.16). (This is the width of the optical filters to be used later, when comparing optical fibres). The measurement is made three times at

| $P_P$ [mW] | $P_{aS}$[nW] | $\chi_{aS}$ [$m^{-1}$] | $P_P$ [mW] | $P_S$[nW] | $\chi_S$ [$m^{-1}$] |
|---|---|---|---|---|---|
| 33 | 20.3 | $137 \cdot 10^{-12}$ | 30 | 60.8 | $522 \cdot 10^{-12}$ |
| 43.5 | 26.5 | $135.6 \cdot 10^{-12}$ | 41 | 84.4 | $530 \cdot 10^{-12}$ |
| 59.5 | 35.9 | $134.3 \cdot 10^{-12}$ | 50.5 | 105.6 | $538 \cdot 10^{-12}$ |

**Table 2.1:** Measurement of the spontaneous Raman scattering coefficients $\chi_{aS}$ and $\chi_S$ in single-mode fibre, where the results are obtained using equation (2.16).

different low pump powers $< 60mW$. Spontaneous scattering grows linearly with the pump power, and similar results for $\chi_R$ indicate that there is, in fact, hardly any stimulated Raman scattering ($< 3\%$). Measurements of the $\chi_R$ parameters in the single-mode fibre are given in table 2.1.

It is found that $\chi_S \approx 520 \cdot 10^{-12} m^{-1}$ and $\chi_{aS} \approx 140 \cdot 10^{-12} m^{-1}$. This is consistent with equation (2.11), taking into consideration the difference in capture fraction at different wavelengths. The experiment is repeated with the graded-index multi-mode fibre, and it is found that $\chi_S \approx 870 \cdot 10^{-12} m^{-1}$, and $\chi_{aS} \approx 220 \cdot 10^{-12} m^{-1}$. These values are measured at room temperature $\approx 295K$. Note that there is an uncertainty in the measurement on the graded-index multi-mode fibre due to existence of multiple modes, and unstable coupling coefficients to the single-mode WDM filter.
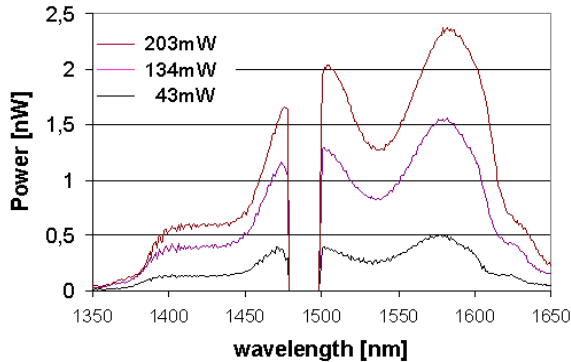


**Figure 2.8:** Spontaneous Raman back-scattering from graded-index multi-mode fibre at three pump powers, with $\lambda_P = 1482nm$.

### 2.6.2   Stimulated Raman Scattering efficiency

It is necessary to know the Raman gain coefficient $g_r$ or efficiency $g_R$ of a certain medium (silica fibre) to be able to predict the behaviour of the involved signals.

When measuring the stimulated Raman scattering, that is, the Raman gain spectrum of the fibre, the pump power is increased to the maximum, and a seed signal is added from the far fibre end. The pump beam is depolarised, and yields approximately $200mW$ at $\lambda_P = 1493nm$. $11.2km$ SMF is used as the gain medium. Setup for the measurement is shown in figure 2.9.
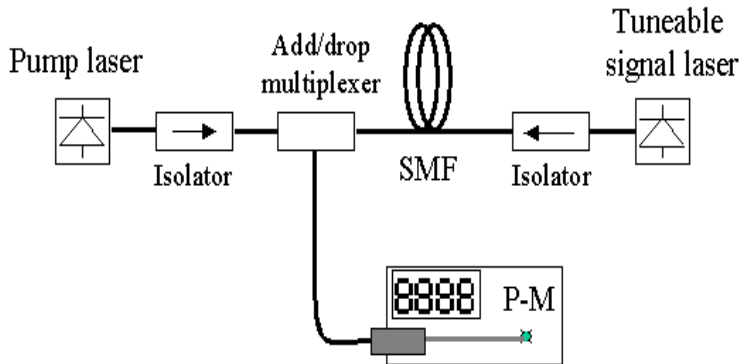


**Figure 2.9:** Setup for measuring stimulated Raman gain coefficient.

Received light is monitored with and without presence of the pump light in the fibre. A tuneable laser provides the seed signal, which is detected by an OSA. The seed signal is at least two orders of magnitude stronger than the spontaneous emission (measured with signal off and pump on), but does not saturate the gain. Hence, the spontaneous emission may be neglected here.

The coupled equations describing the power of the pump $P_P$ and the power of the counter-propagating seed signal $P_s$ are

$$\frac{dP_s}{dz} = -g_R P_P P_s + \alpha_s P_s \qquad (2.17)$$

$$\frac{dP_P}{dz} = -\alpha_P P_P \qquad (2.18)$$

Solving the linear first order differential equation yields the expression for signal power as it propagates through the fibre.

$$P_s(z) = \vartheta e^{\frac{g_R P_0}{\alpha_P} e^{-\alpha_P z} + \alpha_s z}$$  (2.19)

The ratio of signal power at output and input, i.e., at $z = 0$ and $z = L$ when the pump laser is on is,

$$P_{ON} \equiv \frac{P_{s,ON}(0)}{P_{s,ON}(L)} = e^{\frac{g_R P_0}{\alpha_P}(1-e^{-\alpha_P L}) - \alpha_s L}$$  (2.20)

and when the pump laser is off,

$$P_{OFF} \equiv \frac{P_{s,OFF}(0)}{P_{s,OFF}(L)} = e^{-\alpha_s L}$$  (2.21)

Using the ratio of (2.20) and (2.21), one can isolate the Raman gain factor

$$g_R = \frac{\alpha_P}{P_0(1 - e^{-\alpha_P L})} \cdot ln\left(\frac{P_{ON}}{P_{OFF}}\right) = \frac{ln\left(\frac{P_{ON}}{P_{OFF}}\right)}{P_0 L_{eff}}$$  (2.22)

The gain spectrum is obtained in the wavelength interval allowed by the tuneable laser and Stokes filter - $1540nm - 1580nm$. The measured
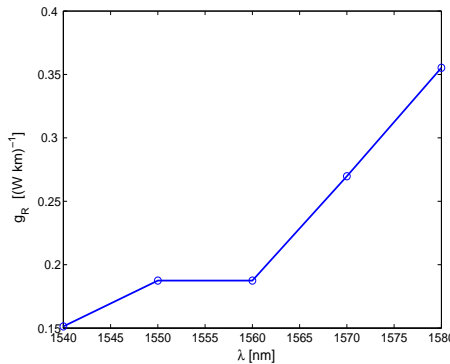


**Figure 2.10:** Measured stimulated Raman gain in $11.2km$ SMF as function of wavelength (limited interval). $\lambda_P = 1493nm$ with $P_0 = 200mW$.

Raman gain efficiency $g_R$ as function of wavelength is shown in figure

2.10. It is important to determine the maximum value of the gain efficiency since most of the signal experiences this gain. In the regarded wavelength interval it is found to be $g_R = 0.355(Wkm)^{-1}$. Highest gain efficiency is, however, expected at $13.2THz$ shift or approximately $1590nm$. In figure 2.2, one can see that the gain curve is flat in this region. Therefore, the approximated value $g_R = 0.36(Wkm)^{-1}$ is used later in the thesis (Chapter 6).

Similar value for single mode fibre is reported elsewhere in the literature [30] [31] [32] [9]. Often the Raman gain coefficient $g_r = g_R \cdot A_{eff}[m/W]$ is given since it may be more instructive to operate with intensity of the involved fields instead of the power when SRS is described. In this work, the system of differential equations, however, deals with powers and it is thus more convenient to use $g_R$.

With same pump power, the intensity of the electromagnetic field in the step-index multi-mode fibres is by far smaller than in standard single-mode fibres. The stimulated Raman scattering is therefore not as evident. However, in graded-index multi-mode fibres, the power is confined to the centre of the core, and Raman gain coefficient is not negligible. Figure 2.11 shows Raman gain in $7.8km$ graded-index multi-mode fibre as function of wavelength, when pumped with $1482nm$ pump. Also here,
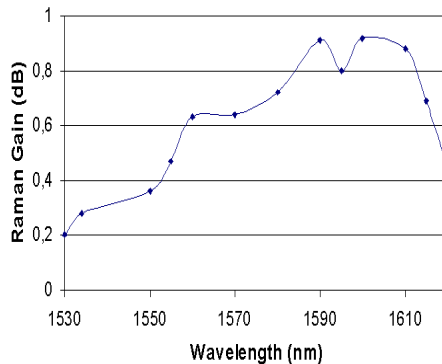


**Figure 2.11:** Measured stimulated Raman gain as function of wavelength in $7.8km$ graded-index multi-mode fibre. $\lambda_P = 1482nm$.

the measured gain spectrum resembles the Raman gain spectrum known from other silica fibres, e.g., the one depicted in figure 2.2. Using equation (2.22), it can be found that the gain peaks at $g_R = 0.17(Wkm)^{-1}$

in the GIMMF.

It may be surprising that the Raman gain coefficient in the multi-mode fibre with a core diameter of $62.5\mu m$ is so high. The explanation may be that the single-mode pump light, which is launched into the multi-mode fibre, will excite only a few modes in the multi-mode fibre. The high intensity is therefore maintained, and high stimulated Raman amplification is generated. This corresponds well with the fact that coupling loss from the graded-index multi-mode fibre to the single-mode fiber is measured to be only $3 - 5dB$. Note also that the signal level fluctuated during the measurements, probably due to multi-mode interference effects and polarisation variations.

### 2.6.3   Stimulated Raman scattering in small core area fibres

It is demonstrated that the spontaneous Raman backscattering grows linearly with pump power. However, at certain intensity and with long interaction length, stimulated Raman scattering becomes significant. The power of Raman scattered light in single-mode fibre (SMF), dispersion-compensating fibre (DCF) and Raman fibre (RAF) is measured and depicted in figures 2.12, 2.13 and 2.14 for $11.2km$ SMF, $4.8km$ DCF and $3km$ RAF, respectively. The pump wavelength is still $\lambda_P = 1493nm$. Apparently, one cannot increase the power of the pump laser indefinitely, to strengthen the spontaneous scattering. Stimulated Raman scattering is not temperature dependent, and cannot be filtered out from spontaneous scattering. Therefore, it can create faulty signal in Stokes channel, or even attenuate the signal in the anti-Stokes channel. This issue is treated more in Chapter 6.

## 2.7   Test of results

When both $\chi_{aS}$ and $g_R$ are determined, one can test the results in experiment where neither the contribution from SRS nor the spontaneous Raman scattering is negligible. The power of the Raman scattered light from entire fibre is then

$$P_R = \psi_f \cdot P_0 \cdot \chi_R \cdot \int_0^L e^{-(\alpha_P+\alpha_R)z+\frac{g_R P_0}{\alpha_P}\left(1-e^{-\alpha_P z}\right)} dz \qquad (2.23)$$
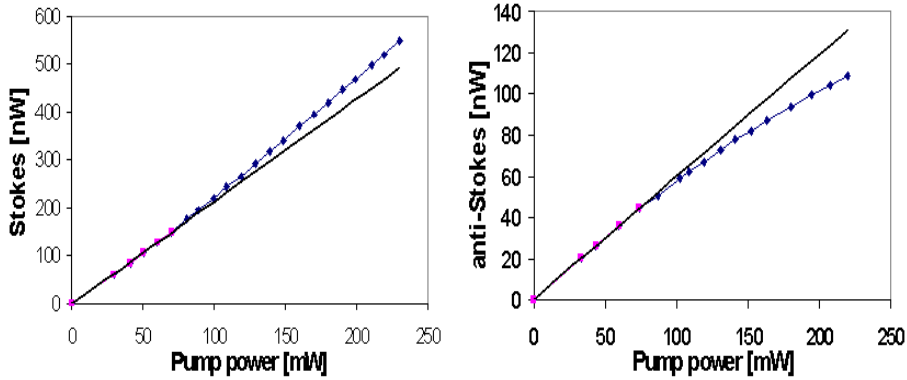
**Figure 2.12:** Measured power of Stokes and anti-Stokes channels in $11.2km$ long SMF as function of the output power of pump laser, plotted together with the linear approximation where no SRS takes place.
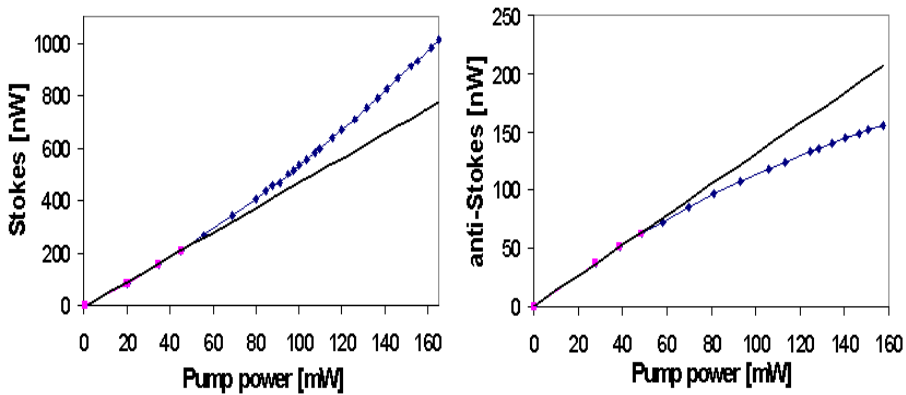


**Figure 2.13:** Measured power of Stokes and anti-Stokes channels in $4.8km$ long DCF as function of the output power of pump laser, plotted together with the linear approximation where no SRS takes place.

where $g_R$ of anti-Stokes channel is scaled up with the wavelength. Figure 2.15 shows the measured data and results predicted by equation (2.23). There is a very good agreement between the measured and modelled data.
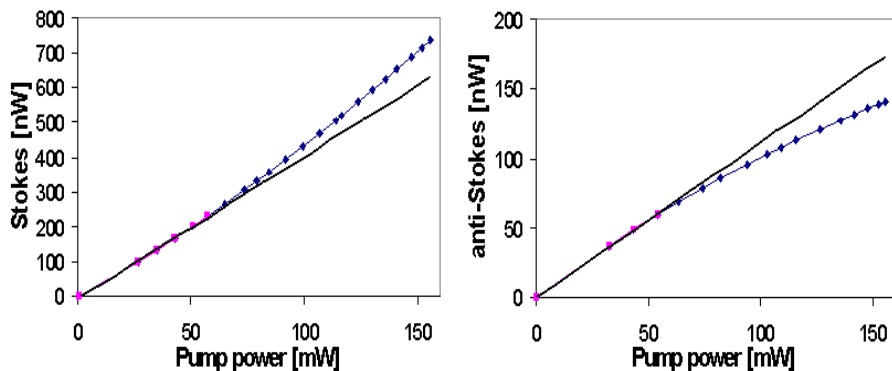
**Figure 2.14:** Measured power of Stokes and anti-Stokes channels in $3km$ long RAF as function of the output power of pump laser, plotted together with the linear approximation where no SRS takes place.
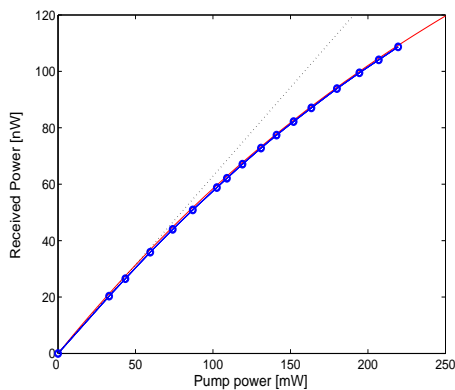


**Figure 2.15:** Measured and modelled anti-Stokes signal power in $11.2km$ long SMF as function of the output power of pump laser. Both stimulated and spontaneous Raman scattering take place.

## 2.8 Summary

In this chapter, basics of the Raman scattering are introduced. It is an inelastic form of non-linear scattering, where power is exchanged with the medium - phonons are created and annihilated, creating Stokes and anti-Stokes photons. There are two fundamental Raman scattering

processes, namely the intensity dependent stimulated Raman scattering (SRS), and the temperature and power dependent spontaneous Raman scattering.

Spontaneous Raman scattering is a very weak process. It grows linearly with the excitation light. Furthermore, the probability for scattering to occur follows the temperature dependent Bose-Einstein distribution.

Stimulated Raman scattering can be efficient in transferring light to lower frequencies. Especially in small-core single-mode fibres, the confinement of light makes the field intensity high, and thus stimulated Raman scattering non-negligible.

The physical constants describing the spontaneous as well as stimulated Raman scattering in single-mode fibre and graded-index multimode fibre are measured in two experiments. The measured parameters yield good agreement with an experiments involving both forms of Raman scattering.

# Chapter 3

# Distributed Temperature Sensing

Different techniques for distributed fibre sensing have been developed to suit different needs and requirements of fibre sensors. For the desired range and resolution of the sensors considered in this thesis, that is, range $L \approx 10km$ with resolution $\Delta z \approx 1m$, one can roughly classify the spatial resolving methods into time coding, frequency coding and wavelength coding.

In time coding, the location of scattering in the fibre is extracted from the time it takes for an optical pulse to arrive to the detector, after being affected by the measured effect. Frequency coding is based on the analysis of the frequency response of the fibre, and finally, in wavelength coding, the wavelength spectrum of the reflected or transmitted light is examined. All techniques have advantages and drawbacks in terms of resolution, measurement time, cost and complexity.

The focus of the thesis is on the Incoherent Optical Frequency Domain Reflectometry (IOFDR), and it is compared to another sensing method based on Optical Time Domain Reflectometry (OTDR). This chapter develops principles and theory of IOFDR for distributed temperature sensing based on spontaneous Raman backscattering, and presents the possibilities with respect to the choice of the Raman and Rayleigh signals, which can be used to obtain temperature profiles of a fibre.

# 3.1   Incoherent optical frequency domain reflectometry

A basic sketch of the fibre sensor is shown in figure 3.1. The fibre is illuminated with the pump laser, and the Raman back-reflection is split into two channels: Stokes and anti-Stokes channel. A section of the fibre is at monitored temperature.
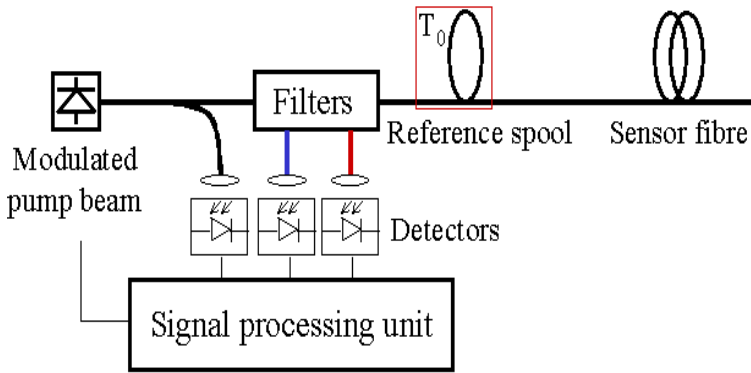


**Figure 3.1:** Sketch of a fibre-optic distributed temperature sensor (DTS) based on incoherent optical frequency domain reflectometry (IOFDR).

Spatial resolving of the back-scattered light is obtained by IOFDR. IOFDR is in principle similar to Stepped Frequency Continuous Wave (SFCW) RADAR systems [33] [34] where the waveform of the transmitted radar waves consists of a sequence of discrete, equally spaced frequencies. The range profile is synthesised by performing inverse Fourier transform on the received signal.

Here, the fibre is illuminated with a sinusoidally modulated pump beam. The modulation frequency is sequentially increased by a fixed increment $\Delta f_m$ from $0 Hz$ to $MHz$ region, and for each step, a measurement of the phase and amplitude of the sinusoidal Raman-backscattered light is made. The frequency response is then transformed to the space domain, after which the distributed temperature is calculated.

The power of the sine modulated pump light that is propagating in the fiber can be expressed as

$$P_P(z, \omega_m, t) = P_0 e^{-\alpha_P z}\Big(1 + m \cdot \cos(\omega_m t - \omega_m \beta_P z)\Big) \qquad (3.1)$$

where $z$ is the distance, $m$ is the modulation depth, $\omega_m$ the radial modulation frequency of the pump source, $c$ is the velocity of light in free space, $n_P$ the refractive index at the pump wavelength $\lambda_P$, and hence $\beta_P = n_P/c$ is the reciprocal of the velocity of light in the fiber. Ideally, the modulation depth would be $m = 1$ but it is usually less than that in order to drive the laser in the linear regime. $\alpha_P$ is the attenuation coefficient in the fiber at $\lambda_P$, which is initially assumed to be temperature independent. $P_P$ is a real, positive harmonic function, but by use of notation in (3.2), the following derivations are simplified.

$$P_P(z, \omega_m, t) = P_0 e^{-\alpha_P z} \mathbb{R} \left\{ 1 + m \cdot e^{\jmath \omega_m t - \jmath \omega_m \beta_P z} \right\} \qquad (3.2)$$

The power of Raman-scattered light from an infinitesimal section $dz$ can be written as

$$dP_S(z, \omega_m, t) = P_P(z, \omega_m, t) \chi_S(T(z, t)) dz \qquad (3.3)$$
$$dP_{aS}(z, \omega_m, t) = P_P(z, \omega_m, t) \chi_{aS}(T(z, t)) dz \qquad (3.4)$$

where $T$ is the absolute temperature, $\chi_R(T(z, t))$ the temperature dependent Raman scattering coefficient of either the Stokes or anti-Stokes photons. Temperature variations are assumed to be much slower than the measurement time so that $T$ is, in the following, only space dependent. $\chi_R$ is fiber-specific and thus dependence on numerical aperture, doping levels, etc. are avoided. Because of the obvious similarity in the form of equations for the Stokes and anti-Stokes channels, subscript $R$ will denote both Raman channels, unless there is a need to distinguish between the two, in which case $S$ and $aS$ are used.

From equations (3.2) and (3.4) it follows that the back-reflected signal $dP_{Rz'}(0, t, \omega_m)$ at the detector, originating from $dz$ around the point $z'$ can be expressed by

$$dP_{Rz'}(0, \omega_m, t) = P_0 \cdot \chi_R \cdot e^{-(\alpha_P + \alpha_R)z'} \cdot \mathbb{R} \left\{ 1 + m \cdot e^{\jmath \omega_m t - \jmath \omega_m (\beta_P + \beta_R)z'} \right\} dz$$
$$(3.5)$$

The received Raman backscattered signal from the entire fiber of length

$L$ is a summation from all the infinitesimal fiber sections i.e. the integral

$$
\begin{aligned}
P_R(0, \omega_m, t) \;=\; & P_0\Big( \int_0^L \chi_R(T(z)) \cdot e^{-(\alpha_P + \alpha_R)z} dz \\
& +\; m \cdot \mathbb{R}\Big\{ e^{\jmath\omega_m t} \int_0^L \chi_R(T(z)) \cdot e^{-(\alpha_P + \alpha_R)z - \jmath\omega_m(\beta_P + \beta_R)z} dz \Big\}\Big)
\end{aligned}
\tag{3.6}
$$

The loss originating from possible splices, optical components and other perturbations of the signals that are specific for a certain setup are neglected here, since these factors can be eliminated after the process of calibration of the sensor by a single constant.

The first term in the parenthesis of equation (3.6) is invariant with respect to the modulation frequency and contains no information on the location from where the Raman scattering originates. It is called the DC term. The second term, or the AC term, on the other hand, is modulation-frequency dependent and is written as

$$
\tilde{P}_R(0, \omega_m, t) = P_0 \cdot m \cdot \mathbb{R}\Big\{ e^{\jmath\omega_m t} \cdot \int_0^L s_R(z) \cdot e^{\jmath\Omega_{PR}z} dz \Big\}
\tag{3.7}
$$

where $\Omega_{PR} = \omega_m(\beta_P + \beta_R)$, and $s_R(z) = \chi_R(T(z)) \cdot exp(-(\alpha_P + \alpha_R)z)$, which contains both the scattering coefficient and the attenuation factors. One can regard the integral of equation (3.7) as a Fourier transform $S_R(\omega_m)$ of $s_R(z)$. $s_R(z)$ are the backscattering functions of the Stokes and anti-Stokes backscattered light, in space domain.

Thus, if the inverse Fourier transformation is performed on the arrays of the discrete measured complex data at frequencies $[-\omega_{m,max}; \omega_{m,max}]$, that is $S_R(\omega_m)$, periodic functions are obtained. One period of each of these functions contains the backscattering functions $s_R(z)$. The process is illustrated in figure 3.2. Since the attenuation coefficients at $\lambda_R$ and $\lambda_P$ are known, it is possible to obtain $\chi_R(T(z))$ from the backscattering function.

Using functions $\chi_R(T(z)))$ and equation (2.12), distributed temperature is calculated. Equation (3.8) is derived in Appendix B expresses the temperature distribution along the optical fiber.

$$
T(z) = \Big( \frac{1}{T_0} + \frac{k_B}{\hbar\omega_p} \ln\big(R_0 \cdot R^{-1}(T(z))\big) \Big)^{-1}
\tag{3.8}
$$
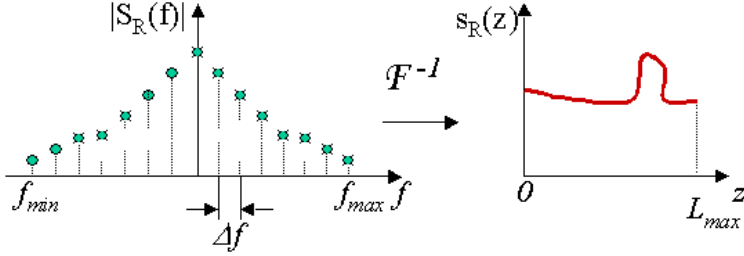
**Figure 3.2:** The arrays of complex frequency responses of the fibre $S_R(\omega_m)$ to the pump-laser light, which is stepwise increased in modulation frequency, is inverse-Fourier transformed to backscattering functions $s_R(z)$.

where $R(T(z))$ is the ratio between the anti-Stokes and Stokes distributed backscattering coefficients in space domain. The calibration constant $R_0$ is obtained from the backscattering coefficients measured in the reference spool, shown in figure 3.1, where the reference temperature $T_0$ is monitored.

$$R(T(z)) \quad = \quad \frac{\chi_{aS}(z)}{\chi_S(z)} \cdot e^{-(\alpha_S - \alpha_{aS})z} \tag{3.9}$$

$$R_0 \quad = \quad \frac{n_{aS}\lambda_S^4}{n_S\lambda_{aS}^4} \cdot e^{-\frac{\hbar\omega_p}{k_B T_0}} \tag{3.10}$$

Since the attenuation in the fibre may change with the temperature, or be non-uniform along the fibre, for greater accuracy it may be necessary to add up the attenuation that is experienced by the wave at each point $dz$ in the fibre [35]. The equation (3.8) becomes

$$T(z) = \left(\frac{1}{T_0} + \frac{k_B}{\hbar\omega_p} \ln\left(C_0 \cdot \frac{n_{aS}\lambda_S^4}{n_S\lambda_{aS}^4} \frac{\chi_S(z)}{\chi_{aS}(z)} \cdot e^{-\int_0^L (\alpha_S(z) - \alpha_{aS}(z))dz}\right)\right)^{-1} \tag{3.11}$$

where $C_0$ is a constant dependent on the calibration temperature.

### 3.1.1 Spatial resolution and sensor range

The inverse Fourier transform of a discrete frequency spectrum, as $S_R(\omega_m)$ in IOFDR, is a continuous periodic function. The backscattering functions $s_R(z)$ in space domain are therefore contained in one period of the

inverse transform of the frequency response $S_R(\omega_m)$. The length of one such period $\Pi_0$ is defined by the frequency step $\Delta f_m$ [36]. It follows that the maximum length of the fibre sensor $L_{max}$ is limited by the step in modulation frequency (assuming sufficient input power to the detector)

$$L_{max} = \frac{c}{2n_g}\frac{1}{\Delta f_m} \tag{3.12}$$

Using the numerical IFFT algorithms, one cannot resolve more spatial points than the number of measurements/samples in the frequency domain. In consistence with this fact, and using (3.12), the systems spatial resolution $\Delta z_{IOFDR}$ is found to be [37]

$$\frac{\Delta z_{IOFDR}}{L_{max}} = \frac{\Delta f_m}{f_{max} - f_{min}} \Leftrightarrow$$

$$\Delta z_{IOFDR} = \frac{c}{4n_g f_{max}} \tag{3.13}$$

where frequencies have sign so that $f_{min} = -f_{max}$ and thus $f_{max} - f_{min} = 2f_{max}$. It is thus sufficient to measure frequency responses with modulation frequencies spanning from $0Hz$ to $f_{max}$ since $S_R(-f_m)$ is the complex conjugate of $S_R(f_m)$. Spatial resolution is defined as the spacing between distinguishable adjacent measurement points. The resolution corresponds to a quarter of the length of the sine-modulated pump-light wave in the fibre at frequency $f_{max}$.

IFFT algorithms are most efficient when the number of points $N = 2^n$, where $n \in \mathbb{N}$ [36]. A drawback with IOFDR is that, with a certain range and desired resolution, one has to make suboptimal measurements. For example, if a $10km$ fibre is measured with a resolution of $1m$, one would usually have 16356 measurement points and measurement time seemingly longer than necessary.

Whereas the spatial resolution of an IOFDR system, $\Delta z_{IOFDR}$, is defined by the maximum modulation frequency $f_{max}$ of the pump laser, in an OTDR system, the spatial resolution $\Delta z_{OTDR}$ is determined mainly by the sampling-rate of the signals, assuming that the pulse width of the pump $\tau_p$ is shorter than or equal to the the time between two samples $\tau_p \leq \tau_n - \tau_{n-1}$, or sampling period $1/f_{samp}$. Furthermore, it is only the attenuation in the fiber, and hence the sensitivity of the detectors, that limits the range of the sensor, i.e. $L_{max}$ is not imposed by any other

parameter. If $n_g$ is the group index at the pump and Raman-signal wavelengths in the fiber, the smallest distance between two measurement points $\Delta z_{OTDR}$ is

$$\Delta z_{OTDR} = \frac{c}{2n_g}\tau_p = \frac{c}{2n_g}\frac{1}{f_{samp}} \quad (3.14)$$

Consequently, to obtain the same resolution, twice as short pulses are needed in OTDR than the shortest pulse in IOFDR. A more thorough comparison between the OTDR and IOFDR follows in Chapter 4.

### 3.1.2 Frequency response

Assuming the temperature is constant along the uniform fiber, the Raman scattering coefficient $\chi_R$ is also constant. The integral of equation (3.7) is evaluated, and the magnitude of the AC term of the received power is found

$$
\begin{aligned}
|\tilde{P}_R(0,\omega_m)| &= \mathbb{R}\left\{ \frac{mP_0\chi_R}{-\alpha_\Sigma + \jmath\omega_m\beta_\Sigma}\left( e^{-\alpha_\Sigma L + \jmath\omega_m\beta_\Sigma L} - 1 \right) \right\} \\
&= mP_0\chi_R\sqrt{\frac{e^{-\alpha_\Sigma L}}{\alpha_\Sigma^2 + \omega_m^2\beta_\Sigma^2}\left( \cosh(\alpha_\Sigma L) - \cos(\omega_m\beta_\Sigma L) \right)}
\end{aligned}
$$

$$(3.15)$$

where $\alpha_\Sigma = \alpha_P + \alpha_R$ and $\beta_\Sigma = \beta_P + \beta_R$. It is evident that the magnitude of the signal falls off as the modulation frequency increases. Figure 3.3 shows an example of the calculated frequency response of an $8km$ and $2km$ long SMF. When the length of the sine-modulated pump-light wave in the fibre becomes shorter than the fibre, the decay of the frequency response function $\tilde{P}_R(0,\omega_m,t)$ starts. The amplitude of the signals can fall several orders of magnitude. This sets high demands on the sensitivity of the detection circuitry.

## 3.2 Alternative schemes for temperature determination

In Chapter 2 it is shown that both spontaneous Raman Stokes and anti-Stokes scattering (used as signal channels) are dependent on the temperature of the fibre where scattering takes place. These two channels
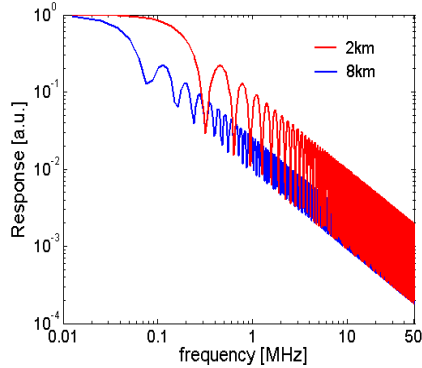
**Figure 3.3:** Computed normalised frequency response of an $8km$ and $2km$ long fibre with $\alpha_\Sigma = 0.4dB/km$ and $n_g = 1.45$.

are used in the calculations of section 3.1. However, only one temperature dependent factor may be sufficient to determine the temperature. The other channel is used merely for comparison - a means of avoiding recurring calibration because of instability in the laser pump power, characteristics of the photo-detectors or small local changes in the attenuation along the fibre. Taking the ratio between the channels cancels out the parameters subject to drift.

In this section, the possibility to use Rayleigh backscattering in combination with one of the spontaneous Raman scattering channels is investigated, as well as the scheme where one spontaneous Raman channel is used alone. The standard configuration using Stokes and anti-Stokes light is in the following referred to as SaS configuration, whereas the configurations employing Rayleigh and anti-Stokes and Rayleigh and Stokes light are referred to as RaS and SR, respectively.

### 3.2.1   Rayleigh scattering as the reference channel

Rayleigh scattering is a form of elastic scattering, i.e., the scattered photons preserve their energy. It is caused by fluctuations on small scale $(< \lambda_P)$ in the density of the matter, and thus of the refractive index of the medium [9]. Rayleigh scattering is a relatively strong effect and is the main source of attenuation in silica in the IR region [9]. The

Rayleigh-scattered power $P_{Rayleigh}$ has the following dependence [9]

$$P_{Rayleigh} \propto \frac{P_0 n_P}{\lambda_P^4} \qquad (3.16)$$

There are many reasons supporting the idea of using Rayleigh scattering instead of spontaneous Raman Stokes scattering as the channel with which the temperature dependent anti-Stokes channel is compared. The idea has been proposed and implemented [38], but not thoroughly analysed.

First of all, Rayleigh scattering is around $30dB$ stronger than the spontaneous Raman Stokes scattering [10]. The difference in received power appropriately improves the SNR of the substituted signal channel. Note, however, that the anti-Stokes channel is the channel that limits the accuracy of the device, as it is usually $5-10dB$ lower than the Stokes channel, so that the total improvement is still modest.

An additional advantage is that less noisy (and cheaper) detectors can be used to detect the stronger Rayleigh scattering instead of spontaneous Raman scattering. The optical filtering module is also simpler; there is no need for two Raman filters but only one.

Furthermore, the wavelength of the pump laser can be chosen more freely. Namely, it is more difficult to have all three: Stokes, anti-Stokes and the pump light in the region of low attenuation in silica, than only two of them. The Raman channels are around $13THz$ to each side of the pump, which results in a separation between Stokes and anti-Stokes channels of $200nm$ at $1500nm$ pump wavelength. Potential problems with difference in group velocity at the wavelengths of the channels are smaller too. A more thorough analysis of the choice of the wavelength is given in Chapter 6.

The power of Rayleigh scattered light is virtually independent of the temperature, and does not follow the anti-Stokes scattering when the temperature of the fibre fluctuates. Thus, a larger change in $R(z)$ is created for the same change in temperature, i.e., the sensitivity of Rayleigh - anti-Stokes system (RaS) is higher.

$$\frac{dR_{RaS}(z)}{dT} > \frac{dR_{SaS}(z)}{dT} \qquad (3.17)$$

As indicated in section 2.6, stimulated Raman scattering can distort

the signal data. Rayleigh scattering is almost unaffected by the SRS effect, which makes the entire system less affected by the SRS.

If Rayleigh scattering is used in stead of the spontaneous Raman Stokes scattering, the temperature profile is found to be

$$T(z) = \left( \frac{k_B}{\hbar\omega_p} \ln \left( R_0 \cdot R^{-1}(z,T) \cdot e^{(\alpha_{aS} - \alpha_P)z} \left( e^{\frac{\hbar\omega_p}{k_B T_0}} - 1 \right) + 1 \right) \right)^{-1} \quad (3.18)$$

Compared with equation (3.8), there is the same number of calculations to be performed - thus there is no difference in the processing time.

The absolute change in Stokes and anti-Stokes scattering with temperature is comparable (see (2.9) and (2.10)).

$$\frac{dP_S(T)}{dT} \propto \frac{P_0 n_S}{\lambda_S^4} \frac{\frac{\hbar\omega_p}{k_B T} e^{-\frac{\hbar\omega_p}{k_B T}}}{(1 - e^{-\frac{\hbar\omega_p}{k_B T}})^2 T^2} \quad (3.19)$$

$$\frac{dP_{aS}(T)}{dT} \propto \frac{P_0 n_{aS}}{\lambda_{aS}^4} \frac{\frac{\hbar\omega_p}{k_B T} e^{\frac{\hbar\omega_p}{k_B T}}}{(e^{\frac{\hbar\omega_p}{k_B T}} - 1)^2 T^2} \quad (3.20)$$

But because of the fact that the anti-Stokes scattering is weaker, the relative change, or the sensitivity $\frac{dP_{aS}(T)}{dT}/P_{aS}(T)$ is usually much higher than that of Stokes, and thus more sensitive to temperature changes. Figure 3.4 shows the change in scattered power in per cent for Stokes and anti-Stokes scattering.



a)                                                        b)
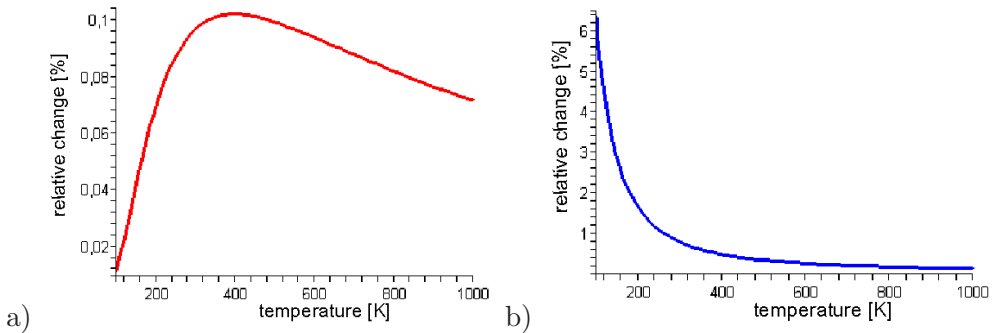
**Figure 3.4:** (a) Change in the power of Stokes scattering as a function of temperature (b) Change in the power of anti-Stokes scattering as a function of temperature.

Still, it is also possible to use the spontaneous Stokes and Rayleigh scattering. This combination gives better SNR of involved channels, at the expense of the sensitivity. The temperature profile is found using the following equation

$$T(z) = \left( -\frac{k_B}{\hbar \omega_p} \ln \left( R_0 \cdot R^{-1}(z,T) \cdot e^{(\alpha_S - \alpha_P)z} \left( e^{-\frac{\hbar \omega_p}{k_B T_0}} - 1 \right) + 1 \right) \right)^{-1} \quad (3.21)$$

Equations (3.18) and (3.21) are derived in Appendix B.

In spite of the mentioned advantages, it is not advisable to replace any of the Raman channels with the Rayleigh scattering. The main reason for not using the Rayleigh scattering is that any back-reflection from e.g. splices or connectors in the optical path of the pump photons or other scattering mechanism may mix with the signal and consequently produce faulty measurements. This scheme is thus not explored further.

### 3.2.2 Single-channel DTS

DTS system relying on a single anti-Stokes channel has also been proposed and realised [39]. After the installation of such a system, one must make reference measurements in controlled conditions, which are later used to calculate temperature relative to the reference measurement. Relative changes in the pump power are monitored as well.

This is a more simple solution, but requires a more complicated calibration process. Likewise, it is not flexible to changes in the measurement parameters, setup or the settings. Therefore, this scheme is not recommendable for hostile environments, where the fibre can get strained or stressed, which changes its loss coefficients.

## 3.3 Summary

The main principles and concepts of the distributed temperature sensor are introduced in this chapter. Incoherent Optical Frequency Domain Reflectometry (IOFDR) is explained, and expressions for the range, resolution and temperature profile are derived. The resolution of Optical Time Domain Reflectometry (OTDR) is also briefly commented.

Possibilities for the choice of different channels including Rayleigh scattering are listed together with some advantages and disadvantages

of the choices. In the following, only Raman Stokes and anti-Stokes channels will be used out of the four mentioned options, since this is the most reliable one.

# Chapter 4

# The Setup

This chapter introduces in more detail the optical components and the modules contained in the distributed temperature sensor (DTS). More specifically, the receiver, amplifiers, laser module, passive optical filters and sensing fibre are described. Furthermore, the influence of the different components and the measurement time on the sensor accuracy is found.

During the study of the DTS, several prototypes of the device were made. All are principally the same, but they differ in e.g. design wavelength, optical filter widths and fibre types. In the following, the most used setup is described in detail; other systems are briefly mentioned.

## 4.1 Detectors

The description of the setup starts where the optical signals end. The Raman signals are very weak (of the order $100nW$) and need to be amplified in the process of detection. Avalanche photo-diodes (APDs) are suitable detectors for this application.

There are two preferred APD detectors for use in DTS, namely $Si$ or $InGaAs$ APDs. The generated Stokes and anti-Stokes signals have to be in the interval of wavelengths detectable by APDs. Since the Raman scattering cross-section peaks at a frequency shift of around $\Delta f = 13THz$, systems based on $Si$ APDs would thus use high power $980nm$ single-mode lasers. The anti-Stokes and Stokes would lie at around $940nm$ and $1020nm$, respectively.

In long-range systems ($> 5km$), it is beneficial to increase the wavelength to the low-loss window of silica around $1500nm$. *InGaAs* APDs are suitable for this wavelength region since they are sensitive between approximately $1000nm$ and $1700nm$.

The responsivity $R_{APD}$ of an APD is defined as [9]

$$R_{APD} = \frac{\nu q}{hf} \approx \frac{\nu \lambda}{1.24} \tag{4.1}$$

where $\nu$ is the quantum efficiency of the photodiode and $hf$ is the energy of the incident photons. The responsivity of an InGaAs APD, which is used in the actual experiments, varies less than 3% over the entire region from $1.4\mu m$ to $1.6\mu m$. The responsivity falls off drastically above $1.7\mu m$ and below $1\mu m$ because of low quantum efficiency. A typical responsivity of the InGaAs APD is shown in figure 4.1.
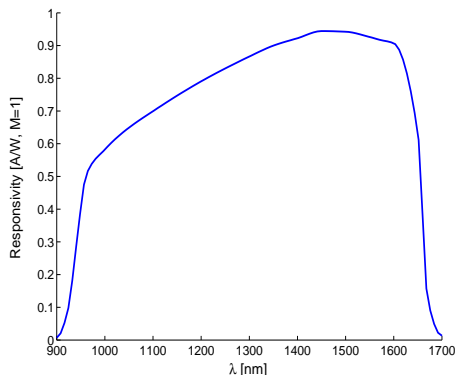


**Figure 4.1:** Typical responsivity of an InGaAs APD as a function of wavelength.

The InGaAs APD used to detect Raman signals in initial experiments is the JDS Uniphase 0040852-004. A standard PIN photo-detector performs detection of the reference channel.

## 4.2   Amplifier and sampler

Figure 4.2 shows a schematic of a Stokes channel receiver and signal amplifying circuit. The APD is biased to approximately $51V$ and has an internal amplification factor $M$ of 5-20, according to the settings.

The OPAMP (Texas Instruments OPA657) in transimpedance configuration (current-to-voltage) amplifies the signal $|R_L|$ times, where $R_L$ is the load resistance. According to the data-sheet, the transimpedance amplifier has a bandwidth of 10MHz, with a load resistor of $200k\Omega$, and with a transimpedance of $10k\Omega$ the bandwidth should be $200MHz$. A theoretical maximum of $40k\Omega$ limits the bandwidth to $50MHz$ corresponding to a minimum resolution of $1m$. The maximum load resistance of a real system should be kept lower than $10k\Omega$ to have sufficient bandwidth and avoid amplification of interfering signals.

Two more OPAMPs follow the transimpedance amplifier, each with a multiplication factor of approximately -7.5 times.
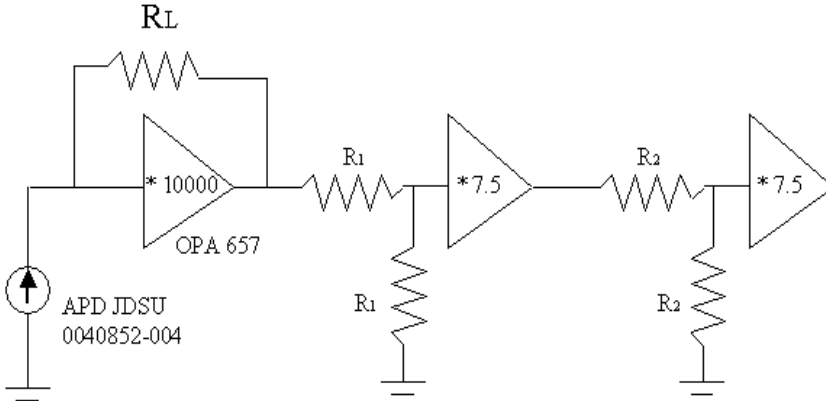


**Figure 4.2:** Schematic of the receiver module of the Stokes channel.

The amount of signal that reaches the receiver module is decisive for its design parameters. It depends on the Raman scattering coefficient of the sensor fibres, and the fibre length. This is commented in Section 4.6.

The electrical signal is then mixed with the local oscillator (LO) down to $|\omega_m - \omega_{LO}|/(2\pi) = 10kHz$. The signal from the mixer is

$$A_{LO}\cos(\omega_{LO}t + \phi) \cdot a_S \cos(\omega_m t + \psi) =$$

$$\frac{A_{LO}}{2}a_S\big(\cos((\omega_{LO} + \omega_m)t + \phi + \psi) + \cos((\omega_{LO} - \omega_m)t + \phi - \psi)\big) \quad (4.2)$$

The 10kHz component is extracted with a narrow electrical band-pass filter (EBPF).

## 4.3   Laser Module

There are several criteria for chosing the pump laser used in the DTS.
The type of the laser, its output power and the operating wavelength
are the main issues. They are discussed thoroughly in Chapter 6. Here
follows the characterisation of the pump laser used in the experiments.

The laser which is chosen for the long-range DTS is a $300mW$ semi-
conductor laser with $\lambda_c = 1493nm$. It is a standard fiber Bragg-grating-
stabilized single-mode Raman pump laser-diode. The line-width of $0.9nm$
ensures good suppression of the stimulated Brillouin scattering (SBS) -
it is well above the Brillouin shift of around $10\text{GHz} \approx 0.1nm$ at $1500nm$
and the associated loss of power is thus avoided. The emission spectrum
is shown in figure 4.3.
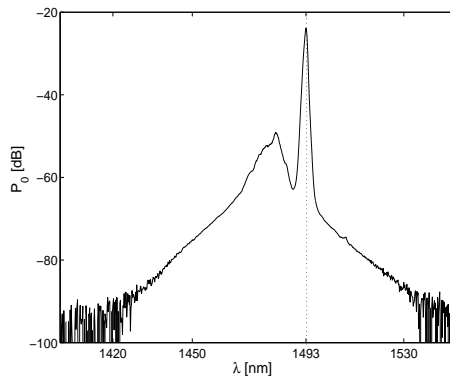


**Figure 4.3:** Emission spectrum of the $1493nm$ semi-conductor laser diode. The
spectral width is around $0.9nm$.

The laser diode is operated in the linear regime of the L-I curve to
obtain a linear transfer function of the current signal to light. (The L-I
curve is available in Appendix D.) Therefore, the peak output power is
limited to $200mW$ ($I = 40 - 800mA$). The modulation depth is around
0.95.

The operating temperature of the laser can shift the emission spec-
trum, as show in figure D.1. It is of interest to keep other wavelength
components other than $\lambda_c$ at a minimum, to minimise any possible
crosstalk. The temperature is therefore held constantly at $28^oC$. The
increased temperature may reduce the life-time of the laser, though.

It is found that the output power of the laser decreases when it is directly modulated. This contributes to lowering the signal to noise ratio at high modulation frequencies. The output spectra of the laser at CW operation and $50MHz$ modulation are shown in figure D.3. This can be included when modelling the system.

The laser light is linearly polarised, and the polarisation is maintained since the laser is pigtailed with polarisation-maintaining (PM) fibre. However, the laser light has to be depolarised before entering the sensing fibre since the Raman scattering is highly polarisation sensitive. If there are any polarisation sensitive components in the setup, random fluctuation in the polarisation of the pump and thus the signal would produce faulty signals and be misinterpreted as changes in the temperature. Therefore, another piece of PM fibre is spliced to the pigtail at $45^o$ relative to the polarisation axis. The two polarisations are thus scrambled; after several metres of propagation, unpolarised light exits the second PM fibre (this is usually done with pump light Raman amplifiers).

The experiments showed substantial decrease in standard deviation of the received backscattering after the polarisation scrambler was installed. Without the scrambler, twisting and bending the fibre influenced the magnitude of the response. There is more on this issue in Chapter 7.

Finally, an isolator prevents any backscattering to reach the laser diode and disturb the pump. The laser module is schematically shown in figure 4.4.
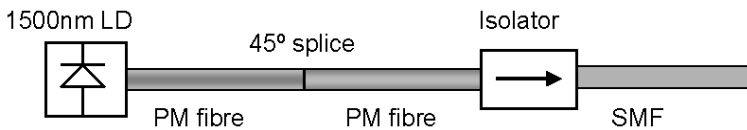


**Figure 4.4:** Laser module with the belonging paraphernalia.

## 4.4   Passive Optical Module

The task of the passive optical module is to direct the pump and signals to their respective destinations, and at the same time filter any undesired

frequency components away. A sketch of the optical module is given in
figure 4.5.
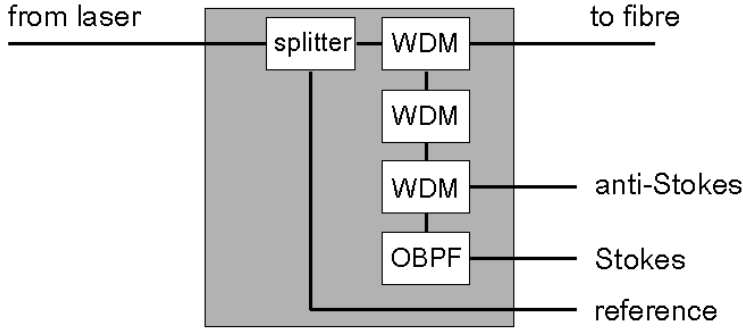


**Figure 4.5:** A sketch of the passive optical module built from discrete optical components.

Firstly, a fraction of 3% of the pump beam is channelled to the PIN
detector by the splitter, for use as a reference signal with which the phase
of other signals is compared and determined. With 3% of the pump
power, a stabile and powerful signal without significant attenuation of
the pump can be obtained.

As there is a substantial portion of light in the laser spectrum far
from the centre wavelength of the pump laser (see figure 4.3), it is nec-
essary to prevent launching the entire spectrum into the sensing fibre.
Rayleigh scattering from the side-bands would otherwise overlap and
interfere with Raman signals. An ADD/DROP multiplexer with cen-
tral frequency of $1490nm$ and width $17nm$ filters away the side-bands.
Rayleigh scattering is around three orders of magnitude stronger than
the spontaneous Raman scattering, but the side-bands are $30 - 40dB$
weaker than the pump at the central wavelength. The multiplexer blocks
the side-bands with $40dB$ or more. Thus, the Rayleigh scattering which
overlaps the Raman signals is at least $40dB$ weaker than the Raman
signal. A single component suffices to filter the pump residuals in this
prototype version, but if a dedicated filter module is made, the desired
suppression could be greater, e.g. $50dB$.

The backscattered signals pass through the same ADD/DROP multi-
plexer towards the detectors. However, a portion of Rayleigh backscat-
tered pump light at the centre pump wavelength passes through this

first stage in spite of the $40dB$ isolation. Another, nominally identical add/drop multiplexer follows the first stage to eliminate the remains of the backscattered pump (to minimise light passing at the edges of the add/drop channel, the component with the wider reflectance band is chosen for the second stage).

The anti-Stokes filter separates the light in the interval $1400-1440nm$ and directs it to the anti-Stokes APD. Finally, an optical band-pass filter (OBPF) passes the Stokes light ($1540 - 1610nm$) to the Stokes APD.

The isolation from the sensing fibre to the APDs, outside the signals wavelength interval, must be at least 60dB (resulting in error under 1%), but preferably more.

Every component and splice introduce an insertion loss on the signals. The attenuation from fibre to anti-Stokes APD is measured to $0.62dB$, while to the Stokes APD, it is on average just below $1dB$. These values agree well with the specifications of the used components. However, a custom-made module ought to give a somewhat better transmission.

The entire optical module together with the corresponding light spectra is shown in figure D.4 in Appendix D. The module is built using discrete optical components pigtailed with single-mode fibres.

## 4.5 The Sensing Fibre

The choice of the sensing fibre can be essential for the system performance. One can basically choose between standard step-index multimode fibre (SIMMF), graded-index multi-mode fibre (GIMMF) and different kinds of single-mode fibres.

Multi-mode fibres have the advantage of relatively large numerical aperture or capture fraction. In addition to this, they have a large spot size. The intensity of the pump light is thus limited, and strong stimulated Raman scattering is avoided. Pump lasers with an optical output power up to $2W$ at $980nm$ are used in arrangements comprising MMF, without significant SRS.

However, MMFs suffer from some drawbacks compared to SMFs. The main disadvantage of the MMF is its high loss and existence of multiple modes, each with its own behaviour. MMF is therefore suitable only for short range distributed sensors. SMFs have low loss and

allow only one mode to propagate, but have very small mode area and therefore suffer from high SRS.

Initially, the standard transmission SMF is used as the sensing fibre. The issue of choosing the appropriate fibre is covered in Chapter 6, where a number of fibre types are tested and analysed.

## 4.6   Noise Considerations

Inherent to virtually every detection and amplification process is the addition of noise to the original signal. When detecting an optical signal with an APD, there are two major sources of stochastic noise, namely shot noise (or quantum noise) and thermal noise. There are two contributions to the shot noise: the so-called dark current in the APD and the optical noise in the signal, the latter being more important in the scheme used here. Thermal noise originates from motion of thermally excited electrons in the amplifier stage.

The shot-noise (voltage) term expressed in $V^2$ is written as [9]:

$$\sigma_S^2 = 2q \cdot M^2 \cdot F_A \cdot (R \cdot P_{in} + I_d) \cdot \Delta f \cdot R_L^2 \;\; [V^2] \qquad (4.3)$$

where $q$ is the unit charge, $M$ is the internal amplification factor of the APD, $F_A$ is the excess noise factor, $R$ is the responsivity, $P_{in}$ the incident power and $I_d$ the dark current. $\Delta f$ is the receiver bandwidth and $R_L$ the load resistance of the transimpedance amplifier. $F_A$ is found from [9]

$$F_A(M) = k_A - (1 - k_A)(2 - 1/M) \qquad (4.4)$$

where $k_A$ is the ionisation-coefficient ratio (around 0.5 for InGaAs APDs).

The thermal noise (voltage) term is expressed as [9]:

$$\sigma_T^2 = \frac{4 \cdot k_B \cdot T_{R_L}}{R_L} \cdot F_n \cdot \Delta f \cdot R_L^2 \;\; [V^2] \qquad (4.5)$$

Here, $F_n$ is the amplifier noise figure, $k_B$ is the Boltzmann constant, and $T_{R_L}$ is the temperature of the load resistor.

There are two more noise terms associated with the electrical amplifiers. These are the voltage noise (data from the data-sheet of the OPAMP)

$$\sigma_V^2 = (4.8 \cdot 10^{-9}V)^2 \cdot \Delta f \;\; [V^2], \qquad (4.6)$$

and the current noise, expressed also in $V^2$ which is

$$\sigma_I^2 = (1.3 \cdot 10^{-15} A \cdot R_L)^2 \cdot \Delta f \ \ [V^2]. \tag{4.7}$$

Assuming that the four terms are independent and all follow Gaussian distributions, the total noise is given by

$$\sigma_N = \sqrt{\sigma_T^2 + \sigma_S^2 + \sigma_V^2 + \sigma_I^2}. \tag{4.8}$$

The subsequent electrical amplifiers and circuitry add negligible noise.

An IOFDR sensor with $12km$ range using SMF is considered as an example. Each of the four contributions is compared to the total noise. Here, $R_L = 2k\Omega$, $M = 11$, $I_d = 2nA$, $P_{in} = 200nW$, $F_n = 3dB$ and the detectors and load resistors are at room temperature. The noise contributions are shown in figure 4.6. One can see that the most dominant
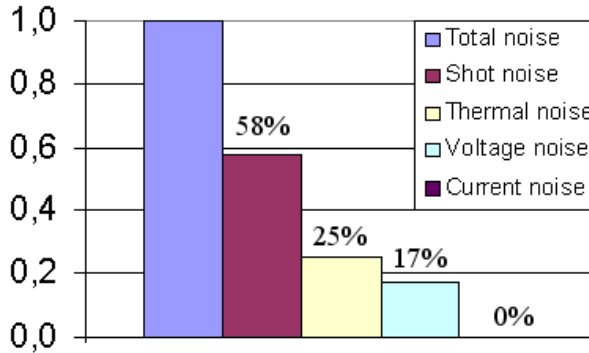


**Figure 4.6:** Noise contributions with their respective fractions of the total noise.

noise term is the unavoidable shot noise from the optical signal. It is at least two times higher than any other noise term. As the load resistance increases, the dominance of the shot noise increases further. The dark current constitutes only a small fraction of the total shot noise. With responsivity $R = 0.9A/W$ and $P_{in} = 200nW$, the optical signal induces noise current of $180nA$ compared to a $2 - 10nA$ dark current in typical APDs. Consequently, cooling of the APD, which mainly reduces the dark current and the thermal noise, or using APDs with smaller dark current makes only little difference in the total noise budget of an IOFDR system.

The magnitude of the received AC signal is frequency dependent. Therefore, the SNR decreases with the frequency in the same way as the signal. The SNR of the sensor, where both signal and noise are expressed in volts, is given by

$$SNR(f) = R_L \cdot R \cdot M \cdot P_{s,in}(f)/\sigma_N \ \ [V/V]. \tag{4.9}$$

The simulated SNR curve with parameters as above is plotted in figure 4.7
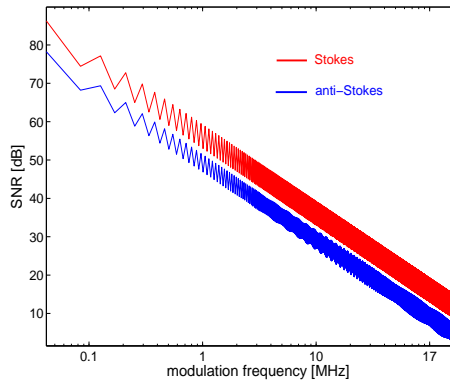


**Figure 4.7:** Simulated SNR as a function of frequency for a typical DTS system.

The power of the optical signal reaching the detectors is of the order $100nW$ on average. In the ideal case, the responsivity of the ADP detector with an optimal gain factor of approximately 10 is around $9A/W$. This produces a current that is only a fraction of a microampere. The transimpedance amplifier with amplification factor of $2 \cdot 10^3 V/A$ follows the APD signal source.

The load resistance of $2k\Omega$ can be increased further. On one hand, a high load resistance reduces the bandwidth of the amplifier, but on the other hand sets more relaxed demands for the internal gain of the ADPs, and increases the SNR.

In order to maximise the SNR, the internal APD gain is optimised. The optimal gain depends on the optical input power and characteristics of the APD. The polynomial to be solved with respect to $M$ is [9]

$$k_A \cdot M^3 + (1 - k_A) \cdot M = \frac{4k_B T \cdot F_n}{qR_L(R \cdot P_{in} + I_d)}. \tag{4.10}$$

Figure 4.8(a) shows the optimal internal APD gain, and 4.8(b) shows the theoretical SNR at DC as a function of the load resistance.



(a) (b)
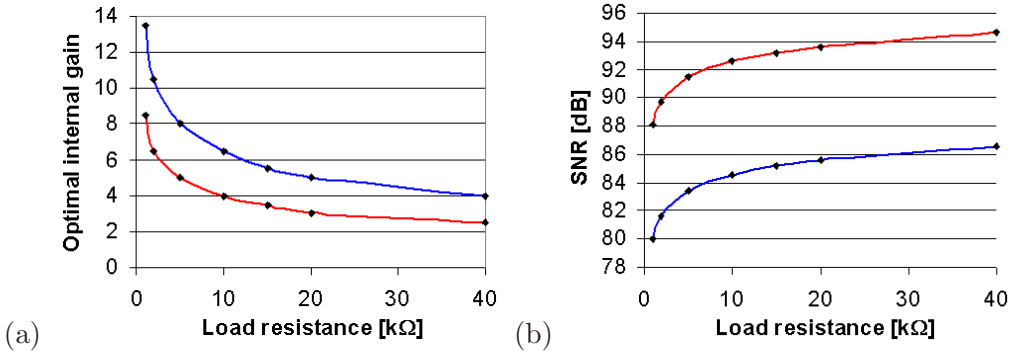
**Figure 4.8:** (a) The optimal internal APD gain M for Stokes (red) and anti-Stokes (blue) as a function of the load resistance $R_L$, (b) SNR as a function of the load resistance for Stokes (red) and anti-Stokes (blue) channel at DC.

In reality, the coupling of light to the sensitive surface of the photodiode is not perfect. Poor coupling increases the optimal gain factor $M$ because less shot-noise is amplified.

Increasing the load resistance from $2k\Omega$ to $40k\Omega$ improves the SNR of each channel by around $4dB$. However, a $40k\Omega$ load resistor limits the amplifier bandwidth to only $50MHz$ at the most. A load resistance of $10k\Omega$ is more realistic as it would allow for the necessary bandwidth and resolution, and increase the SNR by around $2dB$.

If the optimal internal gain approaches unity, one could use PIN photodiodes instead of costly APDs without significant signal degradation. A PIN photodiode has a higher responsivity ($R_{PIN} = 1.1$) compared to APD.

Note also that the load resistance that makes the thermal and shot noise equal is a few $M\Omega$. The shot-noise term is the largest noise-term for virtually any IOFDR setup, and the system is therefore shot-noise limited.

### 4.6.1 Noise distribution

The type of the noise distribution is analysed in the following. Since each summand in equation (4.8) in theory has a normal distribution,

one can assume that the total noise also follows a Gaussian distribution.

To make a reliable statistical analysis, a data-pool of several hundreds of measurements on a $12km$ SMF was made at a single modulation frequency. The distribution of the measured values on the Stokes channel was analysed. The distribution of the samples is shown in figure 4.9, together with a Gaussian fit of the measured distribution.
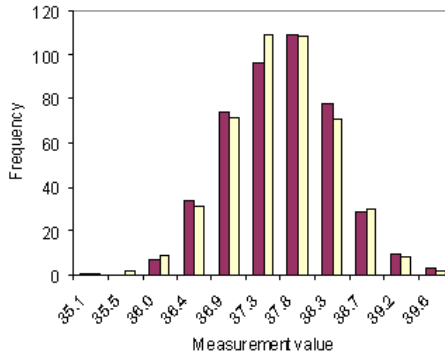


**Figure 4.9:** Statistic analysis of measurement data (dark columns) compared with the Gaussian distribution (white columns).

The measured distribution follows well the Gaussian distribution, and further assumptions about the distribution being Gaussian are thus justified.

## 4.7   Temperature Accuracy

The system performance is evaluated by calculating the signal-to-noise-ratio at each data-point of the backscattering function, obtained from the frequency response. The signal power is derived from the pump power, the spontaneous Raman coefficient of the fiber, and the fiber loss. The noise is calculated from the total optical power at the detector and the detector parameters.

In a shot-noise limited system, the detector noise, $\sigma^2_{APD}$, can be expressed as

$$\begin{aligned}
\sigma^2_{APD} &\approx 2qF_A M^2 I_{APD} B_e \\
&= 2qF_A M^2 R P_0 \chi_R B_e \frac{\Delta z}{L} \int_0^L e^{-(\alpha_R + \alpha_P)z} dz, \quad (4.11)
\end{aligned}$$

where $I_{APD}$ is the the average detector current of the detected optical power. The factor $\Delta z/L$ is included to account for the fact that in IOFDR, there are approximately $L/\Delta z$ measurements for each data-point along the fiber, which effectively decreases the bandwidth by this factor.

The received signal current due to reflection from a specific point along the fiber, defined as the spatial resolution, is

$$I_{\Delta z}(z) = RP_0 m \chi_R \Delta z \cdot e^{-(\alpha_P + \alpha_R)z}. \tag{4.12}$$

Due to much lower scattering cross-section, the anti-Stokes signal is weaker than the Stokes signal and limits the accuracy of a temperature measurement as illustrated in figure 4.7. The approximated signal-to-noise ratio of the anti-Stokes channel is found from equations (4.11) and (4.12)

$$SNR(z) = \frac{I_{\Delta z}^2(z)}{\sigma_{APD}^2} = \frac{RP_0 m^2 \chi_R \Delta z L(\alpha_P + \alpha_{aS}) \cdot e^{-2(\alpha_P + \alpha_R)z}}{2qF_A B_e(1 - e^{-(\alpha_P + \alpha_{aS})L})}. \tag{4.13}$$

The temperature accuracy $\Delta T_{IOFDR}$ is inversely proportional to the square root of the SNR. It is approximated by

$$\Delta T_{IOFDR}(z) \approx \frac{\kappa}{m} \sqrt{\frac{2qF_A B_e}{RP_0 \chi_{aS} \Delta z} \cdot \frac{1 - e^{-(\alpha_P + \alpha_{aS})L}}{L(\alpha_P + \alpha_{aS})}} \cdot e^{(\alpha_P + \alpha_{aS})z}, \tag{4.14}$$

where $\kappa$ is a calibration constant comprising the derivative of the temperature versus voltage function (approximately 130K/V at room temperature).

It follows that the standard deviation of the temperature measurement grows exponentially with the distance (the exponent being dependent on the fiber loss), as the square root of the resolution, and falls off with the square root of the pump power and square root of the measurement time. Roughly, including only the variable parameters, the standard deviation has the form

$$\Delta T_{IOFDR}(z) \approx \frac{K}{m} \sqrt{\frac{B_e}{P_0 \Delta z}} e^{Az} \tag{4.15}$$

The total measurement time $t_{tot}$ can be approximated by the ideal

$$t_{tot} \approx \frac{N_{meas}}{B_e} \approx \frac{L_{max}}{B_e \Delta z} \tag{4.16}$$

The stabilisation and sampling time for the receiver circuitry is not included in $t_{tot}$. Substituting equation (4.16) into equation (4.14) yields an expression for the $\Delta T_{IOFDR}$ with $t_{tot}$ as a parameter.

$$\Delta T_{IOFDR} \approx \frac{\kappa}{m\Delta z}\sqrt{\frac{2qF_A}{RP_0\chi t_{tot}}\frac{1-e^{-L(\alpha_p+\alpha_{aS})}}{L(\alpha_p+\alpha_{aS})}} \cdot e^{L(\alpha_p+\alpha_{aS})} \qquad (4.17)$$

Note that the results above assume that the fibre length is close to the maximum allowable length, i.e. $L_{fibre} \approx L_{max}$.

Since the noise distribution at every modulation frequency follows the Gaussian distribution, the noise distribution on the backscattering functions also follows the Gaussian distribution because a Gaussian function is Fourier transformed into a Gaussian function. Consequently, the points along the temperature profile from a number of measurements under same conditions, also follow the Gaussian distribution.

Gaussian distribution predicts that a certain number of measurements will deviate significantly from the mean value. Figure 4.10 shows that the specified accuracy should be 2.6 times the standard deviation of the measurements, in order to have less than 1% of the measurements exceeding the specified accuracy.
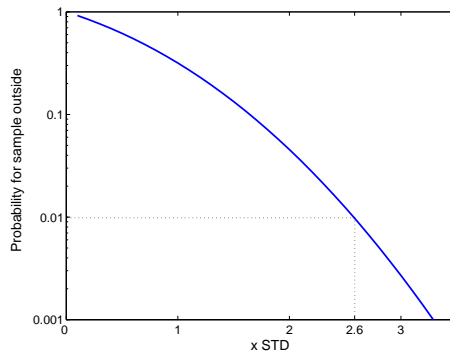


**Figure 4.10:** Calculated probability for a measurement result, which follows the Gaussian distribution, to deviate from the mean value.

## 4.8 IOFDR vs. OTDR

IOFDR and OTDR are the two most commonly used techniques for performing distributed measurements with resolution of order $1m$. It is possible to obtain the same backscattering information, regardless of the detection scheme, but the difference in the practical implementations may be significant. Here, the two ranging techniques are compared in terms of advantages and drawbacks that each technique possesses, and features attractive for specific applications.

Note, however, that the predicted performance of the OTDR is not verified by any experiment; it is estimated purely from theoretical considerations of the method, and by using specified parameters of the electronics equivalent to that used in the IOFDR system.

### 4.8.1 Requirements for implementation of OTDR DTS

In principle, all optical components used in the IOFDR system can also be applied in an OTDR system. However, there are special requirements concerning the electronics.

According to equation (3.14), the sampling of the detector signal must happen every $10ns$ ($f_{samp} = 100MHz$) with high precision, to obtain $1m$ spatial resolution. The laser must be able to generate $10ns$ laser pulses. For the same resolution with IOFDR, the highest modulation frequency needed is $50MHz$ (equation (3.13)) which has a period of $20ns$. Furthermore, the laser current driver must provide sufficient repetition rate of the high-power pulses.

The receiver in the OTDR system must have a very small dark current and at the same time high amplification factor to ensure that a signal in the $pW$ range is detected with a minimum of noise. For this purpose, photon-counting techniques have been developed [40].

### 4.8.2 OTDR Accuracy

As for the IOFDR, the system performance is evaluated by calculating the signal-to-noise-ratio of the backscattered signal originating from the end of the fiber; the detected signal from there is weakest. Again, the weaker anti-Stokes channel is considered.

The signal power is derived from the pump power, the Raman scattering coefficient of the fibre and the fiber loss. The noise is calculated using the same detector parameters as in IOFDR.

In OTDR, the noise current density in the detector circuitry is dominated by the shot noise generated from the dark current of the detector, $I_d$, which is of the order $1nA$ for common InGaAs APD detectors (the one actually used has $I_d = 2nA$).

As above, the noise is reduced by averaging a number of measurements, i.e.

$$\sigma^2_{noise,avg} = \frac{\sigma^2_{noise,single}}{N_{meas}},\tag{4.18}$$

where $N_{meas}$ is the number of identical consecutive measurements.

The temperature accuracy is approximated with

$$\Delta T_{OTDR} \approx \frac{\kappa}{\sqrt{SNR}} = \kappa \frac{1}{P_0 \chi_{aS} \Delta z R e^{-L(\alpha_p + \alpha_{aS})}} \sqrt{\frac{2q F_A I_d \cdot B_e}{N_{meas}}},\tag{4.19}$$

where $\kappa$ is a calibration constant. Equation (4.19) assumes a square pulse. The total measurement time is expressed as

$$t_{tot} = N_{meas} \cdot \frac{2 n_P L}{c}.\tag{4.20}$$

The measurement time does not include any delay between measurements, as well as delay for signal processing. These delays increase the actual measurement time. The electrical bandwidth $B_e$ can be chosen to match the spatial resolution, i.e. $B_e = 1/t_{min} = c/(2 n_P \Delta z)$. Combining this, equation (4.19) and (4.20), yields the following expression for the temperature uncertainty

$$\Delta T_{OTDR} \approx k \frac{1}{P_0 \chi_{aS} \Delta z R} \sqrt{\frac{2 q F_A L I_d}{\Delta z t_{tot}}} \cdot e^{L(\alpha_p + \alpha_{aS})}\tag{4.21}$$

### 4.8.3  Theoretical comparison of IOFDR and OTDR accuracy

Equation (4.21) is compared with the estimate for the temperature uncertainty of an IOFDR system, stated in equation (4.17). Taking the ratio between the $\Delta T_{IOFDR}$ and $\Delta T_{IOFDR}$ suggests which method is better for a specific set of parameters.

$$\rho = \frac{\Delta T_{IOFDR}}{\Delta T_{OTDR}} = \frac{\xi}{m}\sqrt{\frac{P_0 R\chi\Delta z}{L(I_d + RP\xi\chi\Delta z e^{-(\alpha_p+\alpha_{aS})*L})}\frac{1-e^{-L(\alpha_p+\alpha_{aS})}}{\alpha_p+\alpha_{aS}}},$$
(4.22)

where $\xi$ is the ratio between the pump power of OTDR and IOFDR systems, so that $P_{0,OTDR} = \xi P_{0,IOFDR}$. For $\rho < 1$, the IOFDR performs better than the IOFDR.

Taking the standard and measured values for the parameters in the equation (4.22), i.e. $\chi_{aS,SMF} = 1.42 \cdot 10^{-10} m^{-1}$, $R = 0.84 A/W$, $m = 0.9$, $\alpha_{aS} + \alpha_P = 0.48 dB/m$, $P_0 = 200 mW$, one can plot the approximated ratio $\rho$ as a function of the range $L$, and for a number of values of $I_d$. $I_d$ is a function of temperature of the APD and influences the final conclusion significantly. The resolution $\Delta z$ is set to $1m$.
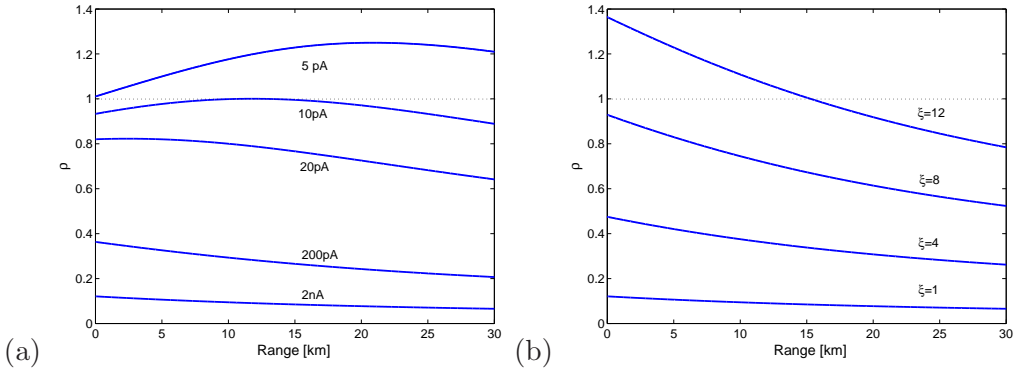


**Figure 4.11:** (a) The ratio $\rho$ as function of sensor range for several values of $I_d$ ($\xi = 1$), (b) The ratio $\rho$ as function of sensor range for several values of $\xi$ (at room temperature).

At room temperature, the difference between the IOFDR and OTDR grows as the sensor range increases. The dark current has to be reduced to only $10pA$ if the standard temperature deviation of the OTDR and IOFDR should correspond after $12km$. With cooled detectors ($-20$ to $-30^oC$) and higher peak pulse power, OTDR may perform better.

However, increasing the resolution (e.g. to $10m$) also gives advantage to the OTDR system by a factor of $\sqrt{10}$.

Use of pulsed lasers with high peak pump power could improve the performance of the OTDR system. One has to increase the pump power by a factor of approximately $\xi = 14$, i.e. to $2.8W$, to get the same performance at $10km$ fiber length and resolution of $1m$, at room temperature. As mentioned earlier, this value is not exact but is to be regarded as an indicator of the order of magnitude of the factor. A similar comparison is conducted in [1], resulting in a necessary peak power of $7W$. The difference may be partly justified by the different detectors and pump wavelengths, and thus the scattering and attenuation coefficients, that were used there.

In practice, it is acceptable to run the semiconductor lasers at much larger peak powers than specified, e.g. $\xi = 5$ to $10$ times, for a short duration of the pulse. Using the same pump lasers, it is therefore feasible that OTDR can have a performance comparable with IOFDR. Note also that problems arising from SRS do not appear in OTDR.

It is not straightforward to say whether a fiber with higher scattering coefficient (e.g. MMF) gives advantage to OTDR or IOFDR because the attenuation changes as well. But preliminary results show that OTDR benefits more from an increase in the $\chi_R/\alpha_R$ ratio.

## 4.9   Summary

This chapter describes in detail the components which constitute the optical module of the DTS used in most of the experiments. The pump laser, optical filters, and the receiver module with APDs and the transimpedance amplifier are presented.

Particularly important are the noise characteristics of the sensor. The main noise sources are identified, and it is found that the shot-noise gives the largest contribution to the total noise.

In the treatment of the accuracy of the IOFDR sensor, it is found that theoretically the standard deviation of the temperature grows exponentially with the range. The accuracy increases with the square root of the measurement time and pump power, and decreases with the square root of the resolution. Furthermore, the accuracy is inversely proportional to the modulation depth.

The IOFDR solution is compared to the OTDR. Based on the considerations in this chapter, it is expected that the IOFDR system will

perform notably better than OTDR (especially in long-range systems), when the same peak pump power, detectors and fiber are employed. For long-range, high-resolution, low-cost systems, IOFDR will constitute a better choice than an equivalent OTDR system.

However, the use of high-power pulsed lasers (or amplification of low-power pulses), and especially cooling or employing more advanced types of the detectors (photon counting), tend to give the OTDR system an advantage, and may ultimately make possible better performance than compared to IOFDR for any range.

# Chapter 5

# Computer Model for Simulations

This chapter introduces the numerical model which is used to obtain the theoretical values of temperature profiles under various conditions. The model makes it possible to predict the performance and optimise the system when different parameters are changed. Results obtained using the model are compared and calibrated with the measured data. Furthermore, some digital signal processing techniques for noise reduction are explored.

The numerical model is developed in Matlab, and the printouts of the main procedures are available in Appendix G.

## 5.1 Frequency response of the fibre

In the following, Stokes and anti-Stokes channels as well as the pump are approximated as monochromatic signals.

The main procedure in the simulation creates the correct frequency response of the fibre. The response depends on the fibre parameters, such as attenuation, length, refractive indices and Raman scattering coefficients, which are loaded from a data-file. The propagation constants are then calculated, and the desired resolution is set.

First, it is assumed that the temperature is constant along the fibre. The integrals which give the phase and amplitude of the backscattered

signals are solved analytically. The equation describing the AC part of the backscattering from the entire fibre, at the detector and at constant temperature is

$$
\begin{aligned}
P_d(\omega_m, t) &= P_0 m \chi_R \int_0^L e^{-\alpha_\Sigma z} \cos(\omega_m t - \omega_m \beta_\Sigma z) dz \\
&= \frac{P_0 m \chi_R}{\alpha_\Sigma^2 + \omega_m^2 \beta_\Sigma^2} \Big( \alpha_\Sigma \cos(\omega_m t) + \omega_m \beta_\Sigma \sin(\omega_m t) \\
&\quad - e^{-\alpha_\Sigma L} \big( \alpha_\Sigma \cos(\omega_m t - \omega_m \beta_\Sigma L) + \omega_m \beta_\Sigma \sin(\omega_m t - \omega_m \beta_\Sigma L) \big) \Big)
\end{aligned}
$$

$$(5.1)$$

$\alpha_\Sigma = \alpha_P + \alpha_R$ and $\beta_\Sigma = \beta_P + \beta_R$ are sums of the attenuation coefficients and propagation constants at the pump and appropriate Raman channel, respectively.

For each modulation frequency, $P_d(\omega_m, t)$ is found for $t = 0 \cdots 2\pi/\omega_m$, and the amplitude and phase are calculated for both Stokes and anti-Stokes waves. Here, it is important to use fine temporal resolution to determine the phase with high precision. Failure to do so produces phase noise and ripple on the final backscattering curves.

For a varying temperature profile, i.e., if there are some hot-spots along the fibre, the fibre is divided into $M$ parts, where $M \leq N$, $N$ being the number of distributed measurement points. The total backscattered signals at the detectors are

$$
\begin{aligned}
P_d(\omega_m, t) &= P_0 \cdot \sum_{k=1}^{M} \chi_k e^{-\sum_{j=1}^{k} \alpha_j (D_j - D_{j-1})} \\
&\quad \cdot \int_{D_{k-1}}^{D_k} e^{-\alpha_k (z - D_k)} \Big( 1 + m \cos(\omega_m t - \omega_m \beta_m z) \Big) dz \\
&= P_0 \cdot \sum_{k=1}^{M} \chi_k e^{-\sum_{j=1}^{k} \alpha_j (D_j - D_{j-1} + \alpha_m D_k)} \Big( \frac{1}{\alpha} \big( e^{-\alpha D_{k-1}} - e^{-\alpha D_k} \big) \\
&\quad + \frac{m}{\alpha^2 + \omega^2 \beta^2} \Big( e^{-\alpha D_{k-1}} \big( \alpha \cos(\omega t - \omega \beta D_{k-1}) + \omega \beta \sin(\omega t - \omega \beta D_{k-1}) \big) \\
&\quad - e^{\alpha D_k} \big( \alpha \cos(\omega t - \omega \beta D_k) + \omega \beta \sin(\omega t - \omega \beta D_k) \big) \Big) \Big)
\end{aligned}
$$

$$(5.2)$$

where every section $k$ of the fibre has its specific Raman scattering co-efficient $\chi_k$ and attenuation constant $\alpha_k$.

The most interesting case for purposes of this analysis is when the fibre has a single hot spot, i.e., the situation where fire is simulated in a section of the fibre. This section starts at $D_1$, ends at $D_2$ and has a length $d$. The entire fibre is of length $L$, and the end-point is called $D_3$. The situation is illustrated in figure 5.1. With $M = 3$, according to equation (5.2), the backscattered signal at the detector from the entire fibre is found to be

$$
\begin{aligned}
P_d(\omega_m, t) \;=\; & \chi_1 \Big( \frac{1}{\alpha} \big(1 - e^{-\alpha X}\big) + \frac{m}{\alpha^2 + \omega^2 \beta^2} \big( \alpha \cos(\omega t) + \omega \beta \sin(\omega t) \\
& -\; e^{-\alpha X} \big( \alpha \cos(\omega t - \omega \beta X) + \omega \beta \sin(\omega t - \omega \beta X) \big) \big) \Big) \\
& +\; \chi_2 \Big( \frac{1}{\alpha} \big( e^{-\alpha X} - e^{-\alpha(X+d)} \big) \\
& +\; \frac{m}{\alpha^2 + \omega^2 \beta^2} \big( e^{-\alpha X} \big( \alpha \cos(\omega t - \omega \beta X) + \omega \beta \sin(\omega t - \omega \beta X) \big) \\
& -\; e^{-\alpha(X+d)} \big( \alpha \cos(\omega t - \omega \beta (X + d)) + \omega \beta \sin(\omega t - \omega \beta (X + d)) \big) \big) \Big) \\
& +\; \chi_3 \Big( \frac{1}{\alpha} \big( e^{-\alpha(X+d)} - e^{-\alpha L} \big) \\
& +\; \frac{m}{\alpha^2 + \omega^2 \beta^2} \big( e^{-\alpha(X+d)} \big( \alpha \cos(\omega t - \omega \beta (X + d)) \\
& +\; \omega \beta \sin(\omega t - \omega \beta (X + d)) \big) \\
& -\; e^{-\alpha L} \big( \alpha \cos(\omega t - \omega \beta L) + \omega \beta \sin(\omega t - \omega \beta L) \big) \big) \Big)
\end{aligned}
\tag{5.3}
$$
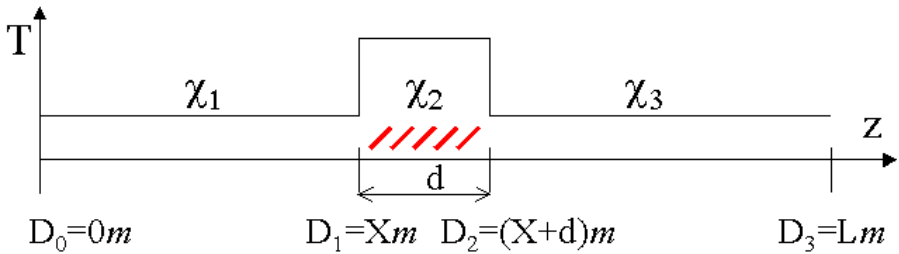


**Figure 5.1:** The section from $D_1$ to $D_2$ has a different $\chi_R$ factors simulating a hot-spot in the fibre.

As a good approximation to reality, and for simplicity, it is here assumed that the attenuation coefficients at relevant wavelengths do

not vary significantly along the fibre. In a more advanced model, loss, index of refraction and the $\chi_R$ parameter can be assigned for every point of both channels and the pump separately.

The magnitudes of the frequency responses of the Raman channels are obtained from the amplitude (or the maximum value) of $P_d(\omega_m, t)$ in equation (5.3), and the phase is deduced from the index in the array $P_d(\omega_m, t)$ at which the maximum value is found.

### 5.1.1   Addition of noise

The received Raman signals have at each modulation frequency a specific signal-to-noise ratio. Noise contributions are described in section 4.6 and are modelled according to their respective governing equations, using parameters specified in data-sheets of the included components (amplifiers and APDs).

The numerical model assumes that the noise distribution in each data-point of the frequency response follows the Gaussian distribution, as argued in Section 4.6.1.

The magnitude of the frequency-response arrays $M_R(\omega_m)$ are scaled to the expected values at $\omega_m = 0$ (from equation (3.6)).

$$M_R(\omega_m) = P_d(\omega_m, t) \cdot \left( P_0 \int_0^L \chi_R(T(z)) \cdot e^{-(\alpha_P + \alpha_R)z} dz \right) / P_d(0) \quad (5.4)$$

The SNR for each modulation frequency is found by dividing the detected signal with the noise array calculated from (4.8)

$$SNR = \frac{MRM_R(\omega_m)R_L}{\sqrt{\sigma_T^2 + \sigma_S^2 + \sigma_V^2 + \sigma_I^2}}. \quad (5.5)$$

The amplitude noise, which is added to the magnitude of the frequency response, has Gaussian distribution with zero mean value, and a variance inversely proportional to the calculated SNR. Phase noise is not added since it is found that amplitude noise is sufficient to describe the measurement uncertainties. The noisy magnitudes of the frequency responses are

$$M_{R,N}(\omega_m) = M_R(\omega_m) + \frac{M_R(\omega_m)}{SNR}\Gamma \quad (5.6)$$

where $\Gamma$ is a stochastic variable having the Gaussian probability distribution function with mean zero, variance one and standard deviation one.

### 5.1.2 Temperature profile

The complex frequency responses of Stokes and anti-Stokes channels are created by adding the phases to the noisy magnitudes of the frequency responses.

$$F_R^*(\omega_m) = M_{R,N}(\omega_m) \cdot e^{-\jmath\varphi(\omega_m)} \tag{5.7}$$

Finally, $F_R^*(\omega_m)$ is concatenated with flipped and complex conjugated $F_R^*(\omega_m)$ to give the frequency responses from $-f_{max}$ to $f_{max}$. The noise is thus also symmetrical as in the real system.

The arrays are Fourier-transformed to produce the backscattering curves in space domain. Fibre loss is compensated by multiplication with an exponential function $exp((\alpha_R(z) + \alpha_P(z))z)$.

Finally, the temperature profile is determined using the ratio of the two channels and natural constants as described in equation (3.8).

### 5.1.3 Signal statistics

The procedure described in sections 5.1.1 and 5.1.2 is repeated for a number of times ($> 50$) so that statistical analysis can be made. For example, standard deviation and the average of the temperature curves can be found.

## 5.2 Comparison between predicted and measured results

After the model has been developed, it was inspected how well the simulation predicts the actual measurements. Temperature profile and standard deviation are measured for a number of different setups with the single-mode fibre and the graded-index multi-mode fibre, and compared to the modelled results.

### 5.2.1   Comparison of frequency responses

Figure 5.2 shows measurements of Stokes and anti-Stokes channels - their amplitudes and phases. Note that the anti-Stokes channel has a higher amplification factor and is therefore comparable in magnitude to the Stokes. Averaging over many measurements with a large integration time gives very low noise, and thus clear signals.



(a)    (b)
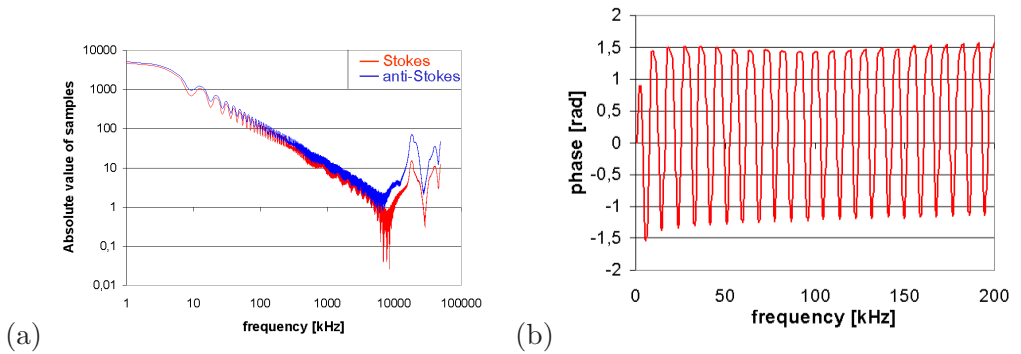
**Figure 5.2:** (a) Average of 20 measured magnitudes of the frequency response from an 11km SMF ($B_e = 60Hz$) as a function of modulation frequency (b) The corresponding phase of the signals.

The deviant behaviour of the measured curves at high frequencies is due to cross-talk between the electrical reference signal and the Raman channels. This is not a concern of this work. However, it can be shown that the frequency response at high modulation frequencies has a modest influence on the overall sensor accuracy.

The corresponding simulated signal samples are shown in figure 5.3

(a) (b)
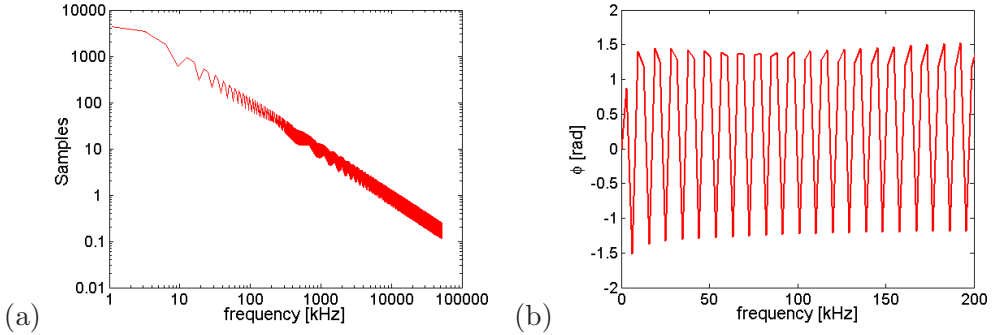
**Figure 5.3:** (a) Simulated noiseless magnitude of the frequency response from an 11km SMF as a function of modulation frequency (b) The corresponding phase of the signal.

The agreement between the simulated and measured frequency responses is very good. Many of such measurements and simulations were made with different sets of parameters and fibres to calibrate the model. The model gives an excellent agreement with the measurements in all cases; figures 5.2 and 5.3 are merely examples of this.

## 5.2.2   Comparison of temperature profiles

Next, the measured noisy temperature profile and the standard deviation from the average of a number of measurements are compared with the modelled results. Again, only one example of the comparison is given.

A $13.8km$ long standard SMF was used in the experiment. 13 temperature measurements were made with the spatial resolution $\Delta z = 3m$. The bandwidth of the receiver was $B_e = 96Hz$. 8192 data-points were taken to meet the demand of IOFDR for $2^n$ points for efficient IFFT. The frequency response was filtered with cosine window function (filtering is discussed in Section 5.3).

The temperature is shown in figure 5.4, and the calculated standard deviation and its exponential fit are shown in figure 5.5.

The corresponding modelled results are shown in figure 5.6. A hot-spot is modelled to enable calibration of relevant constants in the model. This model does not take the SRS into account, but predicts the STD with high accuracy (to within $0.15^oC$).
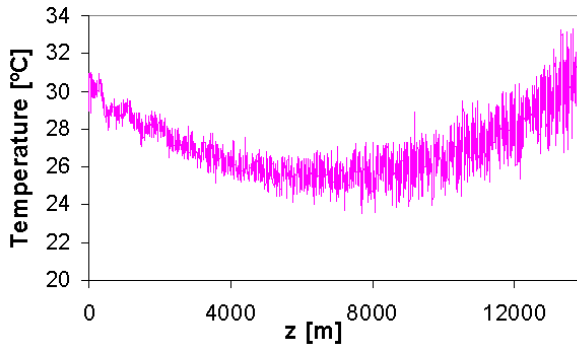
**Figure 5.4:** Measured temperature profile.
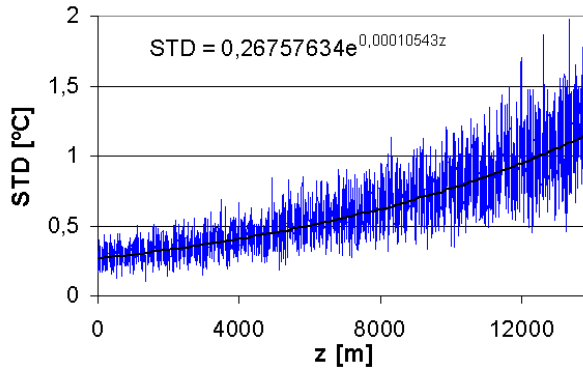


**Figure 5.5:** Measured temperature profile.
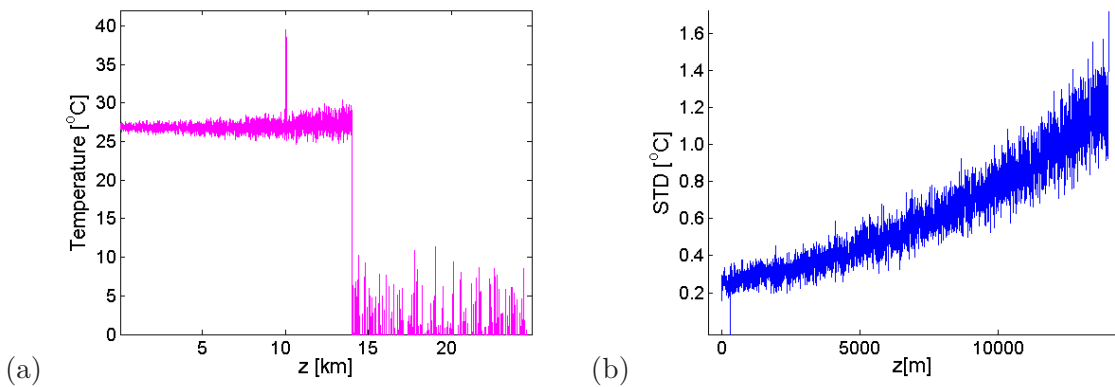


**Figure 5.6:** (a) Modelled temperature profile with a hot-spot for calibration, (b) Standard deviation of 60 modelled temperature profiles.

In conclusion, the model gives reliable results, and can be used to estimate the sensor accuracy when different parameters are changed.

## 5.3 Signal processing

Some refinement of the signals with the aim of reducing uncertainties in the temperature measurements can be achieved by digital signal processing. This section deals with algorithms for noise suppression. Using the developed computer model, it is demonstrated that linear filters and wavelet denoising can give significant improvements in the sensor accuracy.

### 5.3.1 Linear filters

The most noisy part of the frequency response is the high-frequency end, where SNR is low. High-frequency noise can be suppressed by applying a weigh function to the frequency response data, that is low-pass filtering is performed. Low pass filtering can be applied directly on the magnitudes of the measured frequency response - arrays $S_R(\omega)$.

For example, cosine window function can be utilised. Even with noiseless signals, it is beneficial to filter. This removes the ripples at discontinuities of the backscattering functions, which originate from the fact that the transformed arrays in frequency domain are not completely symmetric. Figure 5.7 shows a simulated noiseless temperature profile with a hot-spot, when filtered and unfiltered simulated frequency responses are used.

Also the high-frequency noise is reduced significantly with the filtering. Figure 5.8 shows the temperature profile as a function of length in a section containing a hot-spot, with and without applying the cosine filter function. A $14km$ SMF system with $\Delta z = 3m$ is assumed, and data-points are sampled with $B_e = 96Hz$. It is found that by applying the cosine window function as the LP filter on both frequency response magnitudes $|S_R(\omega_m)|$, the standard deviation is, in this case, reduced by a factor of around 1.46 on average, without noticeable degrading of the resolution.

Spatial filtering of the calculated temperature curve, that is averaging over a couple of neighbouring points, effectively corresponds to LP
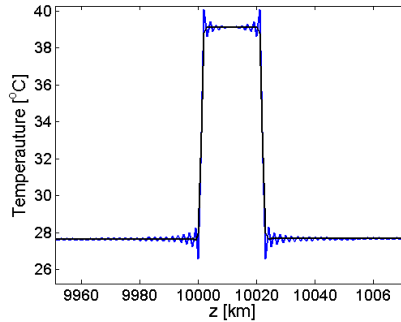
**Figure 5.7:** Simulated noiseless temperature profile with a hot-spot. Ripples at the edges of a hot-spot are removed when LP filter is applied to the frequency-response $S_R(\omega)$. No noise is added in either case.
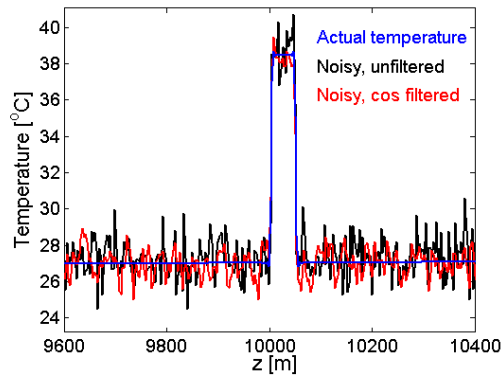


**Figure 5.8:** Temperature profile with a hot-spot obtained using simulated noisy signals unfiltered and filtered with cosine window function.

filtering in frequency domain, with exponential window function. Similar results are achieved with respect to the reduction of STD, but spatial averaging is usually a more time-consuming process than direct filtering, and it is more difficult to resolve possible sharp edges in the temperature profile.

### 5.3.2 Non-linear denoising

Nonlinear filtering can also be applied to reduce the noise level. Here, the results may be unpredictable, and the approach has an "ad hoc" nature. The possibility has been investigated only briefly with median filtering and Discrete Wavelet Denoising (DWDN).

#### Median filtering

Median filter eliminates large fluctuations from the average. The main drawback of the filtering is the reduced spatial resolution, especially if the number of points along the temperature profile, over which the median is taken, is large.

However, if the measured temperature is considered quasi-static in a certain time interval $\Delta\tau$, then $\Delta\tau$ is the time allowed for the measurement to take place. Theoretically, it makes no difference to take one measurement of duration $\Delta\tau$ (with small electrical bandwidth) or $\Upsilon$ measurements of duration $\Delta\tau/\Upsilon$, i.e. with $\Upsilon$ times larger bandwidth (if the time it takes to set the modulation frequency etc. is disregarded). The standard deviation depends on the total time of averaging.

It is investigated whether it is advantageous to take a number of measurements, as illustrated in figure 5.9, and apply nonlinear filtering, such as median filtering, on points corresponding to the same position.
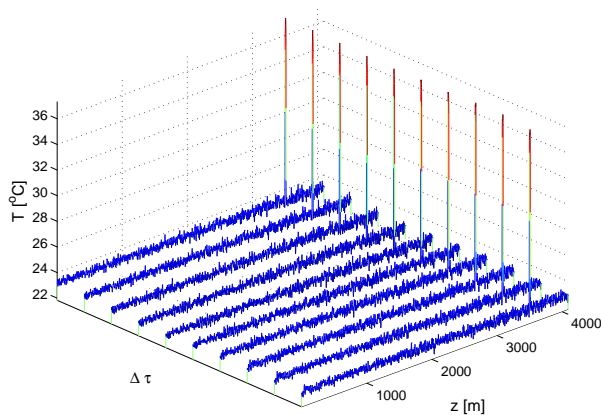


**Figure 5.9:** Simulation of several consecutive temperature measurements taken within time $\Delta\tau$.

It was found that this approach, statistically, does not reduce the standard deviation more than pure linear averaging.

### 5.3.3   Discrete Wavelet denoising

A noisy signal, here the temperature profile $T(z)$ or even the frequency responses $S_R(\omega)$, can be decomposed by means of discrete wavelet transformation into an infinite set of mutually orthogonal wavelets [41]. If the signal is reconstructed by inverse discrete wavelet transform from the wavelet spectrum, but taking only its highest coefficients, some noise contained in the original signal is removed [41].

It is important to choose an appropriate wavelet scaling function for decomposition. The choice depends on the expected signal - the wavelet scaling function should have similar properties (continuity and continuity in derivatives) to the expected signal [42]. In the following, only the Daubechies family [41] of wavelets is used. The simple wavelet Haar1 at level 1 is initially chosen, as its scaling function resembles a hot-spot. (Discrete wavelet denoising (DWDN) is performed in Matlab using 'wden' command with soft thresholding.)

After the wavelet denoising, the temperature profile is smoother and the ripples at discontinuities are also suppressed. Furthermore, the standard deviation of the temperature profile is reduced by approximately a factor of 1.2 using the same setup as in linear filtering. The effect is similar to what is obtained by applying a standard cosine window to the frequency spectrum. Actually, applying Haar1 wavelet also corresponds to a form of low-pass filtering [41].

STD is suppressed even further using more complex wavelets, but the approximation of the temperature profile with a one-point hot-spot, which is a typical feature in applications for the DTS, becomes poor. Denoising with DWT using e.g. Daubechies6 wavelet does yield some improvement, but the length of the hot-spot must be long (e.g. $10 \cdot \Delta z$), otherwise after each discontinuity, an artefact is induced - the hot-spot resembles the wavelet scaling function. An example of this is shown in figure 5.10.
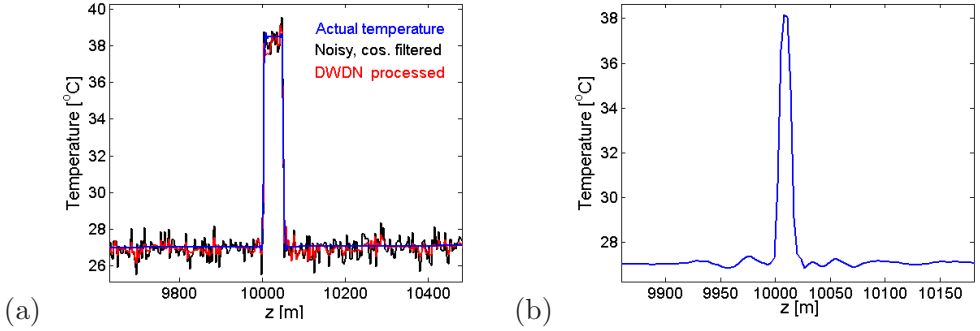
**Figure 5.10:** (a) Temperature profile obtained using simulated noisy signals filtered with cosine window function and discrete wavelet denoising routine with Haar1 wavelet, (b) Simulated temperature profile with a narrow hot-spot, obtained using signals filtered by discrete wavelet denoising routine with DB6 wavelet.

Figure 5.9 can also be regarded as a two-dimensional noisy picture, and it can be processed with standard DWDN procedures and tools for image manipulation and denoising, accommodated for this application. Again, statistically there is not any significant improvement compared to the averaging and LP filtering.

Discrete wavelet denoising does not give significant improvements when processing static or quasi-static signals. However, it may be efficient in detecting appearance of significant changes in the temperature profile regarded over a longer time period. This would allow averaging over a longer time, thus reducing the STD. However, this routine has not been implemented yet.

## 5.4 Summary

The physical processes of signal and noise generation, introduced in previous chapters, are described mathematically, and the developed model is implemented, calibrated and tested here.

The noise of each channel is treated as Gaussian white amplitude noise. This describes the real noise sufficiently well. The modelled frequency responses, backscattering functions and finally temperature profiles proved to be in good agreement with the measured data.

Digital signal processing can refine the collected data. Low-pass

filtering proved to be an efficient way for removing the high-frequency noise as well as oscillations near discontinuities, which are inherent in the IOFDR technique.

It was shown that the cosine window function applied on the frequency responses of both channels can reduce the standard temperature deviation by a factor of around 1.4. Spatial averaging is also a form of LP filtering where high-frequency noise is efficiently suppressed, but the resolution is degraded more than using the cosine window.

Discrete wavelet denoising is considered as well. However, for static signals with a discontinuity in form of a hot-spot, Haar1 wavelet must be used, which is again equivalent with using a LP filter. Other wavelets may reduce noise even more, but are not as suitable for the expected temperature profiles.

# Chapter 6

# Optimisation of the Optical System

The transimpedance amplifier circuit and its components, which are described and analysed in Chapter 4, have the highest influence on the accuracy of the sensor concerning the electronics. In this chapter, the focus is on the optimisation of the optical modules and signal characteristics.

In the following, it is strived to systematically improve all links constituting the system chain. The overall goal is to maximise the weak anti-Stokes signal by all possible means. More specifically, the wavelength of the pump laser is adjusted so as to avoid the high-loss region of the single-mode fibre, and yet bring about most signal power. The power of the pump laser is also maximised to the point where the stimulated Raman scattering becomes detrimental. Furthermore, characteristics, such as scattering cross-section and dispersion of the sensing fibre are studied. The influence of the width of the optical filters is investigated as well. Besides these parameters, the modulation format of the pump laser is also a subject of discussion in this chapter.

## 6.1   Optimisation of the pump wavelength

In this section it is intended to find the optimal pump wavelength $\lambda_{P,opt}$ for the DTS, but also the parameters on which $\lambda_{P,opt}$ depend. This is

done by maximizing the power of the signal originating from the data-point from which the signal is weakest, and at the same time minimising the noise at the receiver. Initial analysis, however, disregards the detector-specific effects, i.e., the noise is assumed to be the same irrespective of the received power and responsivity function of the detector. Further analysis shows the influence of inclusion of shot-noise (at the same time assuming it is the main noise source).

### 6.1.1   Detector-independent optimal pump wavelength

The ultimate sensitivity of the DTS is dictated by the weakest signal reaching the detectors i.e. the anti-Stokes signal originating from the far end of the sensing fiber. That is, integrating the signal power from fiber section $[L - \Delta z; L]$ and propagating it back to the detector, gives a value proportional to

$$P_{aS,d}(L, \lambda_P, \Delta z) \propto P_0 \chi_{aS} \cdot \int_{L-\Delta z}^{L} e^{-(\alpha_P(\lambda_P)+\alpha_{aS}(\lambda_P))z} dz \qquad (6.1)$$

Evaluating the integral, and using equation (2.10), one obtains

$$\widetilde{P}_{aS,d}(L, \lambda_P, \Delta z) \propto \frac{P_0 n_{aS}(\lambda_P)\eta(\lambda_{aS})e^{-(\alpha_P(\lambda_P)+\alpha_{aS}(\lambda_P))\cdot L}}{n_P(\lambda_P)\lambda_{aS}^4(\lambda_P)(\alpha_P(\lambda_P) + \alpha_{aS}(\lambda_P))} \cdot \left( e^{(\alpha_P(\lambda_P)+\alpha_{aS}(\lambda_P))\cdot \Delta z} - 1 \right)$$
$$(6.2)$$

It must be clarified here that e.g. $\alpha_{aS}(\lambda_P)$ is the attenuation at the anti-Stokes wavelength obtained from the corresponding $\lambda_P$ shifted down by $(\lambda_P^2/c)13THz$.

Before finding the optimal pump wavelength, all wavelength-dependent parameters in equation (6.2) are modelled. It is clear that all these parameters i.e. loss, capture fraction and effective index are different for various fibre types, but here standard SMF is considered.

The attenuation in the optical fiber in the wavelength interval $0.6\mu m$ to $1.8\mu m$ is well approximated by including four contributions [43], namely, Rayleigh scattering, ultraviolet absorption, infrared absorption and waveguide imperfections. Rayleigh scattering is described in Section 3.2.1, and scales with $\lambda^{-4}$. Ultraviolet absorption decreases with the wavelength and is caused by the electronic resonances. The infrared absorption increases with the wavelength, and is due to vibrational resonances of silica molecules. Finally, there is Mie scattering, which adds

a nearly constant bias to the attenuation because of waveguide imperfections.

In addition to these, there are usually several absorption OH peaks, of which the most significant one is at 1385nm. This, as well as other impurities in the silica fibre are disregarded. The attenuation can therefore be expressed as

$$\alpha(\lambda) = \frac{A_{Rayleigh}}{\lambda^4} + B_{UV} \cdot e^{\frac{b_{UV}}{\lambda}} + C_{IR} \cdot e^{-\frac{c_{IR}}{\lambda}} + D_{Mie} \qquad (6.3)$$

where $A_{Rayleigh}$, $B_{UV}$, $b_{UV}$, $C_{IR}$, $c_{IR}$ and $D_{Mie}$ are constants which scale the mentioned contributions.

The attenuation profile used in the calculations is shown in figure 6.1 together with its constituent parts. Disregarding the OH peaks may be partly justified by the fact that the SMF used for the DTS is dehydrated, and has very low OH content.
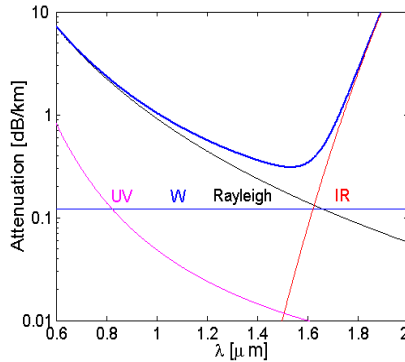


**Figure 6.1:** Approximated spectral loss profile of an SMF according to equation (6.3) with its four components: Rayleigh scattering, UV absorption, waveguide imperfections (W) and IR absorption.

The capture ratio, previously defined and depicted in section 2.5, is also of interest

$$\eta(\lambda) = \frac{3\lambda^2}{8\pi n^2(\lambda) A_{eff}(\lambda)} \qquad (6.4)$$

The very small fraction of the scattered light that is guided to the detectors, needs to be maximised.

Finally, the wavelength dependence of the refractive index is considered. The dependence of the refractive index on wavelength is calculated using Sellmeier's approximation [9] described in appendix C. The variation of the effective refractive index in the SMF is relatively small, and the influence of refractive indices on optimal wavelength is negligible - there is a variation in the ratio $n_{aS}/n_P$ of less than 1% over the entire interval $600 - 1800nm$.

As stated in section 2.3, Raman scattering has a $\lambda^{-4}$ dependence, i.e., it is most efficient at short wavelengths, and drops off as the pump wavelength is moved upward. Also, Rayleigh scattering, which is responsible for most of attenuation in the optical fibre in the visible, NIR and IR regions, has a $\lambda^{-4}$ dependence. That is, the greater the signal generation, the higher is the attenuation.

Therefore, it is necessary to find an optimum, for a given fiber length and spatial resolution (where resolution plays a less significant role), between favorable Raman scattering and deteriorating attenuation. Equation (6.2) is evaluated and maximised with respect to $\lambda_P$ for a sequence of lengths $L$ ranging from 1 to $20km$. Figure 6.2 shows the approximated optimal pump wavelength as function of sensor range.
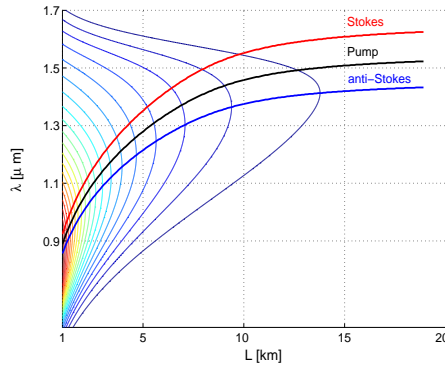


**Figure 6.2:** Approximated optimal pump wavelength and corresponding Stokes and anti-Stokes wavelenghts for the DTS based on SMF, as a function of the range. The contour plots show levels of anti-Stokes signal at the detector from the far fibre end $P_{aS,d}(\Delta z = 1m)$.

The practical choice of the pump wavelength depends also on the availability of high-power pump lasers, optical fiber and its actual loss

profile, detector response etc. It is therefore useful to calculate the penalty for choosing suboptimal pump wavelength. In figure 6.2 the inscribed contours show levels of anti-Stokes signal at the detector from the far fibre end $P_{aS,d}(\Delta z = 1m)$ (equation (6.2)) and may indicate the magnitude of this penalty. For using a pump wavelength which deviates from the calculated, the penalty is highest for short-range sensors (more contours are crossed), whereas for long-distance DTS, the optimal wavelength asymptotically approaches a value around 1550nm, and it is less critical which wavelength is used.

### 6.1.2 Optimal pump wavelength with shot-noise

The optimal pump wavelength in IOFDR depends on detectors too. The responsivity and noise characteristics of different APDs may vary, and different kinds of APDs (Si, various InGaAs alloys) are used for different wavelength regions.

It is first assumed that the responsivity function changes insignificantly in the regarded wavelength interval. It is here also assumed that the shot-noise is the dominant noise term, as it is shown in Section 4.6. High average signal power impeding the APD produces the dominant part of the shot-noise, but does not necessarily yield better SNR of the signal originating from the far fibre end. Therefore, higher pump wavelength is preferred when the noise is accounted for. The attenuation as well as the average signal power are lower here.

Signal power from the entire fibre is found (increasing the boundaries of the integral in equation (6.1) to $[0; L]$) making it possible to find the shot-noise (dark current is assumed negligible). Then, the SNR is determined and maximised for the point at the fibre end.

Figure 6.3 shows the approximated optimal pump wavelength together with the corresponding wavelengths of Stokes and anti-Stokes scattering, when shot-noise is taken into account. The dashed lines show the previous result from figure 6.2, i.e. without the shot-noise considerations.

Apparently, after inclusion of noise, $\lambda_{P,opt}$ approaches its asymptotic value faster.

Finally, the responsivity function of an InGaAs APD, shown in figure 4.1, is included in the model. Figure 4.1 shows that the pump wavelength
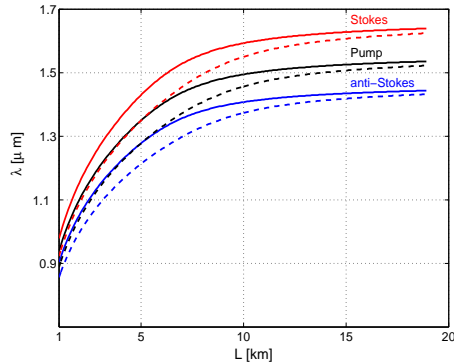
**Figure 6.3:** Approximated optimal pump, Stokes and anti-Stokes wavelength for the DTS based on SMF, when shot-noise is taken into consideration (solid line), and without the shot-noise (dashed).

approaches the asymptotic value even faster. The InGaAs APD is not applicable outside the shown wavelength interval.
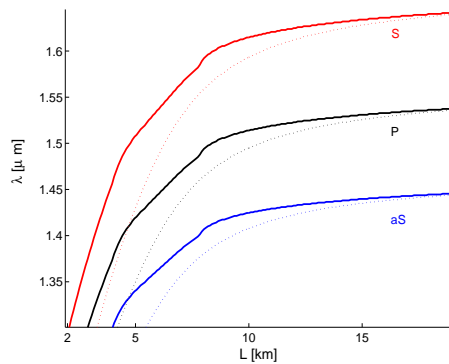


**Figure 6.4:** Approximated optimal pump, Stokes and anti-Stokes wavelength for the DTS based on SMF, when shot-noise and responsivity of InGaAs APD are taken into consideration (solid line), and with the shot-noise only (dashed).

Finally, note that if OH peaks were included in the loss-model, the curve for optimal pump would not be as monotonous. Generally, operation near these peaks is not recommended since the absorption here may change with time. Even if the fiber is dehydrated and has very small OH absorption, it can absorb water molecules from the surroundings.

For the DTS, it is important that loss parameters do not change (in one channel only), as this may be interpreted as a change in the temperature, if no re-calibration is made.

The desired range of the DTS based on the SMF is around $10 - 15km$. According to figure 6.4, a wavelength near $1500nm$ should be chosen. A high-power pump lasers with wavelengths of $1493nm$ and $1506nm$ are used in the experiments. With these sources, the maximum of anti-Stokes channel is in the range of $1400 - 1440nm$ and Stokes is in the range $1550 - 1610nm$.

## 6.2 Optimisation of fibre characteristics

The amount of received signal depends highly on the type of the sensing fibre. The important parameters here are the attenuation, numerical aperture (NA) or the capture fraction, and the Raman cross-section. In this work, various single-mode fibres are analysed, but also multi-mode fibres are looked at.

The numerical aperture, depends firstly on whether the fibre is multi-mode or single-mode. Due to many possible modes of propagation, multi-mode fibres have large numerical aperture compared to single-mode fibres and make them attractive in that respect.

For single-mode fibres, the refractive indices of the core and cladding together with the area of the core are decisive for the NA. According to equation (2.13), a small core diameter and high index contrast between the cladding and core increase the amount of the captured signal. However, small core diameters confine the light into a small area, rendering the intensity of the field high in the fibre centre, which enhances stimulated Raman scattering. Stimulated Raman scattering distorts the crucial amplitude information of the spontaneously scattered Raman light and may, therefore, be detrimental for the extraction of information on temperature. Hence, in single-mode fibres it is desirable to have high capture fraction, but at the same time limit the pump power to below the threshold for the stimulated Raman scattering process.

The Raman cross section is also material-specific. Appropriate doping may increase the Raman cross-section of silica fibre. E.g., $GeO_2$ imbedded in silica has maximum Raman gain coefficient at a frequency shift very close to that of pure silica. It is therefore advantageous to

use fibres with high $GeO_2$ concentration in Raman amplifiers, but here, where spontaneous Raman scattering is utilised and low attenuation is required, dopants do not have significant influence [19]. Additional effects of doping with $GeO_2$ are increased attenuation, and increased refractive index and hence the NA. [1]

Tests with several types of standard fibres, four single-mode and two multi-mode, with different cores dimensions and doping were performed. Namely, Raman cross-section and loss of standard single-mode fibre (SSMF), dispersion compensating fibre (DCF), inverse dispersion fibre (IDF) [44] and Raman fibre (RAF) [30] were measured. Also listed are characteristics of typical standard step-index multi-mode fibre (SIMMF) and the graded-index multi-mode fibre (GIMMF). It is the intention to find the relevant parameters for core design (as function of required sensor range), and find the best among the available ones.

### 6.2.1    Comparing the characteristics of the fibres

Table 6.1 summarises the main characteristics of the mentioned fibres. The way in which $\chi_R$ is measured (described in section 2.6) makes it highly dependent on the bandwidth of the optical filters in the setup. But the same filters are used for all fibres, which justifies the comparison between the tested fibre types. There is, however, the uncertainty in the coupling loss from some special fibres to the SMF based WDM.

It is possible to establish a function of merit for each fibre type. It is chosen here to evaluate the fibres according to how much scattered power from the fibre end reaches the AS photodiode as function of fibre length assuming the pump power is constant. A function of merit $F(z)$ is introduced to show how favourable the properties of a fibre are relative to the standard SMF, as function of distance. Standard SMF is taken as a reference because it is used in most of the experiments.

$$F(z) = \frac{\chi_F}{\chi_{SMF}} e^{-(\alpha_F - \alpha_{SMF})z} \qquad (6.5)$$

At $z > L_{limit}$, there is less signal from the regarded fibre than from the

---

[1]Alternatively, there is a theoretical possibility to use an undoped all-silica photonic crystal fibre (PCF), which has a high capture fraction, and at the same time low scattering loss.

| Fibre type | SMF | DCF | IDF | RAF | SIMMF | GIMMF |
|---|---|---|---|---|---|---|
| Loss aS $[dB/km]$ | 0.28 | 0.8-0.9 | 0.35 | 0.4 | **2** | **0.3** |
| Loss S $[dB/km]$ | 0.2 | 0.6 | 0.31 | 0.6 | **2** | **0.3** |
| Loss P $[dB/km]$ | 0.21 | 0.54 | 0.28 | 0.45 | **2** | **0.3** |
| $\chi_{aS}[km^{-1} \cdot 10^{-9}]$ | 140 | 900 | 360 | 405 | 2970 | 220 |
| $\chi_{S}[km^{-1} \cdot 10^{-9}]$ | 520 | 2200 | 841 | 880 | $\approx 5000$ | 870 |
| $g_R[(W \cdot km)^{-1}]$ | 0.36 | **2.38** | N/M | **2.50** | N/M | 0.17 |
| $A_{eff}$ $[\mu m^2]$ | **85** | **21** | **31** | **18** | $\approx 3000$ | N/M |
| Capture fraction [%] | 0.14 | 0.76 | 0.37 | 0.64 | N/M | N/M |
| Max. $P_P$ [mW] | > 150 | $\approx 55$ | > 80 | $\approx 40$ | > 500 | > 200 |
| Dispersion $[ps/km \cdot nm]$ | $\approx 17$ | $\approx -130$ | N/M | N/M | N/M | $\approx 18$ |
| Dopant [mol] | **3.5** | **17** | **9** | **14** | N/M | N/M |

**Table 6.1:** Relevant properties of single-mode fibre (SMF), dispersion-compensating fibre (DCF), inverse-dispersion fibre (IDF), Raman fibre (RAF), step-index multi-mode fibre (SIMMF) and graded-index multi-mode fibre (GIMMF). Bolded values are retrieved from data-sheets, while others are measured or calculated. Some values were not available nor measured (N/M).

SMF

$$L_{limit} = \frac{1}{\alpha_F - \alpha_{SMF}} \ln \frac{\chi_F}{\chi_{SMF}} \qquad (6.6)$$

Figure 6.5 shows the function of merit defined in equation (6.5) for the different fibres. No restriction regarding maximum pump power is taken into consideration here, and identical pump powers have been assumed for the different fibres. Point of intersection with the constant 1 shows up to which length it is advantageous to use the considered fibre in stead of the SMF.

It is interesting to note that the IDF performs better than SMF up to a length of approximately $20km$, provided the SRS is ignored. The small mode area, however, sets a low limit to the allowable pump power.

It is assumed that all fibres can tolerate the same initial pump power as the SMF without stimulated Raman scattering becoming significant. To include the limitation incurred by stimulated Raman scattering, one can limit the intensity by scaling with the mode area. The function of merit is revised as $F^*(z) = F(z)A_{eff,F}/A_{eff,SMF}$ for fibres with core-area smaller than in SMF. No scaling is done on the MMFs. Figure 6.6
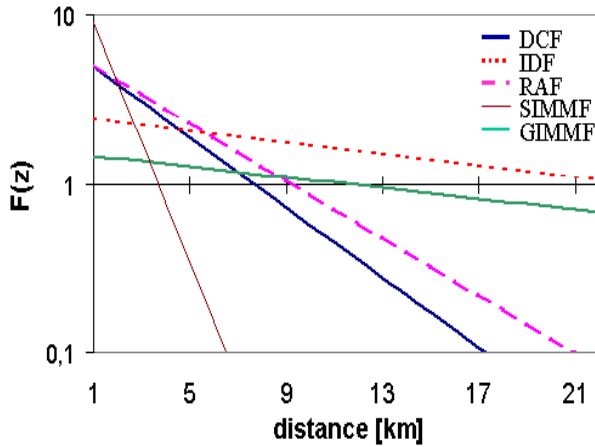
**Figure 6.5:** Function of merit for the different fibre types IDF, DCF, RAF and MMF for some input power, thus assuming SRS is not a limiting factor.

shows $F^*(z)$ for the five fibre types.
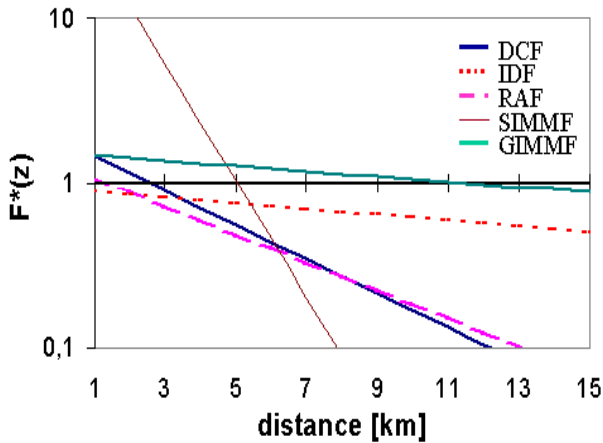


**Figure 6.6:** Function of merit as for the IDF, DCF, RAF, GIMMF and SIMMF when power is limited to avoid strong influence of the SRS.

The picture changes drastically since the SMF has by far the largest core area (except for the SIMMF and GIMMF for which the pump power has been limited to the commercially available average value of around

$500mW$). IDF performs, according to this comparison, marginally worse than the SMF for any range.

From the above, one can conclude that SIMMF is the most suitable fibre for short-range sensors, i.e., $L < 5km$. When the range of $5km$ needs to be exceeded, other fibre types must be employed. GIMMF, as a transition between the SIMMF and the SMF, is theoretically the best choice for range $5km < L < 12km$. The SMF and GIMMF are both good candidates for sensors with range $L \approx 10km$. The GIMMF has a slight advantage of being less affected by the SRS, whereas optical components with SMF pigtails are easier to find.

## 6.2.2 Two-fibre system

Analysis above also suggests the possibility to combine two fibres, e.g., standard SMF and DCF to obtain extended range of the sensor. In this way, the low loss standard SMF provides an adequate Raman signal for the first couple of kilometres, and when the pump power is below the threshold for stimulated Raman scattering, the more sensitive DCF can be applied.

In the following, it will be shown how it is possible to extend the sensor range by use of a combination of several different fibre types connected to form a linear sensor. Initially, the situation when two fibre types are combined is analysed. The sections of the sensor fibre are in the following called $fibre_1$ and $fibre_2$. The proposed setup is shown in figure 6.7.

The most favourable configuration is when $fibre_1$ has low $GeO_2$ doping, low attenuation, larger mode area and hence small influence of SRS. The backscattering coefficient of $fibre_1$ is relatively low, but it is outweighed by the high allowed pump power. $fibre_2$ is more heavily doped, has a smaller mode area but high backscattering coefficient and capture fraction. The intensity in the core of $fibre_2$ is limited since the pump power decayed in $fibre_1$.

In the following, the lengths of $fibre_1$ and $fibre_2$ are optimised. The analysis of the system is done in the CW regime. The forward-propagating pump and the backward propagating signals experience exponential decay in the fibre due to the attenuation. If the sensing fibre of total length $L$ has a junction between its sections $fibre_1$ and $fibre_2$
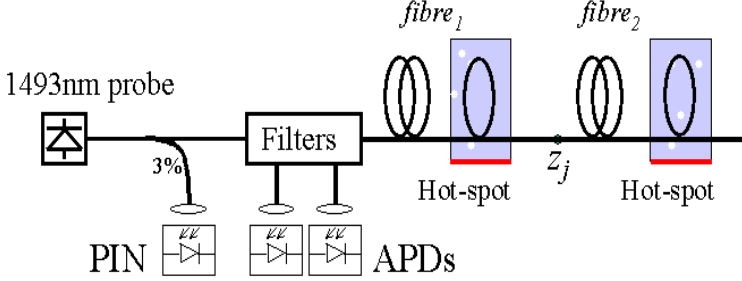
**Figure 6.7:** Setup of the system where the sensing fibre is comprised of $fibre_1$ and $fibre_2$.

at distance $z_J$, the infinitesimal power return from point $z$ in $fibre_1$ may be written as:

$$dP_1 = P_0 \chi_{R1}(z, T) \cdot e^{-\alpha_1 z} dz \qquad (6.7)$$

where $P_0$ is the initial power of pump laser, $\chi_{R1}$ is the fraction of captured, fibre-specific temperature dependent Raman backscattering coefficient (Stokes or anti-Stokes) that includes all doping contributions form $fibre_1$, $\alpha_1$ is the sum of the attenuation coefficients at the wavelengths of the pump and the Raman scattered light in $fibre_1$.

Similarly, the return power from section $dz$ of $fibre_2$ as function of distance is

$$dP_2 = P_0 \chi_{R2}(z, T) \cdot \psi_{12} \psi_{21} \cdot e^{(\alpha_2 - \alpha_1) z_J - \alpha_2 z} dz \qquad (6.8)$$

Here, $\psi_{nm}$ accounts for the splice and coupling loss between $fibre_n$ and $fibre_m$. $\chi_{R2}$ and $\alpha_2$ correspond to $\chi_{R1}$ and $\alpha_1$ in $fibre_2$.

Anti-Stokes channel is usually weaker, relatively more temperature dependent and thus decisive for the accuracy of the sensor. Therefore, the signal is optimised with respect to the AS channel. The optimal situation is when $dP_1(z_j)$ equals $dP_2(L)$, that is where the detected signals from fibre ends of $fibre_1$ and $fibre_2$ are equal in magnitude. If $dP_1(z_j)$ were higher than $dP_2(L)$, $fibre_2$ would be too long and worsen the temperature resolution. In the opposite case, $fibre_2$ could be longer and still not affect negatively the temperature resolution. (This is illustrated with a concrete example in section 6.2.3.) The junction $J$ is thus

placed at

$$e^{-\alpha_1 z_J} = \psi \cdot \frac{\chi_{2R,aS}}{\chi_{1R,aS}} e^{(\alpha_2 - \alpha_1) z_J - \alpha_2 L} \Leftrightarrow z_J = L - \frac{1}{\alpha_2} \ln \left( \psi \cdot \frac{\chi_{2R,aS}}{\chi_{1R,aS}} \right) \quad (6.9)$$

The second term in the right hand side of equation (6.9) gives the optimal length of $fibre_2$. This length is independent of the total sensor length or attenuation coefficients of $fibre_1$. It is not necessarily the case that for any fibre length one would benefit from combining the fibres. It is mentioned earlier that the optimal fibre type depends on the desired range. In order to benefit from combining two fibres, the total length must be larger than the length at which it is advantageous to use $fibre_2$ to $fibre_1$.

### 6.2.3  Experimental results with two-fibre system

To illustrate the concept, a setup comprising a composition of $11.2km$ standard single mode fibre and $4.8km$ dispersion compensating fibre is made.

Compared to SMF, Raman scattering in DCF is around six times as efficient due to the higher germanium doping and higher capture ratio. However, the attenuation is around three times as large at the anti-Stokes wavelength. The combination of fibres chosen for the experiment is therefore a length of SMF followed by a length of DCF. Typical properties of DCF and SMF, when inserted into equation (6.9), yield the optimal position of the junction $J$ being around $5.2km$ before the fibre termination, i.e., one can extend the sensor range by $5.2km$ of DCF.

The experimental setup is the same as shown in figure 6.7. In the actual experiment, a spool of $11.2km$ SMF and $4.8km$ DCF are connected to form the sensing fibre. The fibre is at room temperature of $22^oC$. In between the fibre spools, a section of $40m$ SMF as well as 15m section of the end of the DCF are submerged into hot water at $60^oC$. The hot-spots are introduced in order to allow calibration of the sensor. A grating-stabilized single mode laser-diode (LD) with centre wavelength $\lambda_c = 1493nm$ and average output power of $100mW$ is used as the pump source. The LD is directly modulated up to $8.2MHz$ resulting in a theoretical resolution of 6m (thus avoiding dispersion issues).

The $11.2km$ SMF and the splice to DCF attenuate the pump by

2.7dB. The pump power entering the DCF is thus around $54mW$, which is below the threshold for SRS (for the fibre length of $4.8km$).

Figure 6.8 shows the backscattering curves of the Stokes and anti-Stokes signals as a function of distance. The anti-Stokes channel is weaker, and at the same time more decisive for the temperature accuracy. The backscattering of anti-Stokes reaches approximately same level at the end of the SMF and DCF respectively. The temperature measurement is repeated 30 times, each measurement taking around half a minute. Figure 6.9 shows the standard deviation (STD) of the measured temperature as a function of distance. As predicted, the STD
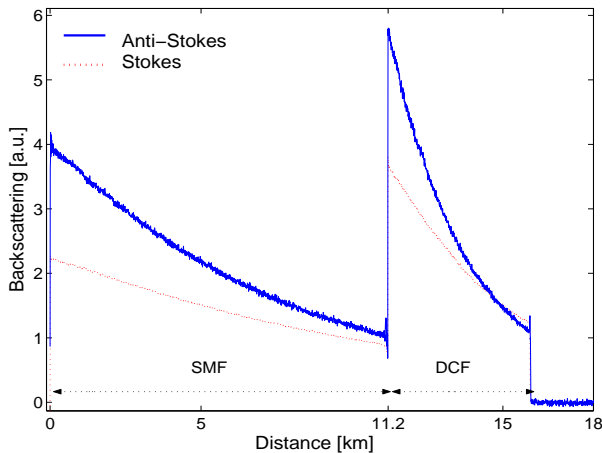


**Figure 6.8:**  Measured backscattering functions $s_R(z)$ of Stokes and anti-Stokes channels with clearly distinguished SMF and DCF sections of $11.2km$ and $4.8km$, respectively.

drops abruptly when the DCF is reached, and the combination of SMF and DCF effectively extends the range without compromising temperature accuracy. The STD is below $4^oC$ along the entire 16km range. For comparison, using the same acquisition time, the exponentially growing STD is estimated to have a maximum of $7^oC$ in a 16km long fibre sensor composed of only SMF.
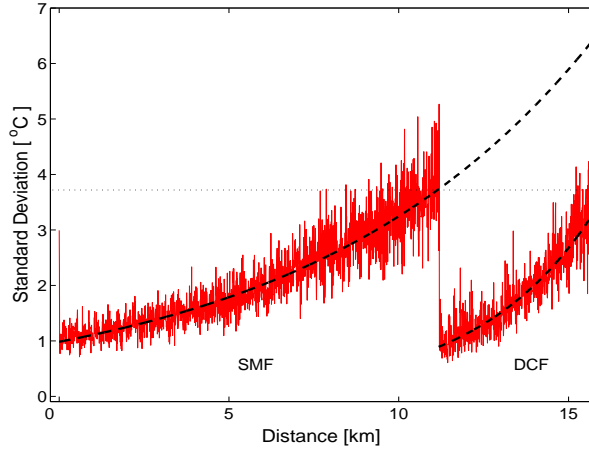
**Figure 6.9:** Standard deviation (STD) of temperature as function of distance. The dashed line shows an exponential fit of the standard deviation in the first and second section of the sensing fibre.

## 6.2.4 Influence of fibre dispersion

The difference in group indices i.e. propagation velocity in the fiber at the pump, Stokes and anti-Stokes wavelengths can also limit the resolution or range of the sensor. The optical fiber length is effectively different for the two signals. When this difference in fiber lengths $\Delta L$ becomes comparable to the spatial resolution $\Delta z$, the measurements are no longer accurate as specified. This needs to be taken into account when demodulation is performed, that is if $\Delta z < \Delta L$. With

$$\Delta L = N|\Delta z_S - \Delta z_{aS}| = \frac{Nc}{f_{max}}\left|\frac{1}{n_P + n_S} - \frac{1}{n_P + n_{aS}}\right| \qquad (6.10)$$

and assuming $(n_P + n_S)(n_P + n_{aS}) = 4n_g^2$ gives the condition

$$\Delta z < N\Delta z\left|\frac{\Delta z}{2n_g}\right| \Leftrightarrow N > \left|\frac{2n_g}{\Delta n}\right| \qquad (6.11)$$

where $N$ is the number of data-points and $\Delta n$ the difference in refractive indices at the Stokes and anti-Stokes wavelengths. If the resolution is set to $\Delta z = 1m$, $N$ corresponds to the length of the fiber in meters. As an example, a $\Delta n$ of $5 \times 10^{-4}$, which is according to the Sellmeier's

approximation of the group refractive index a typical value in single-mode fiber around $1500nm$, limits the length $L$ to approximately $3km$. This problem is solved by rescaling one of the two channels, so that the points of arrays containing the backscattering functions correspond to the same position in the fibre.
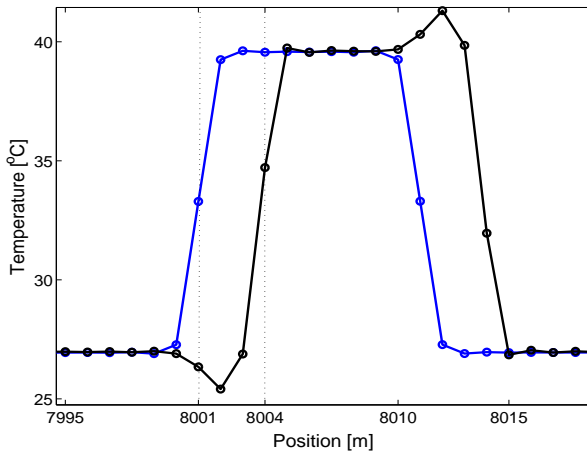


**Figure 6.10:** Computer simulation of a hot-spot in an fiber with zero $\Delta n$ and $\Delta n = 1 \times 10^{-3}$. Not only the hot-spot is displaced, but ripple at the edges is evident.

If MMF is used, there is an additional subtlety due to different propagation velocities and attenuation constants of different modes, in which case $\Delta n$ describes the maximum difference in the effective modal dispersion. In the case of single mode fiber, it is possible to correct for this error if the effective $\Delta n$ is known. However, a related problem can still arise if the signal band, i.e., the optical filter width is too wide so that intra-signal dispersion distorts measurements.

The width of the optical filters $\Delta\lambda_f$ defining the Raman channels has to be relatively large in order to collect as much signal as possible. But the different wavelength components within the channel travel with different velocities, and interfere with each other, effectively lowering the amplitude of the signal, relative to the case with no dispersion. The power at the APD detector, originating from the far fibre end, in the

window of wavelengths $\Delta\lambda_f = \lambda_2 - \lambda_1$ is

$$P_d(\omega, t, L) = P_0 \cdot \chi_R \cdot m \cdot \frac{1}{\Delta\lambda_f} \cdot e^{-\alpha L} \cdot \int_{\lambda_1}^{\lambda_2} \cos(\omega t - \omega\beta(\lambda)L)d\lambda \quad (6.12)$$

Apparently, the influence of dispersion depends on its magnitude, the sensor range, resolution and filter bandwidth. Here, dispersion is manifested in the term $\beta(\lambda)$. In equation (6.12) it is assumed that the contribution from each wavelength is same. Otherwise, the analysis would depend on the actual temperature of the fibre.

As an example, backscattering from the end of an $8.2km$ standard SMF is simulated as function of modulation frequency. Figure 6.11 shows how the relative amplitude of the Raman signal falls off with modulation frequency for several filter widths indicated in the figure. Reducing the filter width reduces the power of received signal too, but
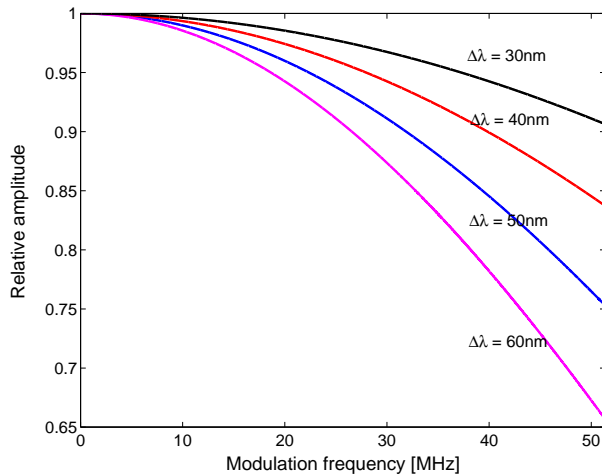


**Figure 6.11:** Backscattering from the end of an $8.2km$ SMF is simulated as a function of modulation frequency for several values of $\Delta\lambda_f$. Intra-signal dispersion lowers the amplitude of the backscattered light relative to the case with no dispersion, as the width of the optical filter increases.

limits the intra-signal dispersion. According to the figure, e.g., halving the filter width gives more than half the signal. Consequently, the filters at this range should be as wide as possible to maximise the AC part of the total signal. This is still under the assumption that Raman scattering is uniform in the considered region $\Delta\lambda_f$.

The influence of dispersion depends on the range $L$ as indicated by equation (6.12). The reduction of amplitude of the signal, relative to the case with zero dispersion, originating from different positions in the fibre, due to dispersion is depicted in figure 6.12. Measurements with
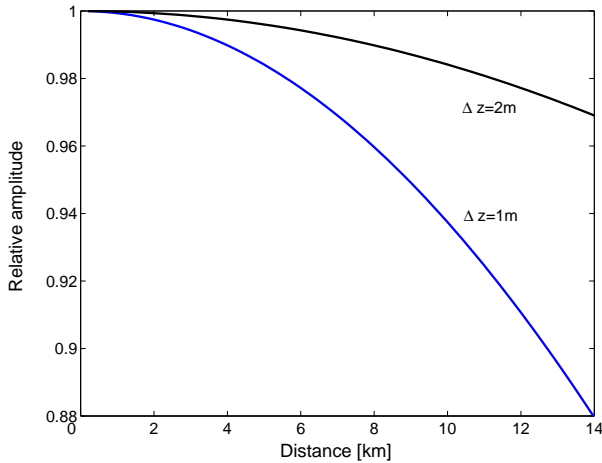


**Figure 6.12:** The relative amplitude (compared to zero dispersion case) of the backscattered light in SMF as a function of distance from the detectors for two spatial resolutions. Filter bandwidth $\Delta\lambda_f = 40nm$.

lower resolution are much less affected, and filters can by wide. To avoid signal degradation in long-range, high-resolution systems, narrow filters and long integration time may have to be utilised.

Dispersion of the GIMMF is investigated in the region around $1500nm$. A short pulse ($\tau_p = 1ps$) is sent through $7.7km$ GIMMF at several wavelengths (spaced by $\Delta\lambda_D$), where the relative delay $\delta_n$ is measured for each wavelength. More detailed description and results of the experiment are given in Appendix E. The dispersion $D$ is found determined as

$$D_\lambda = \frac{\delta_{\lambda_1} - \delta_{\lambda_2}}{L\Delta\lambda_D} \tag{6.13}$$

The dispersion of a 25km long SMF is measured as well to verify the method. Results for both fibres are shown in figure 6.13. Dispersion of the SMF is found to be around $17 - 18ps/(kmnm)$ at $1550nm$, which agrees well with the data-sheet value, and confirms the validity of the method. (However, the slope of the dispersion is not as expected). The
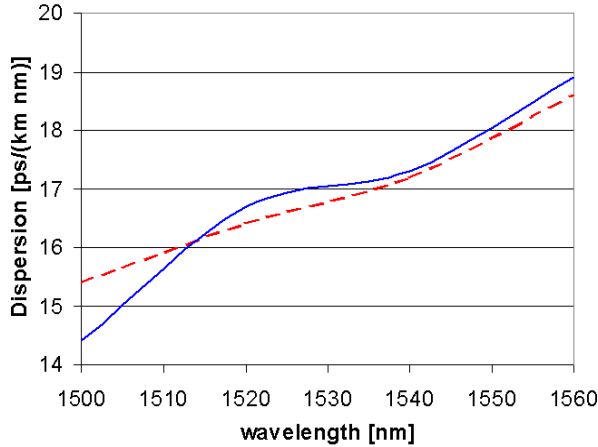
**Figure 6.13:** Measured dispersion of a $25km$ SMF (dashed) and a $7.7km$ GIMMF (solid).

unusual changes in the slope of the dispersion curve of GIMMF may be due to a combination of the modal dispersion and higher uncertainty caused by shorter fibre length, though. GIMMF has very similar dispersion characteristics to the SMF in the regarded wavelength interval, which makes it still an attractive candidate for use in the long-range DTS.

## 6.3 Optimum Pump Power

In IOFDR the entire fiber is continuously illuminated with relatively high intensity. In long-range DTS system based on SMF, the intensity dependent stimulated Raman scattering emphasized due to the small core area of the fibre and the long interaction length between the pump and the Raman signals. In this section, the impact of the nonlinear process of Stimulated Raman Scattering (SRS) on the Raman signals, and how this may be compensated is analyzed.

It is possible to suppress SRS by reducing the optical power or by using a sensing fiber with large effective area and low dopant concentration. However, as the spontaneous Raman scattering, on which the measurement is based, is also governed by these parameters, optimisa-

tion for low SRS will reduce the overall system performance. In Section 4.7, it is shown that the standard deviation of temperature measured by IOFDR is inversely proportional to the square root of the pump power, which makes it an important parameter in the system design.

SRS is manifested by stimulated transfer of the pump photons to the Stokes band (stimulated Raman gain), and more importantly in this case, photons from the anti-Stokes band are transferred to the pump (stimulated Raman attenuation).

The normally applied threshold for SRS is defined as the input pump intensity $I_{th}$ at which the generated Raman signal $I_S$ is equal in intensity to the remaining pump $I_{P,out}$ at the output of the fiber $I_S = I_{P,out}$, [10], but in principle the SRS is present in all relevant systems.

The interactions are governed by the following set of coupled differential equations

$$\frac{dP_S}{dz} = -g_R P_P P_S - P_P \chi_S + \alpha_S P_S \qquad (6.14)$$

$$\frac{dP_{aS}}{dz} = \frac{\omega_{aS}}{\omega_P} g_R P_P P_{aS} - P_P \chi_{aS} + \alpha_{aS} P_{aS} \qquad (6.15)$$

$$\frac{dP_P}{dz} = g_R P_P P_{aS} - \frac{\omega_P}{\omega_{aS}} g_R P_P P_S - \alpha_P P_P \qquad (6.16)$$

In this model, the equations are similar to a backward pumped Raman amplifier, as only the signals propagating in the opposite direction of the pump are considered. $g_R$ is the Raman gain efficiency with depolarized pump. Other variables and constants are as defined in Chapter 2. Pump depletion and growth due to the SRS may be assumed negligible, as the power of the Stokes and anti-Stokes signals typically is very weak ($<< 1mW$). Consequently, one may neglect the first two terms on the right-hand side (rhs) of equation (6.16).

The first terms on the rhs of (6.14) and (6.15) account for the influence of the SRS on the back-scattered Raman signals. As it will be shown, this results in a perturbation of the derived temperature measurement. It is, however, possible to predict and compensate for this effect, thus eliminating the distortion of the temperature curve. The compensation allows the use of higher pump power, which in turn generates more spontaneously Raman-scattered signals, according to the second terms on the rhs of equations (6.14) and (6.15). However, due to

the exponential attenuation of the anti-Stokes channel by the stimulated Raman process and only linear growth of the spontaneous anti-Stokes, increasing the pump power will not improve the SNR indefinitely. At a certain level, the number of anti-Stokes photons lost due to the SRS will exceed the number of spontaneous anti-Stokes photons generated by the increase in pump power, thus effectively reducing the AS signal level originating from distant fiber end.

Once more, the optimisation depends on the sensing fibre and sensor range. In the following, the optimum pump power level is found as a function of fiber parameters and fiber length.

### 6.3.1 Maximising the pump power

To find the optimal pump power for a certain setup, the anti-Stokes channel is considered. The stimulated Raman process has the most pronounced effect for continuous wave (CW), i.e., when the source is not modulated so that the entire fibre is illuminated. The coupled equations (6.14) and (6.15), in the CW regime yield the detector signal originating from an arbitrary point $z'$, when simplified to include only fiber loss and SRS

$$P_{aS,z'}(0) = P_0\chi_{aS}(T,z)\Delta z e^{-(\alpha_P+\alpha_{aS})z'} \cdot e^{\frac{g_R P_0}{\alpha_P}(exp(-\alpha_P z')-1)} \quad (6.17)$$

where $P_0$ is the average launched pump power (in this case CW) and $\Delta z$ is the spatial resolution. The signal uncertainty is highest at the far end of the fiber so that the analytical expression for the optimal pump power is found by maximising $P_{as,L}$ when $z' = L$ in equation (6.17).

$$P_{0,opt} = \frac{\alpha_P}{g_R \cdot (1 - e^{-\alpha_P L})} = \frac{1}{g_R L_{eff}} \quad (6.18)$$

where $L_{eff}$ is the effective length of the fiber [10]. Hence, the optimum pump power is a function of fiber length, Raman gain coefficient and the attenuation at the pump wavelength. The optimal pump power decreases rapidly with increasing fiber length. The received signal power *from the fiber end* as function of the pump power is depicted in figure 6.14 for several fibre lengths. The optimal pump powers are indicated in the graph. The parameters which are measured for the standard SMF are used in the modelling. Namely, $g_R = 0.36 \times 10^{-3}(Wm)^{-1}$
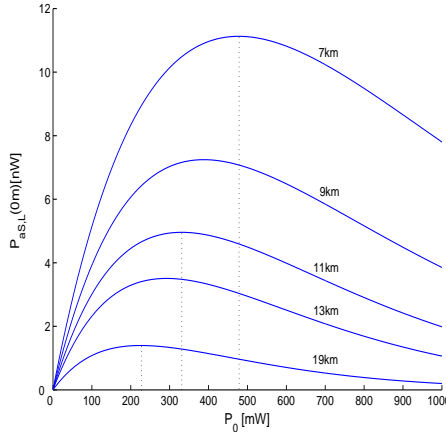
**Figure 6.14:** Received AS signal from remote fiber end as function of pump power for several fibre lengths. Parameters for standard SMF are used.

and $\alpha_P = 0.21 dB/km$. Initially, the signal grows nearly linearly with pump power, but it starts decaying exponentially after a certain power is reached. Apparently, SRS sets a lower limit to the pump power in long-range Raman based distributed temperature sensors.

The optimum pump power $P_{0,opt}$ for $25km$ standard SMF amounts to around $190mW$. However, this value is obtained using the maximum value of the Raman gain efficiency function $g_R(\omega)$, which takes place at a frequency shift of 13.2THz from the pump wavelength. Spontaneous emitted Raman signals cover a much wider bandwidth. If the optical bandpass filter defining the AS channel excludes this part of the spectrum, the effective $g_R$ is lower and yields a higher optimal pump power. In this work, however, this possibility is not used.

### 6.3.2   Compensation Function

Unlike anti-Stokes, the Stokes signal benefits from the strong pump due to the effective amplification by SRS. The SNR of the amplified signal improves with increasing pump power, and the backscattering curve needs only to be compensated for the SRS gain.

In typical IOFDR systems, the pump is modulated by a sinusoidal, thus allowing the frequency response of the system to be measured at

discrete frequencies. When modulation is applied to the pump, the influence of SRS is smaller (fibre illuminated by smaller average power) and higher average pump power is,in principle, allowed. The SNR of both S and AS signals falls off with increasing modulation frequency, so the optimal pump power may be somewhat higher than stated in equation (6.18). However, in this work, the optimum pump power to which is referred, is the one defined in equation (6.18).

The time ($t$) and modulation frequency ($\omega_m$) dependent pump, still assuming the pump is not depleted, may be written as

$$P_P(\omega, z, t) = P_0(1 + m \cos(\omega_m t - \omega_m \beta_P z))e^{-\alpha_P z} \tag{6.19}$$

where $m$ is the modulation depth, and $P_0$ the average power.

The Stokes photons experience a gain that is dependent on the modulation frequency. The signal at the detector is found by solving equation (6.14) using equation (6.19), with boundary condition $P_S(L) = P_P \chi_S e^{-\alpha L} \Delta z$.

$$
\begin{aligned}
P_{S,d}(\omega, t) \quad = \quad & P_0 \chi_S e^{P_0 g_R \left( \frac{1}{\alpha_P} + \frac{m(\alpha_P \cos(\omega t) + \omega \beta \sin(\omega t))}{\alpha_P^2 + \omega^2 \beta^2} \right)} \cdot \\
& \int_0^L \quad (1 + \cos(\omega t - \omega \beta z))e^{-(\alpha_P + \alpha_S)z} \cdot \\
& e^{-P_0 g_R \exp(-\alpha_P z) \left( \frac{1}{\alpha_P} + \frac{m(\alpha_P \cos(\omega t - \omega \beta z) + \omega \beta \sin(\omega t - \omega \beta z))}{\alpha_P^2 + \omega^2 \beta^2} \right)} dz
\end{aligned}
\tag{6.20}
$$

where the third term in the integral is due to SRS. To estimate the distortion caused by SRS, the integral is calculated with the actual $g_R$ and with $g_R = 0$. The ratio between the amplitudes of the AC part of the two resulting functions of modulation frequency gives the frequency compensation function. To find the compensation function for the anti-Stokes channel, the procedure is repeated with parameters valid for the anti-Stokes channel.

The simulation shows that SRS does not alter the phase of the recieved Stokes and anti-Stokes signals. The ratio between the amplitudes of these functions, thus gives the frequency compensation function. The compensation functions for the Stokes and anti-Stokes channels are shown in figure 6.15.
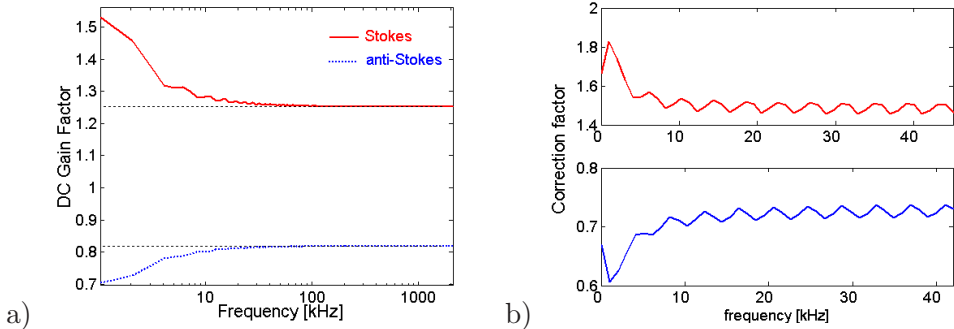
**Figure 6.15:** (a) The gain factor of the DC part of the backscattered Raman signals as a function of modulation frequency. The simulated fiber is $25km$ standard SMF, with $g_R = 0.36 \cdot 10^{-3}(Wm)^{-1}$. Average pump power is $100mW$. (b) Magnitude of the compensation functions for the Stokes and anti-Stokes channels as a function of modulation frequency. Frequency goes only up to $40kHz$ - the functions become periodic.

The Stokes signal is amplified up to 1.7 times, while the anti-Stokes signal is attenuated up to 1.43 times in the example where $25km$ SMF is used and average pump power $100mW$. The compensation functions for the Stokes and anti-Stokes channels become nearly periodic for modulation frequency above $40kHz$. The integral of the squared compensation functions is not unity since some of the energy has to be added to, or subtracted from Stokes and anti-Stokes signals, respectively.

The DC part of the backscattering influences only the shot-noise - it is slightly reduced in the anti-Stokes, and increased in the Stokes channel.

### 6.3.3   Experimental verification of the results

In this section, the results are applied on measured frequency responses, and it is shown how the temperature profile is corrected. Figure 6.16 shows an example of a temperature curve obtained using IOFDR on $25km$ SMF which is held at a constant room temperature. The average pump power here is nearly $100mW$.

The numerical prediction that predicts the impact of SRS is also shown. The obvious bending of the temperature curve is a consequence of SRS. The bending becomes increasingly pronounced as the pump power is set higher, or disappears when it is decreased (but the mea-

surement accuracy decreases as well). As illustrated, it is possible to compensate for this effect and rectify the temperature curve by applying the calculated correction factors.
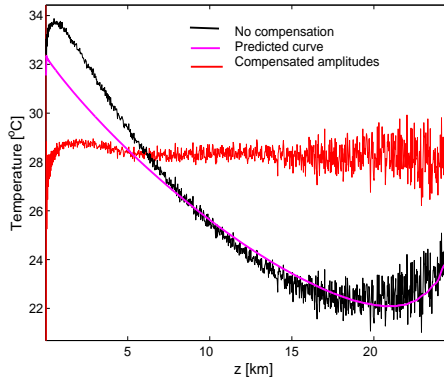


**Figure 6.16:** The measured, predicted and compensated temperature profiles of 24km SMF DTS with resolution of 6m. A very good agreement between the theory and measurements is achieved.

There is a very good agreement between the predicted and measured results. The peak-to-peak error due to the SRS for this particular setup without compensation is around $12^{o}C$. The systematic smooth variation over the long distance indicates that most of this error originates from deviations at low modulation frequencies ($f_m < 25kHz$), which is in agreement with figure 6.15. The nearly constant attenuation and amplification for $f > 25kHz$ modifies only the effective fiber loss, which is automatically cancelled by calibration.

The compensation is especially necessary for long-range systems where the interaction length of the pump and signals is most significant and where SMF having small core area is used. Short-range systems ($< 5km$) employing SIMMFs are virtually unaffected by SRS for all practical purposes.

As stated in Chapter 2, SRS is not dependent on temperature. Therefore, for a chosen fiber length and pump power, it is possible to calculate the compensation functions once, and they remain constant for a certain setup. Furthermore, the numerical compensation can be incorporated in window- or low-pass filter-function and will hence not have any impact on the total computation time.

## 6.4    Optimisation of the modulation format

The following section describes some estimations of possible improvements of the system performance by modification of the transmitter signals. The improvements are assumed valid both for single-mode and multi-mode fibres.

### 6.4.1    Modulation format

The shot-noise in the long-range DTS system (where InGaAs APDs are used) is the dominant source of noise - it is several times higher than other noise contributions, specifically the thermal noise. The system is thus said to be shot-noise limited. The shot-noise power of an APD receiving the optical power $P_{avg}$ is given in equation (4.3).

In the shot noise term, only the detector dark current $I_d$, is affected by the detector temperature, and typically, $I_d$ is several orders of magnitude lower than the detector current, $R \cdot P_{avg}$. Hence, reducing the temperature of the InGaAs APD (from room temperature) does not have a dramatic impact on the total noise of the system. However, the overall SNR improves almost linearly with a reduction of the average signal power. The resulting STD (standard deviation) of temperature drops approximately with the square root of the change in average signal power, assuming the amplitude of the signal is unchanged.

Reduction of the average power emitted by the laser may be done through alternative modulation formats. The laser is not modulated to produce a pure sine wave, but maintains the fundamental frequency component at the nominal modulation frequency. The sine modulation $A_S$ of the pump laser (utilised now) may be expressed as

$$A_S = \frac{1}{2} + \frac{1}{2}\sin(f) \tag{6.21}$$

If the laser is modulated as half sine wave, $A_H$ may be expressed as

$$A_H = \frac{1}{\pi} + \frac{1}{2}\sin(f) - \frac{2}{\pi}\left(\frac{\cos(2f)}{3} + \frac{\cos(4f)}{15} + \frac{\cos(6f)}{35} + \cdots\right) \tag{6.22}$$

The main frequency component remains high (unchanged compared to the original modulation), but the average power, and thereby the noise,

is reduced by a factor of $\pi/2 \approx 1.57$. Hence, the overall STD of temperature is expected to be reduced by a factor of around $\sqrt{\pi/2} \approx 1.253$ by just changing the modulation format.
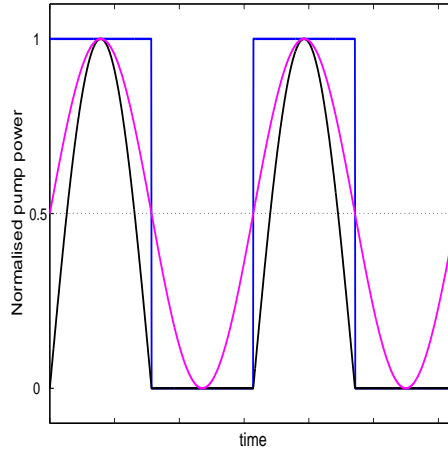


**Figure 6.17:** Proposed modulation formats of the pump laser. Either the average power should be low, or the amplitude of the fundamental frequency component high.

Alternatively, using square modulation (initially with 50% duty cycle) makes the average optical power launched into the fibre the same as in sine-modulated wave, but the amplitude of the main frequency component is higher by a factor of $4/\pi \approx 1.27$. The received signal will be increased accordingly, leading to a better overall SNR. This should directly reduce the STD of the temperature curve by 1.27 times, i.e. marginally more than if using the half sine modulation. Contrary to the half sine modulation, the amplitude of the first harmonic frequency is almost negligible. Square wave modulation is written as

$$A_Q \propto \frac{1}{2} + \frac{2}{\pi} \left( \frac{\sin(x)}{1} + \frac{\sin(3x)}{3} + \frac{\sin(5x)}{5} + \cdots \right) \qquad (6.23)$$

A combination of reduction of the mean optical power and increase of the amplitude of the main frequency component gives even better results. Square wave modulation with variable duty cycle ($d = \rho/\pi$)

may be expressed as

$$A_{Qd} = \frac{\rho}{\pi} - \frac{2}{\pi} \left( \frac{\sin(\rho)\cos(f)}{1} - \frac{\sin(2\rho)\cos(2f)}{2} + \frac{\sin(3\rho)\cos(3f)}{3} + \cdots \right)$$
$$(6.24)$$

It is now trivial to maximise the amplitude and at the same time minimise the square root of the average power i.e. find $\rho$ in

$$max\left( \frac{2\sin(\alpha)}{\pi} \middle/ \sqrt{\frac{\alpha}{\pi}} \right) \qquad (6.25)$$

or at points where $2\rho = \tan(\rho)$.

Figure 6.18 shows normalised equation $\sin(\rho)/\sqrt{\rho}$. Apparently, a 50% duty cycle ($\rho = \pi/2$) is not the optimal solution (due to the shot-noise) - it turns out that a duty cycle of 37% ($\rho = 1.166$) yields the most advantageous combination.
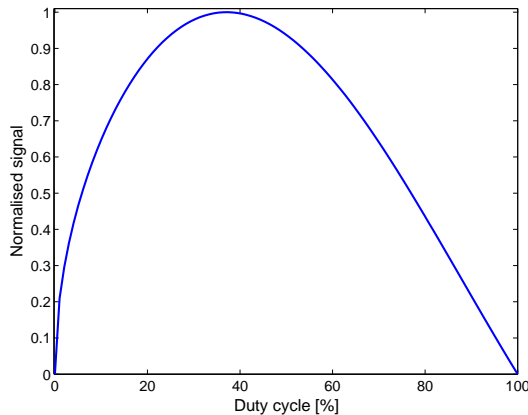


**Figure 6.18:** Theoretically, a duty cycle of 37% gives the best SNR. $2\rho = \tan(\rho)$ as a function of duty cycle $d = \rho/\pi$ is shown.

Using the square modulation with 37% duty cycle reduces the theoretical STD of the temperature curve by a factor of 1.35.

A study of half-sine wave with variable duty cycle shows the optimal duty cycle is 50%. That is, the square wave shown above is still the best and most practical solution. Note that linearity in current vs. optical output power is not necessary in square-wave modulation.

### 6.4.2 Probable problems

Probably the main problem with the alternative modulation formats is the fact that they produce higher order harmonics. A relatively narrow electrical filter may be needed to eliminate the harmonics and isolate the fundamental frequency component.

The received signal is mixed with a local oscillator so that the fundamental frequency is downshifted to $10kHz$ $(= f_{ds})$. This may give interference problems at low modulation frequencies. The lowest modulation frequency is determined by the sensor length (range). If it is set to $10km$ in the new system, the frequency spacing of the IOFDR system $\Delta f$ is around $5kHz$ according to equation (3.12).

Mixing the detected signal with the local oscillator gives

$$
\begin{aligned}
A_{LO} &\quad \cos(\omega_{LO}t + \phi) \cdot \sum a_n \cos(\omega_n t + \psi) \\
= &\quad \tfrac{A_{LO}}{2} \sum a_n \big( \cos((\omega_{LO} + \omega_n)t + \phi + \psi) + \cos((\omega_{LO} - \omega_n)t + \phi - \psi) \big)
\end{aligned}
\tag{6.26}
$$

There is a cross-talk between frequency-responses of the fundamental frequency and the fourth harmonic at low modulation frequencies (up to $f_m = 20kHz$ i.e. the first couple of data-points) in the worse case when the intermediate frequency ($f_{IF} = 10kHz$) is a multiple of $\Delta f$. If the $f_{IF}$ were not a multiple of $\Delta f$ (as is the case in a realistic situation), with narrow filtering around 10kHz (BW=1kHz), the problem of interference would be largely suppressed.

In practice, it may be preferable to change the $f_{IF}$ to a frequency that does not coincide with a multiple of the modulation frequency (e.g. $10.5kHz$) to be as far as possible from $n \times \Delta f$.

The existence of harmonics in the alternative modulation format does impose some limitations and complications to the system, but these are to be weighted with the advantages that follow.

### 6.4.3 Measuring several frequency components simultaneously

What seems to be a problem may result in being an additional advantage. The non-negligible component at double (or triple) the modulation frequency could be used beneficially. In other words, one could measure

the response of the fibre simultaneously at several frequencies, separated by band-pass filters before the mixer. Some authors acquainted with the IOFDR technique suggested this in a slightly different way [1], emphasizing it as an advantage of IOFDR. However, the idea is never implemented.

The amplitude of the first harmonic in half-sine wave is $3\pi/4 \approx 2.356$ times smaller than the amplitude of the main component. If the measurement is taken and later combined (weighted average) with an actual measurement at $2f_m$, the integration time is effectively improved for half of the measurements. Theoretically, this way the STD is improved by a factor of around 1.20.

For 50% duty cycle square modulation, every third frequency is measured twice (first time again with amplitude $3\pi/4 = 2.356$ times smaller than nominal value). The expected improvement in STD is only 1.1 times.

With 37.5% duty cycle, there is a component at twice the modulation frequency, but its amplitude is smaller. The improvement is again found to be around 1.1 times.

The use of harmonics demands redesign of the receiver and software, and gives only a modest improvement.

### 6.4.4   Experimental tests

The predicted improvements are tested experimentally. A description of the experiments and the results are presented in Appendix F.

Conclusively, there is a theoretical possibility to improve the system performance with 35% by changing the modulation format. In this estimate, possible negative effects from the practical realisation are disregarded. However, the generation of higher frequency components, which have to be effectively filtered out, do have a significant effect. The requirements for filtering must be evaluated experimentally.

## 6.5   Summary

In this chapter optimisation of several design parameters of the optical module is described. It is shown that the optimal design of the DTS system depends strongly on the posed requirements.

For short range sensors, it is important to generate strong signal in spite of high attenuation in the fibre, whereas high attenuation is unacceptable for long-range systems, even though a weak signal is produced. According to the analysis, a pump wavelength of around $1500nm$ is chosen for a DTS with range of $10 - 15km$. Note that using a pump laser with central wavelength of $1500nm$, one avoids the OH absorption peak at $1385nm$.

Choice of the optimal fibre is also discussed. Standard SMF and the GIMMF are the most suitable fibres (among the tested ones) for the long range DTS. GIMMF is in many ways similar to the SMF. But the ease of handling, its relatively large core area and high scattering cross-section make it a more attractive choice for the $10km$ DTS. It was found that up to a length of approximately $12km$, the GIMMF is preferred, while the SMF is recommended for $L > 15km$. For $13km < L < 15km$, the difference between the two is marginal.

Dispersion is an undesirable effect in distributed temperature sensing, and it can distort the Raman signals, or even limit the range or resolution of the sensor. However, in practical measurements, which are presented in Chapter 7, it does not produce visible deviations due to correct calibration of the sensor.

Step-index multi-mode fibre has additionally intra-modal dispersion. With its high dispersion and loss, it is not a good candidate for the sensor fibre in long-range distributed sensor systems. However, the SIMMF performs superbly in short-range systems due to its high numerical aperture and large core area.

DCF and RAF and are also unsuitable for long-range sensors because of a combination of high attenuation, dispersion and small mode area. Though, these fibres can be used to extend the range of a standard SMF based sensor. There is only a marginal difference in performance of the IDF and the SMF, but e.g. compatibility with standard WDM components make it inconvenient to use the IDF.

For an all-SMF $16km$ sensor, the exponentially growing standard deviation is estimated to $7^oC$ with acquisition time of less than half a minute. Combining $11.2km$ SMF and $4.8km$ DCF and using same acquisition time and resolution, one achieves standard temperature deviation as low as $4^oC$. Also the average standard deviation reduces significantly. Hence, a combination of SMF and DCF can enhance the

detected signal, which facilitates the extended range without diminishing temperature resolution. When combining two fibres with specific characteristics, there is an optimal length for the second fibre section, regardless of the total sensor range. For the particular fibre configuration used in the presented experiment, the optimal length of DCF was approximately $5.2km$. Optimising the fibre design specifically for the purpose of the sensor would probably increase the performance further. It is possible to expand the model to include more than two different fibre sections, and ideally, the core diameter and doping concentration should change continuously along its length. This would make the STD constant. The level of desired STD would then define the initial fibre index profile. The core diameter would decrease continuously with increase in refractive index of the core until physically achievable.

SRS poses a problem for distributed temperature measurements by spontaneous Raman scattering when IOFDR is used for obtaining spatially resolved measurements. It is found that the optimal pump power is reached when the anti-Stokes signal from the far fiber end is maximized, thereby bringing the sensor accuracy to the maximum. The optimal pump power is a function of fiber length and intrinsic fiber characteristics such as fiber loss, effective mode area and Raman gain coefficient. For a $25km$ long SMF the optimum average pump power, $P_{opt}$ is estimated to be nearly $200mW$.

Furthermore, a technique for numerical compensation of the SRS effect is developed and successfully tested. The compensation functions for the frequency data are found and applied on measurement results experimentally obtained from a $25km$ long SMF. The validity of the method is confirmed as the temperature profile is corrected. A systematic error, which is around $12K$, is hereby eliminated. The compensation functions can be combined with a numerical filtering function so that no additional computation time is needed to perform the compensation.

Finally, different modulation formats are considered in order to reduce the quantum noise of the APDs, or increase the amplitude of the fundamental frequency of the received signals. It is found that it is theoretically possible to achieve a reduction of standard deviation of temperature data-points of 35% compared to sine modulation, by use of square wave modulation with a duty-cycle of 37%, but problems with interference of higher-order harmonics arise. Requirements for the elec-

trical band-pass filters become more strict, and direct modulation of the pump laser becomes problematic. Because of various limitations of the existing DTS, only sine modulation is utilised in actual measurements.

# Chapter 7

# Representative Results Obtained by the Sensor

This chapter comprises some of the results obtained by the distributed temperature sensor (DTS). Several optical modules with different lasers and optical filters, in combination with single-mode fibre (SMF), as well as graded-index multi-mode fibre (GIMMF) were used.

Some predictions from Chapters 4, 5 and 6 are confirmed. The possible temperature accuracy, range and resolution are demonstrated.

Furthermore, the need for a polarisation scrambler for DTS using SMF is justified; an example without the scrambler is shown.

## 7.1 MMF 1510nm system

Temperature measurements with a high-power pump laser $P_0 \approx 100mW$, $\lambda_c = 1510nm$ and $7.8km$ graded-index multi-mode fibre are presented here. The optical filter module is principally the same as described in Section 4.4, but in this case it is pigtailed with MMF and designed for $\lambda_c = 1510nm$.

Seven series of measurements were made with resolution spanning from $0.45m$ to $3.6m$, while the receiver bandwidth varied from $10 - 320Hz$. Pump power and modulation depth were the same in all experiments. For each set of parameters, around 50 measurements were made, so that the standard deviation could be calculated reliably. The

measured STDs were fitted by exponential functions. Spatial averaging was performed on the measurements, and there was no filtering in the frequency domain. The results are shown in figure 7.1.
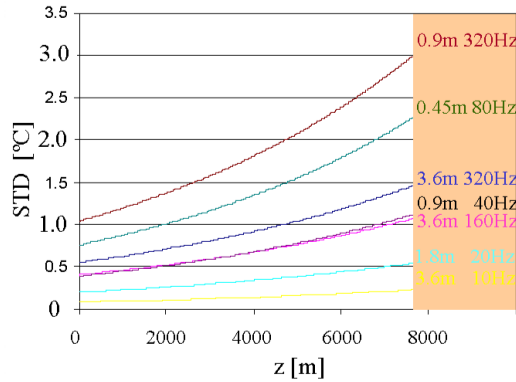


**Figure 7.1:** Fitted standard deviation for seven series of temperature measurements on $7.8km$ GIMMF.

The fitted exponential curves for the standard deviation are normalised by a function $\sqrt{\frac{\Delta z}{B_e}}$ to demonstrate the validity of equation (4.15).
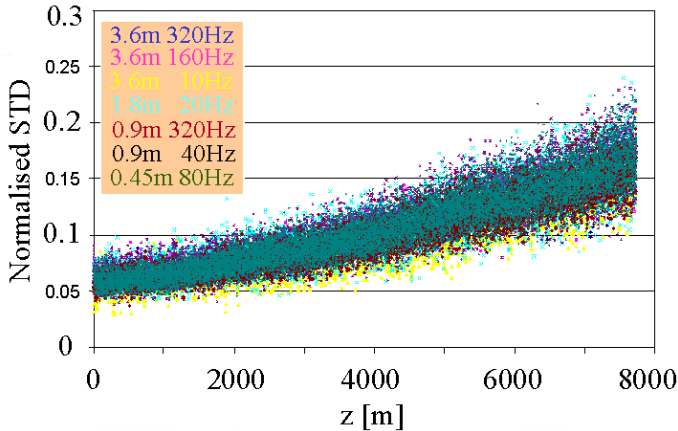


**Figure 7.2:** Measured standard deviations of temperature profiles of $7.8km$ GIMMF, normalised by the square root of the measurement time per data point and spatial resolution.

All curves fall nearly on the same exponential line. Equation (4.15) proves to be applicable, and an estimate of the accuracy for this particular system can be quickly obtained from the expression

$$STD(z) = 0.06e^{0.000135z}\sqrt{\frac{B_e}{\Delta z}}, \tag{7.1}$$

where the constants are determined so as to fit the measurements.

It was also experimentally found that the total measurement time is given by

$$t_{tot} = 1.3\frac{L_{max}}{\Delta z B_e}, \tag{7.2}$$

where the factor 1.3 is due to the stabilisation time for the receiver circuitry. Otherwise, equation (4.16) is correct. The typical measurement time here is a few minutes.

## 7.2   SMF 1493nm system

A number of measurements on $13.8km$ SMF were performed with the system comprising the high-power laser with $\lambda_c = 1493nm$ and average output power $97mW$. An example of the temperature profile and the standard deviation are shown in figure 7.3. The STD can be reduced
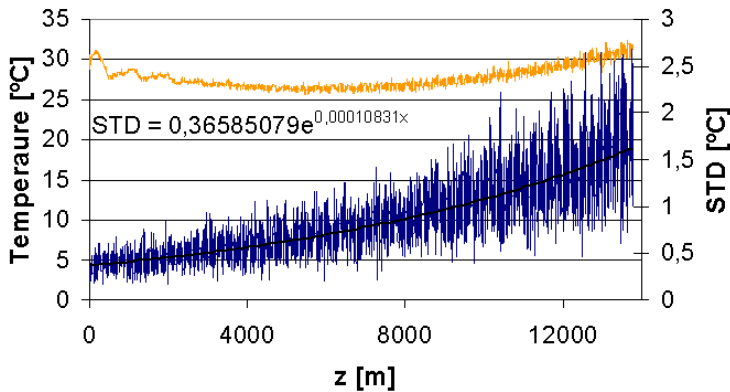


**Figure 7.3:** Temperature and standard deviation on 14km SMF. $P_0 = 97mW$, $\Delta z = 3m$, $B_e = 96Hz$, and no filtering was applied.

further by LP filtering, by a factor of around 1.4. Having this result, equation (4.15) can be used to estimate standard deviations for other pump powers, resolutions, measurement times and ranges, just like in the case of GIMMF.

## 7.3   Comparison between SMF and GIMMF

Finally, an experimental comparison between the SMF and GIMMF is presented here. The measurements on $13.8km$ SMF and $7.8km$ GIMMF with the same resolution and measurement time per data-point ($B_e = 96Hz$) are shown in figure 7.4. Clearly, the influence of the SRS in GIMMF is smaller. The oscillations in the first $3 - 4km$ are again due to electrical cross-talk between strong reference and weak Raman signals.
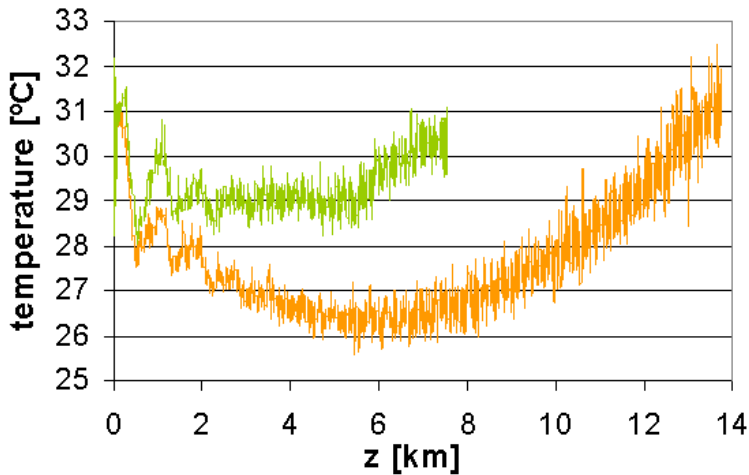


**Figure 7.4:** Temperature profile measured with SMF and GIMMF, using the same parameters.

The standard deviation is plotted in figure 7.5, where the fact that the measurement time on the SMF is twice as long is compensated by a factor of $1/\sqrt{2}$. The crossing point of the calculated standard deviations is at around $13km$, which is very close to the theoretically predicted value from Section 6.2.1. The small discrepancy may be due to different filters

and APDs in the SMF and MMF setup, but also to the approximative nature of the theoretical prediction.
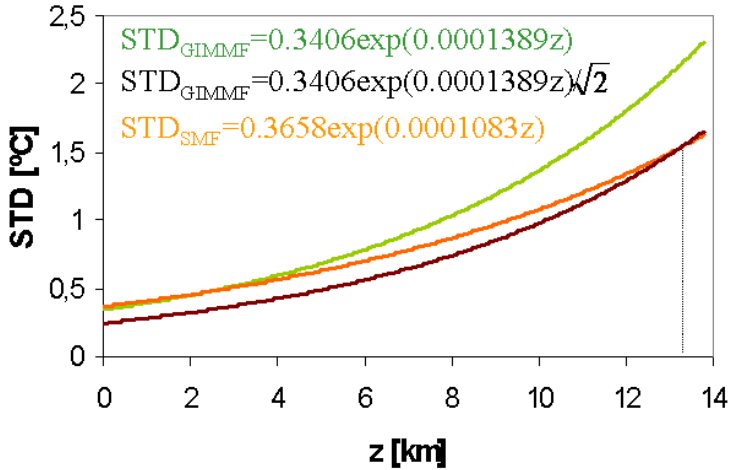


**Figure 7.5:** Exponential fit of the standard deviation of temperature measured with SMF and GIMMF.

## 7.4   24km experiment

An experiment with a $24km$ SMF was also performed to investigate the possibility to extend the sensor range even further. Measurements with $\Delta z = 3m$, $B_e = 96Hz$ and $P_0 = 100mW$, are shown in figure 7.6. The influence of SRS is very strong, but there is still a possibility to perform the measurement of temperature and to detect the fibre end. To obtain distributed temperature measurements with acceptable deviations, a longer measurement time is needed, though.

## 7.5   1550nm systems

The possibility to shift the pump wavelength to $1545nm$ and amplify the pump with an Erbium-doped fibre amplifier (EDFA) was also investigated for possible systems with range exceeding $15km$.
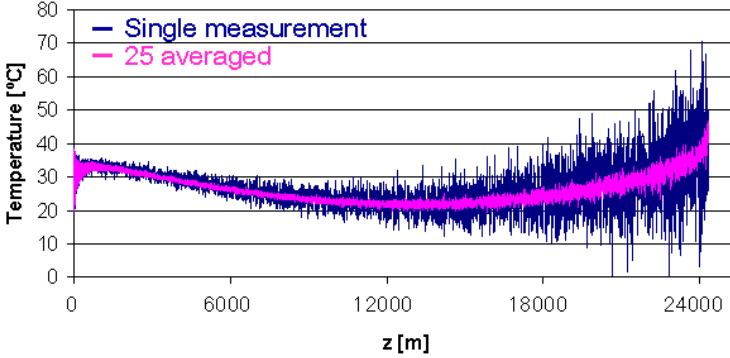
**Figure 7.6:** Temperature profile on 24km long SMF.

A pump laser providing $6mW$ was amplified by an EDFA with a maximum output of $23dBm$. However, at modulation frequencies up to $50kHz$, the amplifier depleted, and could not provide linear gain to the pump. This distorted the sine-modulation, and made temperature measurements erroneous. At higher modulation frequencies, the EDFA functioned well, but still, SBS affected the pump power, since the linewidth of the laser was approximately $0.1nm$.

Measurements with low pump power ($6mW$) were conducted though, with both GIMMF and SMF. Figure 7.7 shows the temperature profile and the STD on $7.8km$ GIMMF. Again, the oscillations of the temperature profile are due to strong crosstalk between very weak Raman signals and strong reference signal. Here $B_e = 60Hz$, $\Delta z = 3m$, and the number of points is $N = 4096$.

Figure 7.8 shows the temperature profile and STD measured on $13.8km$ SMF, together with an exponential fit of the STD. The resolution is $\Delta z = 3m$, the effective bandwidth $B_e = 22.4Hz$, and $N = 8192$.

The standard deviation of measurements with SMF and GIMMF with the low-power $1545nm$ pump laser are compared. After re-scaling with the factor $\sqrt{B_{e,SMF}/B_{e,GIMMF}}$, the standard deviations are shown in figure 7.9. When the pump wavelength is shifted to $1545nm$, the crossing point between the standard deviations is again at $\approx 13km$. Note however, that the width of optical filters of these SMF and MMF systems differs significantly. With equivalent filters, a change in the
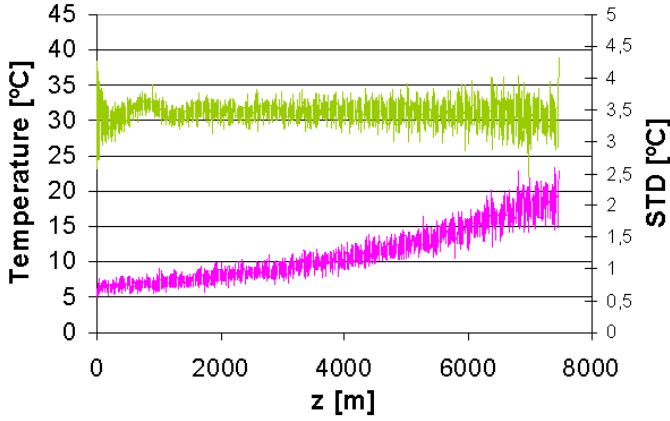
**Figure 7.7:** Measured temperature profile and standard deviation on $7.8km$ GIMMF, with $B_e = 60Hz$, $\Delta z = 3m$ pump $\lambda_c = 1545nm$ and $P_0 = 6mW$.
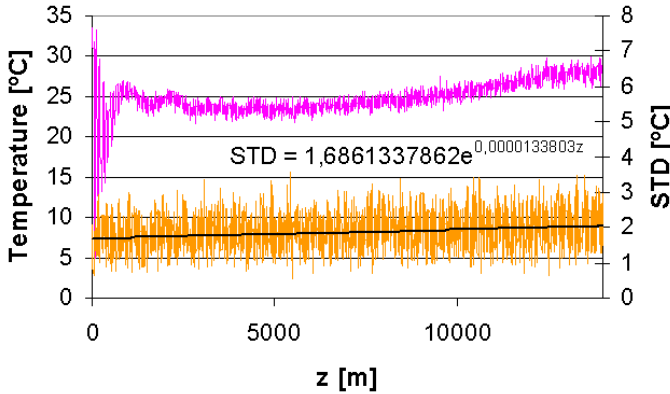


**Figure 7.8:** Measured temperature profile and standard deviation on $13.8km$ SMF, with pump $\lambda_c = 1545nm$.

crossing point to lower range is expected, since the attenuation of SMF is smaller at this wavelength, while it is approximately the same in GIMMF.

Finally, measurements with pump laser $\lambda_c = 1545nm$, and $\lambda_c = 1493nm$ are also compared. The results are scaled according to equation (4.15), and plotted in figure 7.10. The standard deviation of the $1545nm$ system grows slowly, and the crossing point is at approximately $13km$.
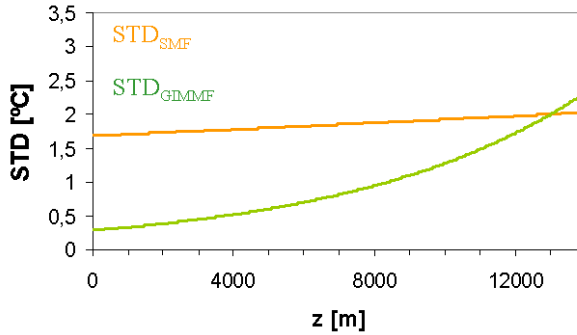
**Figure 7.9:** Standard deviation as a function of length in SMF and GIMMF, with pump $\lambda_c = 1545nm$.
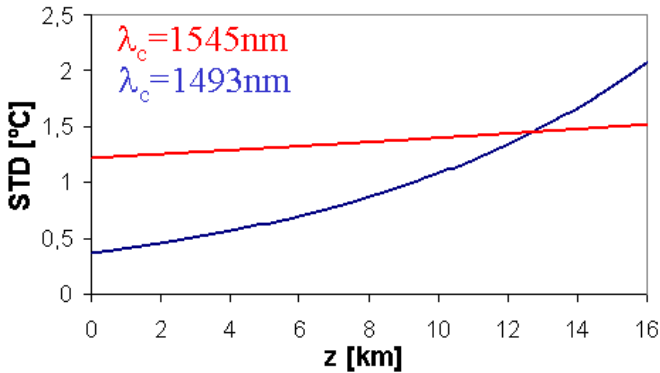


**Figure 7.10:** Standard deviation as a function of length in SMF, with pump $\lambda_c = 1545nm$ and $\lambda_c = 1493nm$.

This is not far from the value predicted in Section 6.1.

## 7.6 Polarisation scrambling

It is necessary to include a polarisation scrambler right after the pump laser, as indicated in Section 4.3. Uncontrolled polarisation of the pump waves results in an unpredictable scattering cross-section, and thus in uncertainties in determining the temperature. Figure 7.11 shows a temperature profile along SMF at room temperature where strongly po-

larised pump was launched into the fibre. 20 measurements were made,
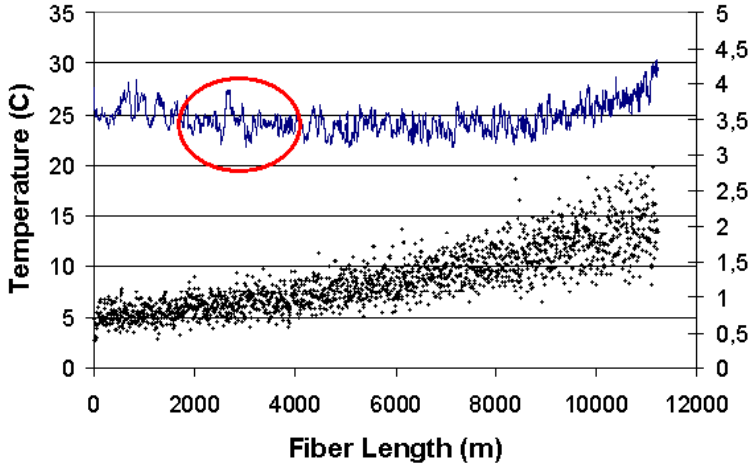


**Figure 7.11:** Temperature profile along an SMF without polarisation scrambling of the pump laser (solid line). Standard deviation (dots) based on 16 consecutive measurements is also shown (right axis).

and the standard deviation was calculated. A resolution of $6m$ and a long acquisition time were used to minimise the noise. The variations in the marked region exceed $5^oC$, while the standard deviation is around $1^oC$ in that region. Clearly, there is a systematic pattern imposed on the real temperature profile. The pattern changes slowly over time or when a section of the fibre is bent. With insertion of a polarisation scrambler, the pattern nearly vanishes.

Finally, note that a polarisation scrambler is not strictly needed with SIMMF since many modes with different polarisations are automatically excited already in the beginning of the fibre.

## 7.7   Summary

Some typical measurements and an analysis of these measurements are presented in this chapter. SMF and GIMMF were used together with pump lasers at $\lambda_c \approx 1500nm$ and $\lambda_c \approx 1550nm$.

The procedure for estimating temperature accuracy, developed in Section 4.7, was put under test, and it showed good agreement with

the observed data. Thus, it enables one to evaluate the sensor perfor-
mance when various parameters, such as range, measurement time and
resolution are varied.

Curves obtained with the GIMMF and SMF are compared, and it
was found that the standard deviation of temperature points is smaller
when using GIMMF up to $13km$. However, the main advantage of the
GIMMF over the SMF system is the reduced impact of non-linearities
(SRS) due to the larger core area of the multimode fiber. Therefore,
GIMMF may be preferred for even longer ranges.

A measurement on a $24km$ SMF system is also presented to demon-
strate the possibility to increase the range significantly, when low-loss
fibres are used.

# Chapter 8

# Fibre Bragg grating sensor

This chapter introduces a different type of a fibre-optic sensor. The combined strain and temperature sensor based on fibre Bragg gratings (FBG) is presented. Heating, contraction and elongation of the Bragg grating changes its reflectance characteristics, wherefrom it is possible to deduce the change in the applied stress and temperature.

Fibre-optic strain sensors based on fibre Bragg gratings have found applications in the monitoring of large-scale concrete structures [5] [45]. They have the primary advantage over conventional electrical strain gauges in that they are not subject to drift, thus making them ideal for the use in long term monitoring of large-scale structures. Furthermore, their small size gives them more flexibility in their use, allowing the potential for unobtrusively embedding them into the concrete so as to directly measure the bulk strains of the structure as well.

## 8.1 FBG as a Sensor

FBG reflects a narrow interval of wavelengths due to its periodic structure. When the grating period or the effective refractive index in the fibre is changed, the interval of reflected wavelengths shifts. This makes FBGs suitable for sensor operation.

The Bragg grating wavelength $\lambda_B$, which is here defined as the centre wavelength of the back-reflected light from a Bragg grating, depends on the effective index of refraction of the core and the periodicity of the grating. The effective index of refraction, as well as the periodic spacing

between the grating planes, will be affected by changes in the applied strain and the temperature of the fibre where the grating is embedded. The functional dependence of the mode refractive index is given by the relationship [5]

$$\partial n_{eff} = \frac{\partial n_{eff}}{\partial T} \cdot \Delta T + \frac{\partial n_{eff}}{\partial \varepsilon_z} \cdot \Delta \varepsilon_z \tag{8.1}$$

where $\frac{\partial n_{eff}}{\partial T}$ is the temperature coefficient, $\Delta T$ is the change in temperature, $\frac{\partial n_{eff}}{\partial \varepsilon_z}$ is the longitudinal stress optic coefficient, and $\Delta \varepsilon_z$ is the applied longitudinal strain.

The change in the effective mode index and periodicity induced by the strain $\Delta \sigma_z$ and temperature $\Delta T$ change, shifts the Bragg wavelength by $\Delta \lambda_B$ [5].

$$\begin{aligned}
\frac{\Delta \lambda_B}{\lambda_B} &= \left(1 - \frac{n^2}{2} \cdot [p_{12} - \nu \cdot (p_{11} + p_{12})]\right) \cdot \Delta \varepsilon_z \\
&+ \left(\frac{1}{\Lambda} \cdot \frac{\Delta \Lambda}{\Delta T} + \frac{1}{n} \cdot \frac{\Delta n}{\Delta T}\right) \cdot \Delta T \\
&= (1 - \Xi) \cdot \Delta \varepsilon_z + (\alpha_\Lambda + \alpha_n) \cdot \Delta T
\end{aligned} \tag{8.2}$$

where the first term accounts for the change in the longitudinal strain, and the second term for the change in temperature. $n$ is the refractive index of the core, $p_{ij}$ are Pockel's coefficients, $\nu$ is the Poisson's ratio, and $\Lambda$ is the grating period. The coefficient $\Xi$ is fibre- and grating-specific, and is measured to be 0.22, so the pure strain dependence is simplified to

$$\frac{\Delta \lambda_B}{\Delta \varepsilon_z} = \lambda_B \cdot 0.78 \cdot 10^{-6} \mu\varepsilon^{-1} \tag{8.3}$$

Thus, a change in the longitudinal strain of $1\mu\varepsilon$ results in a shift $\Delta \lambda_B$ of around $1.2pm$ at $1550nm$.

In the second term of equation (8.2), the two coefficients stand for two temperature dependent processes. Namely, one can distinguish between the thermal-optic (TO) effect and the thermal-expansion (TE) effect. The two effects are represented by constants $\alpha_n$ and $\alpha_\Lambda$, respectively. TO originates from the change of refractive index of silica glass in the fibre core due to the temperature dependence of refractive index, while TE is due to volume change of glass with temperature. Both effects

alter the Bragg constant and thus the Bragg wavelength. The thermo-optic coefficient $\alpha_n$ of a silica fibre is measured to be $6.67 \cdot 10^{-6} K^{-1}$ [5]. Thus, TO is the dominant effect for an FBG which is not encapsulated, as the TE constant is only around $\alpha_\Lambda = 0.35 \cdot 10^{-6} K^{-1}$.

Temperature dependence of the Bragg wavelength must be found after the grating is encapsulated, since the encapsulation may also induce some strain on the fibre. Encapsulation procedure is described in Appendix H.

## 8.1.1   Temperature calibration

Encapsulating the fibre with stainless steel rods gives additional contribution to the temperature dependence. Namely, the thermal expansion coefficient of stainless steel (up to $100^o C$) is around $10 - 15 \cdot 10^{-6} K^{-1}$ [46] and consequently, a certain strain is induced in the fibre by expansion or contraction of the encapsulation. It is therefore necessary to measure the response of the entire sensor-head to changes in ambient temperature.

Four such sensor-heads with non-overlapping Bragg wavelengths are made and connected in line. The unstrained encapsulated gratings are submerged in water-tank with slowly-varying temperature. The temperature of water is monitored, and, as it changes, $\Delta\lambda_B$ is noted for every degree. The temperature in the tank spans from $20^o C$ to $41^o C$ in the regarded time interval. Figure 8.1 shows $\Delta\lambda_B$ as a function of time, while the water temperature changes.

As shown in figure 8.2, $\Delta\lambda_B$ of the FBG temperature sensor changes linearly with temperature.
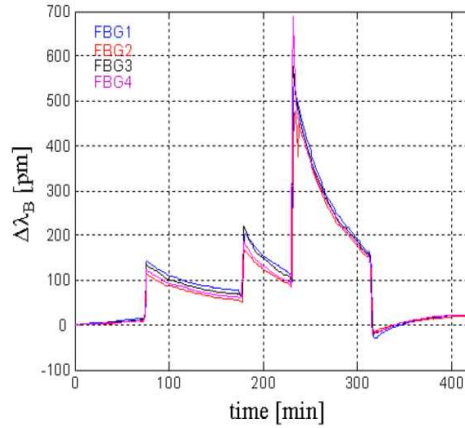
**Figure 8.1:** $\Delta\lambda_B$ as a function of time, while the water temperature changes (min $20^oC$, max $41^oC$). The sensitivity of the four tested sensors is very similar.
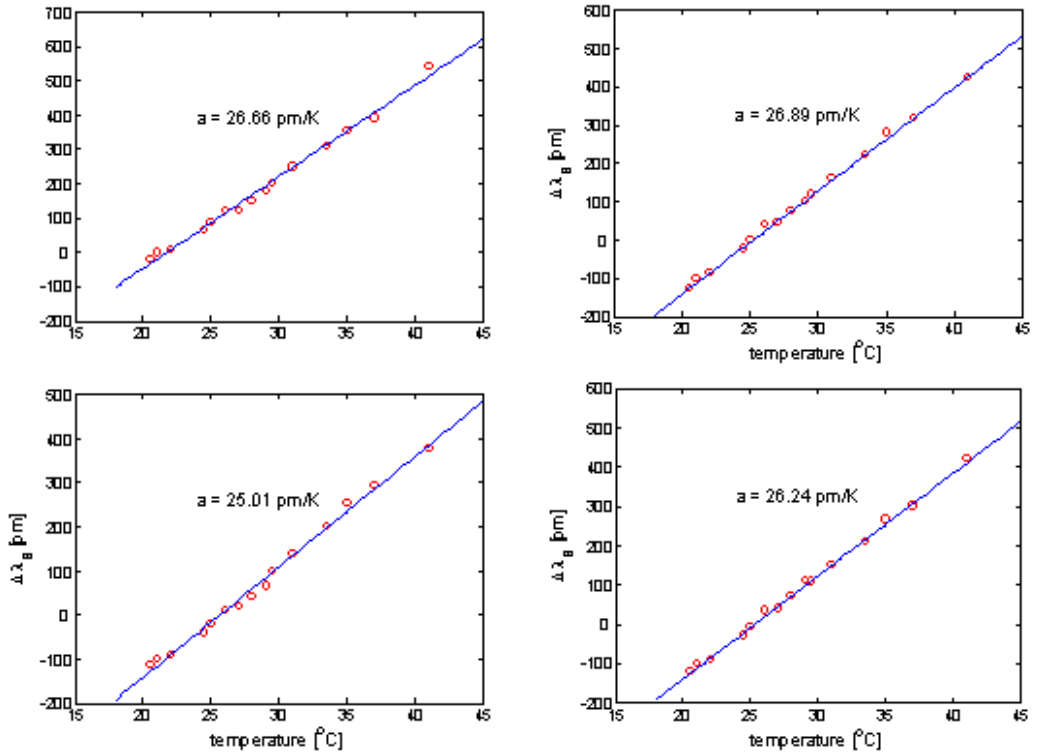


**Figure 8.2:** Bragg-wavelength shift as a function of temperature for the four encapsulated FBG sensors, together with a linear fit.

The gratings have nearly the same slope and hence very similar response to temperature changes. (The repeatability of the encapsulating is thus satisfactory.) The mean value of the slope is $\mu_a = 26.2 pm/K$, and the STD in the four samples is $\sigma_a = 0.84 pm/K$.

One can find that the expansion of the rods induces a strain of $13.04 \mu\epsilon/K$, which is within the expected range of value. These coefficients are measured with a repeatability of 3% in other three sensors. Moreover, the TE coefficient of stainless steel varies for different types, and may not be constant in different temperature intervals. Here several factors contributed to the uncertainty. It is mostly the fabrication non-uniformities, but also the uncertainty of the measurement itself.

## 8.2 FBG strain sensor system based on tuneable laser

The experimental quasi-static strain sensing system employing an active interrogation scheme using a tuneable laser source (TL) and a computer, plus the four FBG sensor heads, is developed for installation on civil engineering structures such as bridges. The system is designed to automatically upload and download data so as to allow for its use in remote locations.

A sketch of the strain measurement system is shown in figure 8.3. The tuneable laser (TL) scans with high resolution an interval of wavelengths and returns to the computer the reflection spectrum of the fibre containing fibre Bragg grating sensors (FBGs). The scanning is repeated periodically and the device measures the change in strain applied on the FBGs by recording the change in reflected wavelengths.

The user controls the measurement system via a notebook. The developed control software also allows to write the control file via internet on the laptop and change the settings, and receive measurement results via e-mail. The computer has full control over the TL and issues commands and receives data using the GPIB interface. This kind of connection allows the computer to be up to 20 meters away from the TL and have flawless communication. This is a recognized standard interface used in industrial control systems. All data are recorded on the hard-disc and, if a computer network is accessible, it is sent via e-mail to a monitoring and data-processing centre.
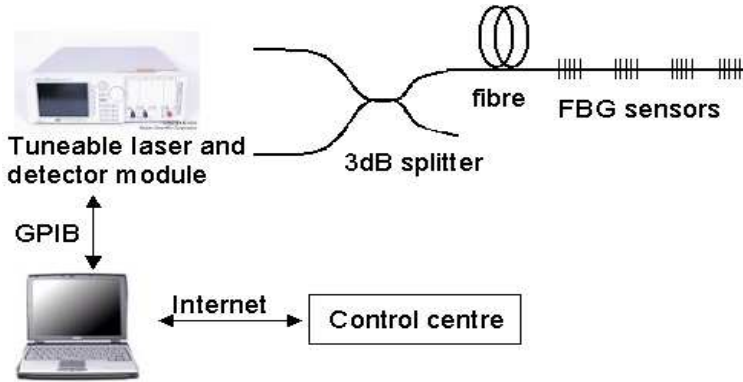
**Figure 8.3:** Instrumentation setup for the measurements.

### 8.2.1    Scanning

To avoid repeated scanning of the entire wavelength spectrum of the
TL, the initial scan locates the Bragg wavelengths of the specified num-
ber of gratings. When the gratings are detected, only small wavelength
intervals (of width $1nm$) are scanned with high resolution to make the
actual strain measurements. The centre wavelength of the FBGs is reg-
ularly updated (every hour), so that when high strain is applied, or the
ambient temperature changes significantly, the Bragg wavelength does
not escape from the scanned windows. The program runs faster and can
thus perform measurements more frequently. It takes approximately one
minute to scan four gratings if this scheme is used and more than three
minutes if the entire spectrum is scanned, even with somewhat poorer
resolution.

The tuneable laser scans the reflection spectrum with $5pm$ between
consecutive points. According to equation (8.3), this would give a resolu-
tion of $4.16\mu\varepsilon$. To increase the resolution and avoid influence of possible
fluctuation of TL power, lines are fitted at the edges of the reflectance
curve of each FBG. The slope and interception of the lines yield the
crossing point with the threshold value without the quantisation error.
Six points are used in fitting the line at each grating.

The maximum reflectance of a grating may fluctuate slightly and
depends on the density of points in the scan. Therefore, the maximum,
which is used when determining the threshold value, is calculated as the

average of the "top" points. The linear fit of the edges is shown in figure 8.4 with the threshold value.
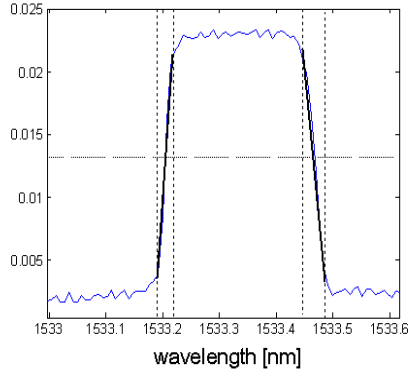


**Figure 8.4:** Reflectance of a Bragg grating. A line is fitted to approximate the edges and omit the quantization error due to scanning resolution.

### 8.2.2 Sensor performance in laboratory environment

Prior to field trials, the sensor is tested in the laboratory.

The FBGs, which are not encapsulated, respond when the fibre is subjected to small longitudinal force. Figure 8.5 shows that there is an increase of approximately $4\mu\varepsilon$ every time a weight of $4 - 5g$ stretches the fibre with an FBG. Temperature was stabilised.

In metal packaging, greater force needs to be applied to detect a change in the strain. Encapsulated strain sensor was ballasted with $1.5kg$. Figure 8.6 shows the response.

The encapsulated gratings were not temperature stabilised, and there is an obvious correlation between the readouts of the four gratings. Variations in the ambient temperature contribute to the inaccuracy of strain measured in an uncontrolled environment. In field trials, to suppress the influence of temperature on the results, one FBG can be used as a temperature sensor, i.e., it is not attached firmly to the measured surface so that only temperature fluctuations alter its Bragg wavelength. Since the gratings are supposed to be installer near each other in the experiments, and the concrete (e.g. a bridge) acts as a big heat reservoir, the temperature can be assumed to be the same at all four points where FBGs
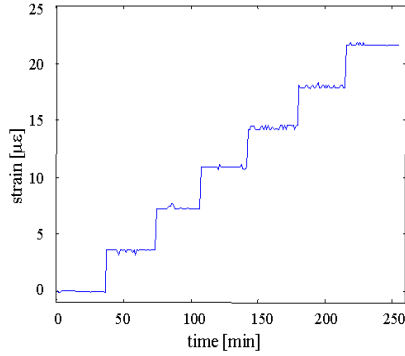
**Figure 8.5:** The FBG sensor is loaded longitudinally with several weights. The figure shows strain versus time. Standard deviation is calculated for all loads.
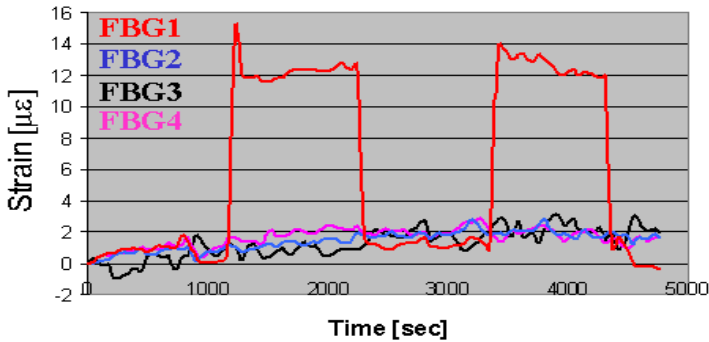


**Figure 8.6:** Strain as a function of time measured by the encapsulated FBG sensors. One sensor-head is ballasted with $1.5kg$ to produce the visible change in the strain.The standard deviation of measured strain is around $1\mu\varepsilon$ when the base-line is corrected for temperature variations.

are installed. With measured temperature, it is possible to subtract its influence on other gratings.

Both temperature and strain are measured with certain inaccuracy. The two errors are not correlated, so that the total standard deviation is found to be around $2\mu\varepsilon$.

The output power of the TL is also monitored constantly, but the TL offers a very good control of this parameter, and power variations

do not have an effect on the final results.

## 8.3 Field test of the strain sensor system

The field tests are conducted at the bridge over Shepherd's Creek, Lake Macquarie, NSW, Australia. This bridge is selected as it is the first bridge in Australia to employ Reactive Powder Concrete (RPC) [47] [48] in the casting of its girders. RPC has very high strength and is capable of withstanding compressive stresses in excess of $160MPa$. The bridge represents an advancement over the Magog River Pedestrian Bridge in Quebec [49], the first in the world to use reactive powder concrete, in that it is open to traffic and thus with the use of an intelligent monitoring system this new construction material can be field tested to its full extent.

The experiment that is conducted on the particular bridge consists of two parts. First, strain activity over a two-day period is monitored. The traffic over the bridge is not controlled. In this experiment it was intended to study bridge behaviour as the ambient temperature changes. In second part, the traffic is stopped, and a truck with varying load is parked on the bridge.

Four FBG sensor heads are surface-mounted in the middle of a girder and under the bridge deck to monitor the strain and temperature movement. Simultaneously, the strain is measured with electro-mechanical gauges too. The placement of the sensors is sketched in figure 8.7.

### 8.3.1 Field trial 1

Figure 8.8(a) shows the calculated temperature under the bridge, using the calibration curve. The measurement started Friday afternoon, and lasted 46 hours. The temperature has modest variations - the difference in maximum and minimum is only $3^oC$.

Once the temperature is determined, it is possible to suppress the temperature effect from the strain-measuring FBGs. Figure 8.8(b) shows the strain as function of time at the three measurement points. The data are averaged (moving average) to remove high-frequency noise. The strain curves follow closely the temperature variations and highest absolute strain change is detected in sensor FBG4, lowest in sensor FBG1.
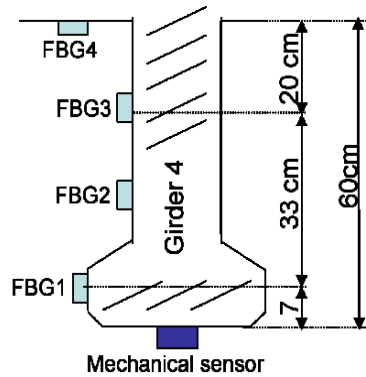
**Figure 8.7:** Four FBG sensors are installed on the RPC girder and bridge-deck as well as one electromechanical strain gauge.
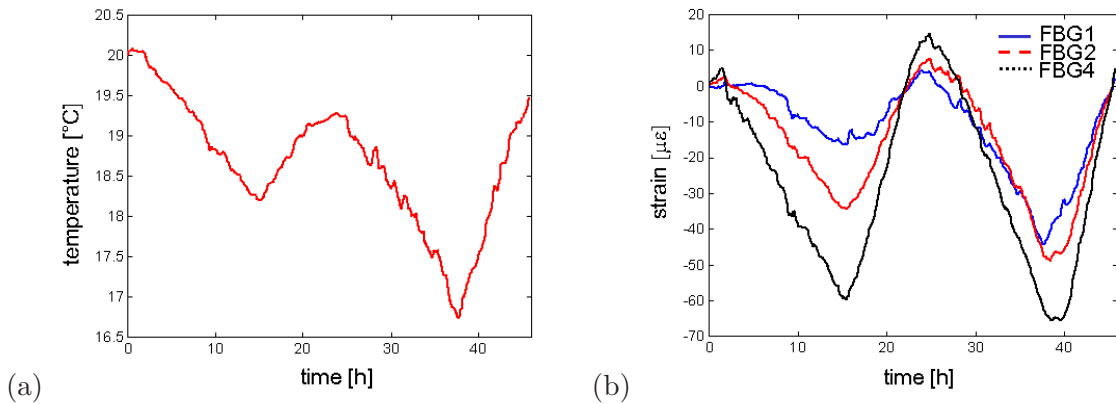


**Figure 8.8:** (a) Measured temperature variation over the two-day cycle (b) Strain variation over the two-day cycle at the three measurement points.

### 8.3.2   Field trial 2

In the second part of the experiment, a truck with varying load is parked in three lanes of the bridge for several minutes. The girder on which the sensors are mounted lies under the middle lane. The total mass of the truck ballasting the bridge is firstly 20.67T, 27.48T, 34.28T and finally 41.04T. Figure 8.9 shows the strain in FBG1 as the truck changes lanes and its load.
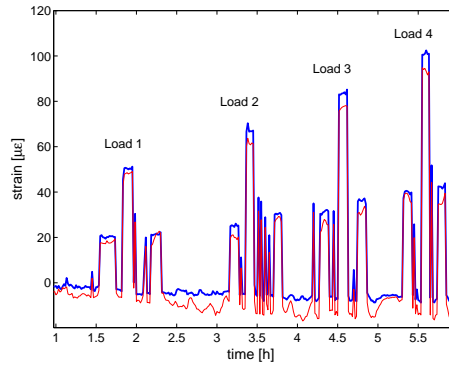
**Figure 8.9:** Measured strain in FBG1 for the four loads in the three lanes of the bridge, with (solid) and without (thin) compensating for temperature variations.

Figure 8.10 shows the induced strain in FBG1, FBG2 and strain gauge sensor, as a function of the truck weight in the middle lane.
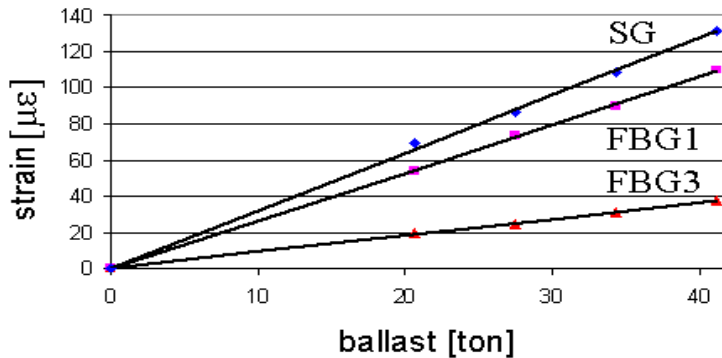


**Figure 8.10:** Strain in the electromechanical strain gauge (SG), FBG1 and FBG3 as function of the ballast in the middle lane.

Electro-mechanical strain sensor yields similar results to those of the FBGs. The difference originates from different placement of the sensors. The mechanical sensor, as shown in figure 8.7, is placed on the bottom of the girder where the deformation under load is highest, and thus measures higher strain. The strain grows linearly with the ballast for these values of the load. The load-strain curve is not linear when the truck is in lanes one and three. The third strain sensor, which is under

the bridge deck and not on the girder, shows very small, even negative read-out. The temperature change, and thus contraction of the bridge is, however, registered very clearly.

The efficiency of temperature compensation is illustrated in figure 8.11. It shows the strain, the temperature and the strain compensated for temperature vs. time in FBG1 while the 20.67 tonne load is positioned above and to each side of the girder being measured.
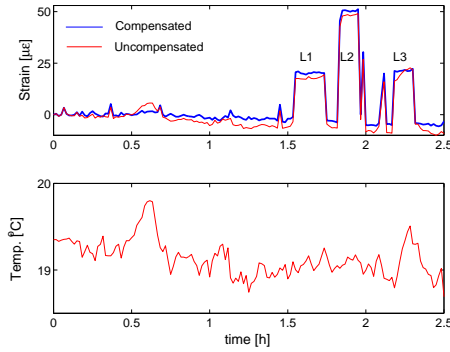


**Figure 8.11:** Temperature compensation scheme successfully removes "bumps" originating from temperature fluctuations, from the strain curve. L1, L2 and L3 indicate the strain in the three lanes of the bridge.

## 8.4 Summary

Sensitivity of fibre Bragg gratings to temperature and strain is exploited in sensor technology. The Bragg wavelength shifts as the effective mode index and the grating periodicity change.

FBG gratings are encapsulated, and tested for temperature and strain response, after which the calibration is performed. The estimated accuracy of the sensor is $\pm 2\mu\varepsilon$ in a slowly varying temperature environment.

FBG-based strain sensor system utilising a tuneable laser is successfully tested in a field trial. An array of four sensor heads was mounted on a concrete bridge. The results agree well with the theoretical expectation with respect to maximum strain variations and correlation to the ambient temperature, as well as the results obtained with another sensor type. The repetition rate of measurements was one minute.

The good signal-to-noise ratio obtained by use of the tuneable laser offers the potential of many more FBGs connected in series, especially if narrow-band gratings are used.

Monitoring the strain over long time shows movement of the bridge as the temperature changes, or some static load is applied on the structure. But this may not always satisfy needs of a sensing system. For example, it is can be interesting to measure the vibrations in the bridge as a consequence of a truck running over it. Dynamic strain measurement with high sampling frequency is also possible, but it is not included in this thesis.

Ease of installation and remote control are among the benefits which make this sensor system an attractive alternative to the electro-mechanical strain gauges.

# Chapter 9

# Conclusions

Finally, general conclusions are summarised here, and some suggestions for possible further work in the area.

## 9.1   General conclusions

Two types of distributed fibre-optic sensors were designed and analysed during the course of the study, namely Raman temperature sensor and FBG strain and temperature sensor.

Theory behind the Raman scattering was studied and understood in order to construct an efficient sensor which takes advantage of the temperature dependent spontaneous Raman scattering.

Two techniques for localisation of the backscattering were considered: incoherent optical frequency-domain reflectometry and the optical time-domain reflectometry. The analysis showed that it is advantageous to use IOFDR in cases where the temperature changes slowly with time, and when conventional APD photo-detectors are used. It is not necessary to cool the detectors. According to the presented theory, using OTDR, one can obtain the same, or ultimately even better accuracy than with IOFDR, but much more complex and costly detection schemes are necessary.

Thorough analysis and optimisation process of the optical module of the temperature sensor were conducted and verified through experiments and numerical modelling of the system. Several fibre types were tested in order to find the relevant parameters for choice of the sensing fibre.

Numerical aperture, attenuation, mode area and even dispersion are of the main concern. The possibility to combine different fibres and take advantage of their respective characteristics was also suggested. In fibres with a small mode-area, stimulated Raman scattering posed a significant problem. However, it was shown that this problem can be solved to certain extent, by applying compensation functions. Furthermore, it was found that the pump wavelength should be moved to the low-loss region if long range is required. Various modulation formats were suggested and tested, but with current electronics of the device, problems with interference of higher-order harmonics deteriorated the measurements.

The noise of the entire system was characterised, and the standard deviation of the temperature was derived as a function of range, spatial resolution, measurement time and detector parameters. A useful computer model was developed to simulate the entire sensor, and various signal processing methods for noise suppression were evaluated.

A large number of measurements was made, and some of these results are presented in this thesis. It was found that the graded-index multi-mode fibre used in the experiments performs better than the standard transmission single-mode fibre up to a length of around $13km$. As the sensor range increases more ($> 15km$), the single-mode fibre becomes the better choice. The graded-index MMF is thus a step between the step-index MMF and the SMF.

As an example of performance with GIMMF, it is possible to obtain approximately $8km$ range, spatial resolution of $1m$, standard temperature deviation of $1^oC$, with measurement time of around 4 minutes.

Finally, a temperature and strain sensor utilising a number of fibre Bragg gratings interrogated by a tuneable laser was also successfully demonstrated. Field trials on a bridge were conducted in parallel with measurements using the standard equipment for such purposes. It was shown that the fibre-optic solution is more convenient and at least as accurate. Standard deviation of the FBG strain sensor was estimated to around $2\mu\varepsilon$, while the repetition time with the used tuneable laser was around one minute. It was also shown that using the FBGs, it is possible to measure the ambient temperature with great accuracy ($\approx 0.1^oC$) at a single point.

Generally, the entire study was a mixture of theoretical and experimental work where various fields of engineering were exercised. Comple-

tion of the design, construction and test of the two sensors was a truly rewarding work.

## 9.2   Further research

Fibre sensors have been the subject of research for decades, but their actual implementation and breakthrough has been relatively slow. Fibre-optic solutions usually offer higher precision at an accordingly higher price, compared to other sensor types. However, the areas of applications are constantly emerging, and the demand for ever more accurate and farther reaching sensors motivates to continue improving the fibre-optic sensor technology.

Besides intelligent algorithms which could use the already gathered data to reduce the standard deviation, some hardware improvements are also possible. Application of the advanced modulation format can only be realised with new electronics with narrow electrical band-pass filters which can suppress efficiently the higher-order harmonics. The pump-power threshold, at which signals become degraded, is far from reached, so appearance of new high-power lasers is welcomed by the sensor. New types of fibres which are resistent to high temperatures are becoming available, and use of these fibres in long-range temperature sensing should be investigated.

# Bibliography

[1] M. A. Farahani and T. Gogolla, *Spontaneous Raman Scattering in optical fibers with modulated probe light for distributed temperature Raman Remote Sensing*, J. Lightwave Technology, 17, pp. 1379-1391, 1999.

[2] Zhang Zaixuan, I. S. Kim, W. Jianfeng, F. Haiqi, G.Ning, Y. Xiangdong, L. Honglin, W. Xiaobiao, O. Sangiki, Y. Kim, *10km Distributed optical fiber sensors system and measuring network*, Proceedings of the Second International Symposium on Instrumentation Science and Technology, Vol.3, pp.302-307, 2002

[3] Z. Zaixuan, L. Honglin, G. Ning, W. Jianfeng, W. Xiaobiao, Y. Xiangdong, F. Haiqi, I. S. Kim, *30km distributed optical fiber Raman photons temperature Lidar*, in Lidar Remote sensing for Industry and Environment Monitoring III, Proc. SPIE 4893, pp. 78-82,2003.

[4] Y. T. Cho, M. Alahbabi, G. Brambilla, T. P. Newson, *Brillouin based OTDR with measurement range of 85 km using combined EDFA and Raman amplification*, CLEO 2004, vol 1, 2004

[5] Allan D. Kersey, Michael A. Davis, Heather J. Patrick, Michel LeBlanc, K. P. Koo, *Fiber Grating Sensors*, Journal of Lightwave Technology, vol. 15, pp. 1442-1463, 1997

[6] D. K. Gifford, B. J. Soller, M. S. Wolfe, M. E. Frogatt, *Distributed Fiber-Optic Temperature Sensing using Rayleigh Backscatter*, ECOC 2005

[7] Y. Koyomada, Y. Eda, S. Hirose, S. Nakamura, K. Hogari, *Novel Fiber-Optic Distributed Strain and Temperature Sensor with Very*

*High Resolution*, IEICE - Transactions on Communications, Vol. E-89B, pp.1722-1725, 2006

[8] S. M. Chandani, N. A. F. Jaeger, *Fiber-Optic Temperature Sensor Using Evanescent Fields in D Fibers*, Photonics Technology Letters, Vol. 17, pp.2706-2708, 2005

[9] Govind P. Agrawal, *Fiber-Optic Communication Systems*, 2nd edition, John Wiley & Sons. Inc., 1997

[10] Govind P. Agrawal, *Nonlinear Fiber Optics*, 2nd edition, Academic Press Inc., 1995

[11] H. Kramers, W. Heisenberg, Z. Physik, Vol. 31, p.628, 1925

[12] C. V. Raman, K. S. Krishnan, *The Production of New Radiations by Light Scattering. Part I*, Proceedings of the Royal Society of London. Series A, Vol.122, No.789, 1929

[13] G. Landsberg, L. Mandelstam, *Scattering of light in crystals*, Zeitschrift fur Physik , Vol.50, pp. 769-780, 1928

[14] Y. R. Shen, N. Bloembergen, *Theory of stimulated Raman and Brillouin scattering*, Phys. Rev. Vol. 137A, pp.1787-1805, 1965

[15] R. H. Stolen, J. P. Gordon, W. J. Tomlinson, H. A. Haus, *Raman response function of silica-core fibers*, J. Opt. Soc. Am. B, Vol. 6, No. 6, June 1989

[16] Keith J. Blow, David Wood, *Theoretical Description of Transient Stimulated Raman Scattering in Optical Fibers*, J. Quantum Electronics, Vol. 25, No. 12, December 1989

[17] Dawn Hollenbeck, Cyrus D. Cantrell, *Multiple-vibrational-mode model for fiber-optic Raman gain spectrum and response function*, J.Opt.Soc.Am.B,Vol.19, No.12, December 2002

[18] S. Namiki, Y. Emori, *Ultrabroad-band Raman amplifiers pumped and gain-equalized by wavelength-division-multiplexed high-power laser diodes*, IEEE Journal on Selected Topics in Quantum Electronics, Vol.7, pp. 3-16,

[19] R. H. Stolen, *Nonlinearity in fiber transmission*, Proc. IEEE 68, pp.1232-1236 (1980).

[20] Robert W. Boyd, *Nonlinear Optics*, Academic Press, 1992

[21] D. A. Wardle, *Raman Scattering in Optical Fibres*, The University of Auckland, 1999

[22] R. A. Serway, C. J. Moses, C. A. Moyer, *Modern Physics*, Sounders College, Orlando 1997

[23] B.H. Brandsen, C.J. Joachain, *Quantum Mechanics*, 2nd Edition, Prentice Hall, imprint of Pearson Education Limited, 2000

[24] G. Grau, W. Freude, *Optische Nachrichtentechnik*, 3rd Edition, Springer Verlag, 1991

[25] G. Grau, W. Freude, *Optische Nachrichtentechnik*, 3rd Edition, Springer Verlag, 1991.

[26] E.J. Woodbury, W.K. Ng, Proceedings IRE, 1962

[27] K. Rottwitt, J. Bromage, A.J. Stentz, L. Leng, M.E. Lines, H. Smith, *Scaling of the Raman gain coefficient: Applications to Germanosilicate Fibers*, J. Lightwave Technology, 21, pp. 1652-1662, 2003

[28] R. H. Stolen, *Relation between the effective area of a single-mode fiber and the capture fraction of spontaneous Raman scattering*, Journal of Optical Society if America B, Vol.19, pp. 498-501, 2002

[29] E. Brinkmeyer, *Analysis of the backscattering method for single-mode optical fibers*, Journal of Optical Society of America, Vol.70, pp.1010-1012, 1980

[30] Y. Quian, J. H. Povlsen, S. N. Knudsen, L. Grüner-Nielsen, *Fiber Raman amplification with single-mode fibers*, Optical Amplifiers and their Applications, Vol. 44, pp. 128-134, 2001

[31] R.H.Stolen, E.P.Ippen, A.R.Tynes, *Raman oscillation in glass optical waveguide*, Applied Physics Lett., Vol. 20, p.62, 1972.

[32] D. Mahgerefteh, D. L. Butler, J. Goldhar, L.G. Joneckis, *Novel in-fiber technique for measuring of the Raman gain coefficient*, OFC 1997

[33] M. I. Skolnik, *Introduction to Radar Systems*, National Defence Industry Press, pp. 79-81 1992

[34] G. F. Stickley, D. A. Noon, M. Cherniakov, I. D. Longstaff, *Gated stepped-frequency ground penetrating radar*, Journal of Geophysics, Vol. 43, pp. 259-269, 2000

[35] Y. Tanabe, A. Takada, K. Ikawa and N. Bando, *An improvement of the accuracy in the distributed fiber Temperature measurement using Raman backscattering*, Optical Fiber Sensors, 44, pp.537-543, 1989

[36] John G. Proakis, Dimitris G. Manolakis, *Digital Signal Processing*, Prentice-Hall, 1996

[37] D. Garus, T. Gogolla, K. Krebber and F. Schliep, *Brillouin optical fiber frequency domain analysis for distributed temperature and strain measurements*, J. Lightwave Technology, 15, pp. 654-662, 1997.

[38] Zhang Zaixuan, Guo Ning, Yu, Xiangdong, Wu Xiaobaio, *The optimum design of 6km LD distributed optical fiber Raman photon sensor (DOFRPS) system*, SPIE, 3555, pp. 209-216

[39] Jiang Zou, Shu Wang, Zongkai Yang, *Distributed temperature measurement based on single-channel anti-Stokes light*, International Journal Infrared and Millimeter Waves, 21, pp. 793-803, 2000

[40] R. Feced, M. Farhadiroushan, V.A. Handerek, A.J. Rogers, *Advances in high resolution distributed temperature sensing using the time-correlated single photon counting technique*, IEE Proceedings Optoelectronics, Vol.144, pp.183-188, 1997

[41] A. Jensen, A. la Cour-Harbo, *Ripples in Mathematics, The Discrete Wavelet Transform*, Springer Verlag, 2001

[42] L. Pasti, B. Walczak, D. L. Massart, P. Reschiglian, *Optimization of signal denoising in discrete wavelet transform*, Elsevier, Chemometrics and Intelligent Laboratory Systems, Vol. 48, pp. 21-34, 1999

[43] P.J. Samson, *Analysis of the wavelength dependence of Raman backscatter in optical fibre thermometry*, Electronics Letters, 26, pp. 163-165, 1990

[44] S. N. Knudsen, M. O. Pedersen, L. Gruner-Nielsian, *Optimisation of dispersion compensating fibres for cabled long-haul applications*, Electronics Letters, Vol. 36, pp. 2067-2068, 2000

[45] Allan D. Kersey, Michael A. Davis, and D. G. Bellemore, *Development of fiber sensors for structural monitoring*, in Proc. SPIE Nondestructive Evaluation of Aging Bridges and Highways, Oakland,CA, June 1995, vol. 2456, p. 262.

[46] Atlas Steels Australia

[47] N. Gowripalan et al., Concrete in the 3rd Millenium, 21st Biennial Conference, Concrete Institute of Australia, Brisbane, July 2003, pp. 99-108.

[48] J. Voo, J.S. Foster, R.I. Gilbert, N. Gowripalan, *Design of disturbed regions in reactive powder concrete bridge girders*, in Proc. High Performance Materials in Bridges 2003, pp.117-127

[49] E. Dallaire, P.C. Aitcin, M. Lachemi, *High-performance powder*, Civil Engineering, vol. 68, pp. 48-51, (1998).

[50] R. Maaskant, T. Alavie, R.M. Measures, G. Tadros, S.H. Rizkalla, A. Guha-Thakurta, *Fiber-optic Bragg Grating Sensors for Bridge Monitoring*, Elsevier Cement and Concrete Composites, vol.19, pp. 21-33, (1997).

[51] M. A. Davis, D. G. Bellemore, and A. D. Kersey, *Structural strain mapping using a wavelength/time division addressed fiber Bragg grating array*, in Proc. SPIE 1994 2nd European Conf. Smart Struct. Materials, Glasgow, Scotland, Oct. 1994, vol. 2361, pp. 342-345.

[52] S.C. Tjin, Y. Wang, X. Sun, P. Moyo, J.M.W. Brownjohn, *Application of quasi-distributed fibre Bragg grating sensors in reinforced concrete structures*, Meas. Sci. Technol. Vol. 13, pp. 583-589, (2002).

[53] Y.B. Lin, K.C. Chang, J.C. Chern, L.A. Wang, *Packaging Methods of Fiber-Bragg Grating Sensors in Civil Structure Applications*, Sensors journal, Vol. 5, June 2005, pp.419-424

[54] J. Lauzon et al., *Implementation and characterization of fiber Bragg gratings linearly chirped by a temperature gradient*, Optics Letters, vol. 19, pp. 2027-2029, (1994).

[55] I. Alasaarela, P. Karioja, H. Kopola, *Comparison of distributed fiber optic sensing methods for location and quantity information measurements*, Optical Engineering, 41, pp.181-189, 2002

# List of Acronyms

```
APD      -     avalanche photo-diode
AS       -     anti-Stokes
CW       -     continuous wave
DCF      -     dispersion compensating fibre
DTS      -     distributed temperature sensor
DWDN     -     discrete wavelet denoising
EBPF     -     electrical band-pass filter
EDFA     -     Erbium-doped fibre amplifier
FBG      -     Fibre Bragg-grating
FFT      -     fast Fourier transform
GIMMF    -     graded-index multi-mode fibre
GVD      -     group-velocity dispersion
IDF      -     inverse dispersion fibre
IF       -     intermediate frequency
IFFT     -     inverse fast Fourier transform
IOFDR    -     incoherent optical frequency-domain reflectometry
LIDAR    -     light detection and ranging
LO       -     local oscillator
LD       -     laser diode
MMF      -     multi-mode fibre
NA       -     numerical aperture
NIR      -     near infra-red
OBPF     -     optical bandpass filter
OTDR     -     optical time-domain reflectometry
PCF      -     photonic crystal fibre
RADAR    -     radio detection and ranging
RAF      -     Raman fibre
```

```
RF      -   radio frequency
RPC     -   reactive powder concrete
SBS     -   stimulated Brillouin scattering
SIMMF   -   step-index multi-mode fibre
SMF     -   single-mode fibre
SNR     -   signal-to-noise ratio
SRS     -   stimulated Raman scattering
STD     -   standard deviation
TE      -   thermal-expansion effect
TL      -   tuneable laser
TO      -   thermal-optic effect
WDM     -   wavelength division multiplexing
```

# Appendix A

# Ph.D. Publications

The following publications have resulted from this Ph.D. project.

**Emir Karamehmedović**, Thomas Feuchter, and Palle Jeppesen, "Distributed Temperature Sensing by IOFDR with High Pump Power in Single-Mode Fibers", submitted to IEEE Journal of Lightwave Technology

**Emir Karamehmedović**, Gang-Ding Peng, Trevor Whitbread, Paul Childs and Nadarajah Gowripalan, "Strain Monitoring on the Experimental Reactive Powder Concrete Bridge at Shepherd's Creek using Fibre-optic Bragg grating sensors", submitted to IEEE Journal of Lightwave Technology

**Emir Karamehmedović**, Thomas Feuchter, and Palle Jeppesen, "Optimum pump power in distributed temperature sensing by spontaneous Raman scattering using IOFDR", Optics of High Technology Material Science, 2005, Kiev, Ukraine.

**Emir Karamehmedović**, Paul Childs, Trevor Whitbread, Allan C. L. Wong, N. Gowripalan, and Gang-Ding Peng, "Field Test of Strain Fluctuation in the Experimental Reactive Powder Concrete Bridge at Shepherd's Creek ", BGPP/ACOFT 2005, Sydney, Australia

**Emir Karamehmedović**, Thomas Feuchter, and Palle Jeppesen, "Ex-

tended range distributed fibre-optic temperature sensing using combined
SMF and DCF", Photonics 2004, Kochi, India.

**Emir Karamehmedović**, Ulrich Glombitza, Dino Simonits, "Fibre-
Optic Distributed Temperature Sensing Using IOFDR", European Work-
shop on Optical Fibre Sensors 2004, Santander, Spain, 2004

**Emir Karamehmedović**, Ulrich Glombitza, Dino Simonits, "Fiber-
optic Temperature Sencor Based on Incoherent Optical Frequency Do-
main Reflectometry", Photonics West 2004, San Jose, California, USA,
2004

**Emir Karamehmedović**, Ulrich Glombitza, "Fiber-Optic Tempera-
ture Sensor", iNANO Summer School, Fuglsøcentret, Denmark, 2003

# Appendix B

# Temperature profiles

Expressions for the temperature profile for different schemes are derived in this appendix.

Every temperature measurement system that is mentioned needs a reference point which is at a known, monitored temperature, as shown in figure D.4. The calibration constant $R_0$ is the ratio of the scattering coefficients of the two involved channels at the known temperature $T_0$.

### Raman Stokes and anti-Stokes scattering channels

Firstly, derivation of the configuration with Raman Stokes and anti-Stokes channels is derived. In Chapter 2 it is stated that the probability for spontaneous Raman scattering obeys

$$P_{aS}(T) \propto P_0 \frac{n_{aS}}{\lambda_{aS}^4} \cdot \left( e^{\frac{\hbar\omega_p}{k_B T}} - 1 \right)^{-1} \tag{B.1}$$

and

$$P_S(T) \propto P_0 \frac{n_S}{\lambda_S^4} \cdot \left( 1 - e^{\frac{-\hbar\omega_p}{k_B T}} \right)^{-1} \tag{B.2}$$

The calibration constant $R_0$ is defined as

$$R_0 \equiv \frac{P_{aS,T_0}}{P_{S,T_0}} \propto \frac{n_{aS}\lambda_S^4}{n_S\lambda_{aS}^4} \cdot e^{-\frac{\hbar\omega_p}{k_B T_0}} \tag{B.3}$$

Next, note that the backscattering from the fibre (obtained in case of IOFDR by inverse Fourier transform of frequency data) is

$$P_{aS}(z) \propto P_0 \cdot \chi_{aS}(z,T) \cdot e^{-(\alpha_P + \alpha_{aS})z} \tag{B.4}$$

and

$$P_S(z) \propto P_0 \cdot \chi_S(z, T) \cdot e^{-(\alpha_P + \alpha_S)z} \tag{B.5}$$

The ratio $R(z)$ of (B.4) and (B.5) is

$$R(z) \equiv \frac{P_{aS}(z)}{P_S(z)} \propto \frac{\chi_{aS}}{\chi_S} \cdot e^{(\alpha_S - \alpha_{aS})z} \tag{B.6}$$

From (B.4) and (B.5), it also follows that

$$R(z) \propto \frac{n_{aS}\lambda_S^4}{n_S\lambda_{aS}^4} \cdot e^{-\frac{\hbar\omega_p}{k_B T(z)}} \tag{B.7}$$

The pump power is factored out, and any fluctuation affects equally both channels. It is also assumed that the local fluctuations in the attenuation constants at $\lambda_S$ and $\lambda_{aS}$ are nearly same, so the difference $\alpha_S - \alpha_{aS}$ does not vary significantly.

Finally, using equations (B.6), (B.7) and (B.3) one can obtain the temperature profile

$$\frac{R(z)}{R_0} = e^{-\frac{\hbar\omega_p}{k_B}\left(\frac{1}{T(z)} - \frac{1}{T_0}\right)} \Leftrightarrow$$

$$\frac{1}{T(z)} - \frac{1}{T_0} = -\frac{k_B}{\hbar\omega_p} \cdot \ln\left(\frac{R(z)}{R_0}\right) \Leftrightarrow$$

$$T_{SaS}(z) = \left(\frac{1}{T_0} + \frac{k_B}{\hbar\omega_p}\ln\left(R_0 \cdot R^{-1}(z)\right)\right)^{-1}$$

$$T_{SaS}(z) = \left(\frac{1}{T_0} + \frac{k_B}{\hbar\omega_p}\ln\left(C_0 \cdot \frac{\lambda_S^4 n_{aS}}{\lambda_{aS}^4 n_s}\frac{\chi_s(z)}{\chi_{aS}(z)} \cdot e^{-(\alpha_S - \alpha_{aS})z - \frac{\hbar\omega_p}{k_B T_0}}\right)\right)^{-1} \tag{B.8}$$

where $C_0$ is another calibration constant.

## Rayleigh and Raman anti-Stokes scattering channels

Rayleigh scattering may be used to substitute one of the spontaneous Raman channels. Rayleigh scattering is linear, and scales as

$$P_R(z) \propto P_0\frac{n_R}{\lambda_R^4}e^{-2\alpha_P z} \tag{B.9}$$

The procedure is the same as above. $R_0$ for the Rayleigh-anti Stokes (RAS) configuration is found

$$R_0 \equiv \frac{P_{aS,0}}{P_{R,0}} \propto \frac{n_{aS}\lambda_R^4}{n_R\lambda_{aS}^4} \cdot \frac{1}{e^{\frac{\hbar\omega_p}{k_B T_0}} - 1} \tag{B.10}$$

The distributed scattering ratio $R(z)$ is

$$R(z) \equiv \frac{P_{aS}(z)}{P_R(z)} \propto \frac{\chi_{aS}\lambda_R^4}{n_R} \cdot e^{(\alpha_P - \alpha_{aS})z} = \frac{n_{aS}\lambda_R^4}{n_R\lambda_{aS}^4} \cdot \frac{1}{e^{\frac{\hbar\omega_p}{k_B T(z)}} - 1} \tag{B.11}$$

Again, the temperature profile is found from $R(z)/R_0$

$$
\begin{aligned}
\frac{R(z)}{R_0} &= \frac{e^{\frac{\hbar\omega_p}{k_B T_0}} - 1}{e^{\frac{\hbar\omega_p}{k_B T(z)}} - 1} \Leftrightarrow \\
e^{\frac{\hbar\omega_p}{k_B T(z)}} &= 1 + \frac{R_0}{R(z)}(e^{\frac{\hbar\omega_p}{k_B T_0}} - 1) \Leftrightarrow \\
T_{RaS}(z) &= \left(\frac{k_B}{\hbar\omega_p} \ln\left(R_0 \cdot \chi_{aS}^{-1}(z) \cdot e^{(\alpha_{aS} - \alpha_P)z}\left(e^{\frac{\hbar\omega_p}{k_B T_0}} - 1\right) + 1\right)\right)^{-1} \tag{B.12}
\end{aligned}
$$

**Raman Stokes and Rayleigh scattering channels**

For the Stokes-Rayleigh (SR) configuration, the probability function for the Stokes scattering is inserted in stead of the anti-Stokes.

$$R_0 \equiv \frac{P_{S,0}}{P_{R,0}} \propto \frac{n_S\lambda_R^4}{n_R\lambda_S^4} \cdot \frac{1}{1 - e^{-\frac{\hbar\omega_p}{k_B T_0}}} \tag{B.13}$$

$$R(z) \equiv \frac{P_S(z)}{P_R(z)} \propto \frac{\chi_S\lambda_R^4}{n_R} \cdot e^{(\alpha_S - \alpha_{aS})z} = \frac{n_S\lambda_R^4}{n_R\lambda_S^4} \cdot \frac{1}{1 - e^{-\frac{\hbar\omega_p}{k_B T(z)}}} \tag{B.14}$$

Finally, it is straightforward to obtain

$$T_{SR}(z) = \left(-\frac{k_B}{\hbar\omega_p} \ln\left(1 - R_0 \cdot \chi_S^{-1}(z) \cdot e^{(\alpha_S - \alpha_P)z}\left(1 - e^{-\frac{\hbar\omega_p}{k_B T_0}}\right)\right)\right)^{-1} \tag{B.15}$$

| c | $3 \cdot 10^8 m/s$ |
|---|---|
| h | $6.62618 \cdot 10^{-34}$ |
| $\hbar$ | $h/(2\pi) = 1.0545893 \cdot 10^{-34}$ |
| $k_B$ | $1.38066 \cdot 10^{-23}$ |
| q | $1.602 \cdot 10^{-19}$ |

**Table B.1:** Table of natural constants used in the thesis.
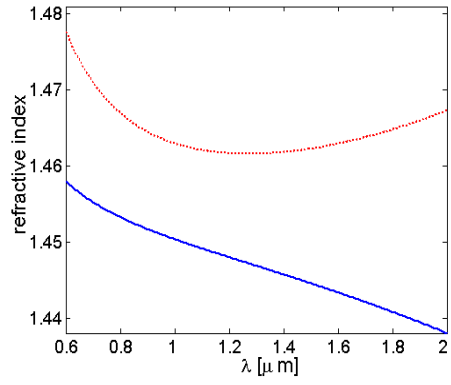
# Appendix C

# Sellmeier's Approximation

The Sellmeier's equation gives a good approximation to the refractive index of silica [9] in its transparent region:

$$\tilde{\epsilon}(\omega) = n^2(\omega) = 1 + \sum_{i=1}^{m} \frac{B_i \omega_i^2}{\omega_i^2 - \omega^2} = 1 + \sum_{i=1}^{m} \frac{B_i}{1 - \left(\frac{\lambda_i}{\lambda}\right)^2} \qquad (C.1)$$

where $\omega_i$ frequencies are atomic or molecular resonant frequencies that constitute the dielectric. $B_i$ are constants that weigh the oscillator strength, the first three of which can be found in the following table.

| Oscillator strengths ($B_i$) | Corresponding wavelengths ($\lambda_i$) |
|---|---|
| 0.6961663 | 68.4$nm$ |
| 0.4079426 | 116.24$nm$ |
| 0.8974794 | 9.896$\mu m$ |

Using the formula (C.1), the dependence of refractive index of pure silica in the wavelength range 0.6$\mu m$ to 2$\mu m$ is plotted in Figure C.1. The group index, defined as $n_g = n + \omega \frac{dn}{d\omega}$, is also plotted in the figure.
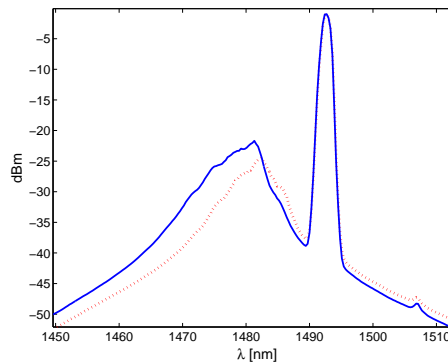
**Figure C.1:** Refractive index and group refractive index in pure fused silica.

# Appendix D

# The optical module

In this appendix, the scheme of the optical module is presented. Some laser characteristics and wavelength spectra are illustrated.

Figure D.1 shows the change in the emission spectrum of the laser diode when the temperature of the diode changes.



**Figure D.1:** Emission spectrum of the laser diode at $22^oC$ and $28^oC$. Side-lopes must be minimised - the temperature is raised.

The L-I curve of the laser diode is in figure D.2.

When the laser-diode is directly modulated, its output power varies with the modulation frequency. The output spectra of the laser at CW and $50MHz$ are shown in figure D.3.
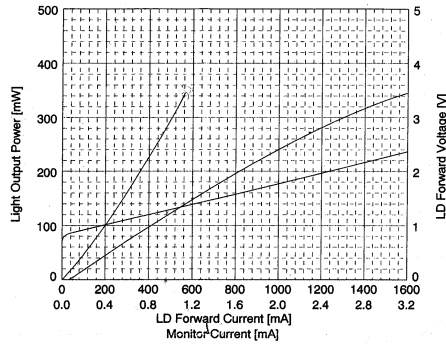
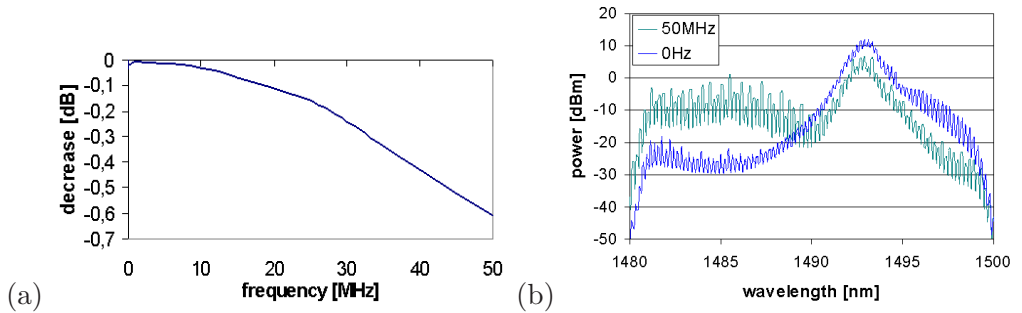**Figure D.2:** L-I curve of the laser used in the experimental DTS.
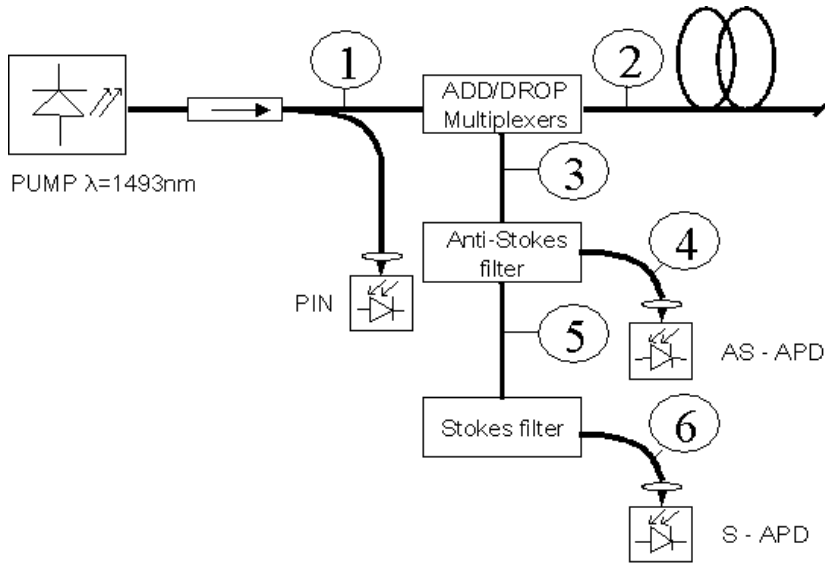


**Figure D.3:** (a) The dependency of the output power on the modulation frequency (b) Change in the spectrum of emitted light.

A more detailed scheme of the optical module is in figure D.4. The relevant signals at marked spots are shown in their respective graphs. Furthermore, there is a list of the actual components used in the module.

**Figure D.4:** The setup of the optical module of the SMF prototype system.
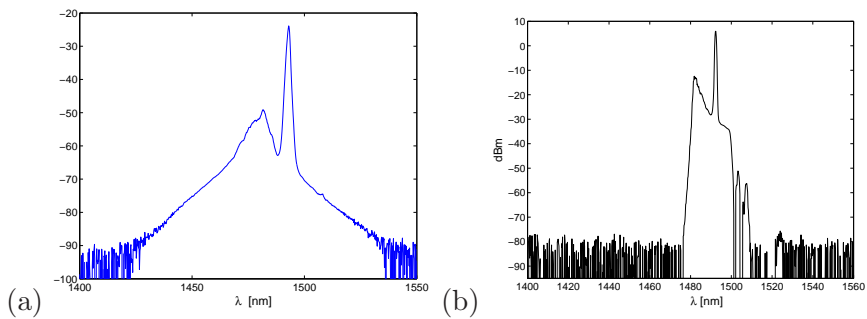


**Figure D.5:** (a) Point 1: The input spectrum to the passive filter module (b) Point 2: The pump launched into the fibre.
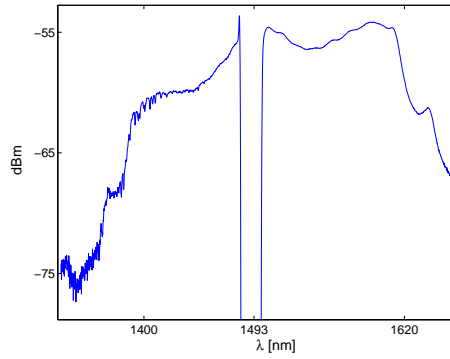
**Figure D.6:** Point 3: Raman Stokes and anti-Stokes signals - Rayleigh scattering from the pump is removed.
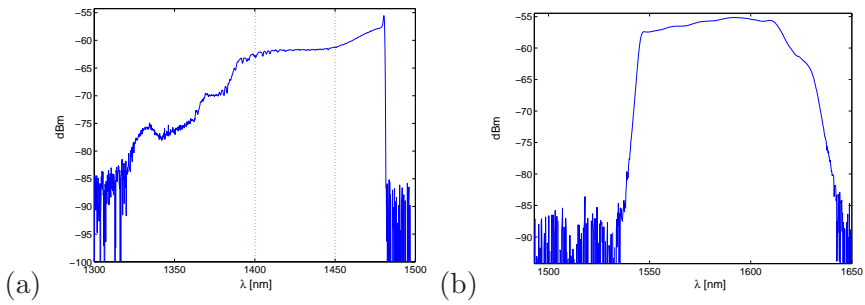


**Figure D.7:** (a) Point 4: Raman anti-Stokes signal after the filter sent to the APD (b) Point 6: Raman Stokes signal after filtering sent to the APD.

# Appendix E

# Dispersion measurements

Dispersion measurement in a fibre was conducted by sending a *ps* pulse at several wavelengths through a length of optical fibre, and measuring the time it takes for the pulse to propagate through the fibre. A tuneable laser (Photonetics TunicsPlus) in combination with an electro-optic modulator provided the *ps* pulses. The time delay was measured on an oscilloscope. The dispersion is deduced from the measurements

$$D_\lambda = \frac{\delta_{\lambda_1} - \delta_{\lambda_2}}{L\Delta\lambda_D} \tag{E.1}$$

where $\delta_{\lambda_1}$ and $\delta_{\lambda_2}$ are time delays at the two wavelengths $\lambda_1$ and $\lambda_2$, $L$ is the fibre length, and $\Delta\lambda_D = |\lambda_1 - \lambda_2|$ is the difference in the wavelengths of the consecutive measurement points.

Dispersion was measured on $24km$ SMF and $7.8km$ GIMMF. The results are presented in tables E.1 and E.2, and in figure E.1.

| Wavelength | Delay | Relative delay | Relative delay/km | Dispersion |
|------------|-------|----------------|-------------------|------------|
| $[nm]$ | $[\mu s]$ | $[ns]$ | $[ns/km]$ | $[ps/(km\ nm)]$ |
| 1500 | 124.1755 | 0 | 0 | 15.4 |
| 1520 | 124.1832 | 7.7 | 0.31 | 16.4 |
| 1540 | 124.1914 | 15.9 | 0.64 | 17.2 |
| 1560 | 124.2000 | 24.5 | 0.98 | 18.6 |
| 1580 | 124.2093 | 33.8 | 1.35 | // |

**Table E.1:** Dispersion measurements in $24km$ single-mode fibre.

| Wavelength | Delay | Relative delay | Relative delay/km | Dispersion |
|------------|-------|----------------|-------------------|------------|
| $[nm]$ | $[\mu s]$ | $[ns]$ | $[ns/km]$ | $[ps/(km\ nm)]$ |
| 1500 | 38.21225 | 0 | 0 | 14.4 |
| 1520 | 38.21450 | 2.25 | 0.29 | 16.7 |
| 1540 | 38.21710 | 4.85 | 0.62 | 17.3 |
| 1560 | 38.21980 | 7.55 | 0.97 | 18.9 |
| 1580 | 38.22275 | 10.5 | 1.35 | // |

**Table E.2:** Dispersion measurements in $7.8km$ graded-index multi-mode fibre.
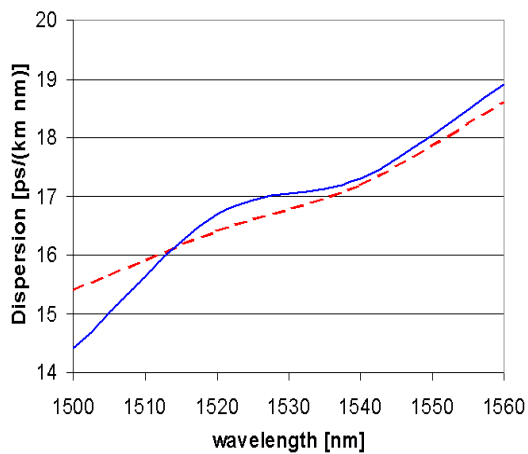
**Figure E.1:** Measured dispersion of a $25km$ SMF (dashed) and a $7.7km$ GIMMF (solid).

# Appendix F

# Test of modulation formats

Setup for testing the modulation formats is shown figure F.1. DTS sends a sine-modulated pump wave which is detected by a PIN diode. Signal from the diode is used to generate a sine wave or a square wave of variable duty cycle, with exactly the same frequency as the pump laser. A laser with $\lambda_s = 1550nm$ that simulates Raman Stokes backscattering from the sensor fibre, is directly modulated by the regenerated signal from the PIN.
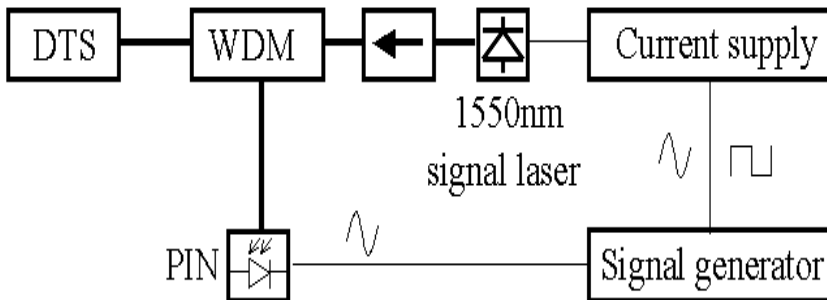


**Figure F.1:** Setup of the experiment testing modulation formats.

Due to limitations od the laser current driver, PIN photo-diode, the electrical circuitry for signal reshaping, the tested modulation frequency is set to low $f_m = 18kHz$. The standard deviation of the Stokes signal is measured and compared for the three cases. Namely sine-modulation, square wave modulation with duty cycle 50%, and, what was found to be the optimal for the modelled setup, square wave modulation with

duty cycle of 37%. Results are in figures F.2, F.3 and F.4.
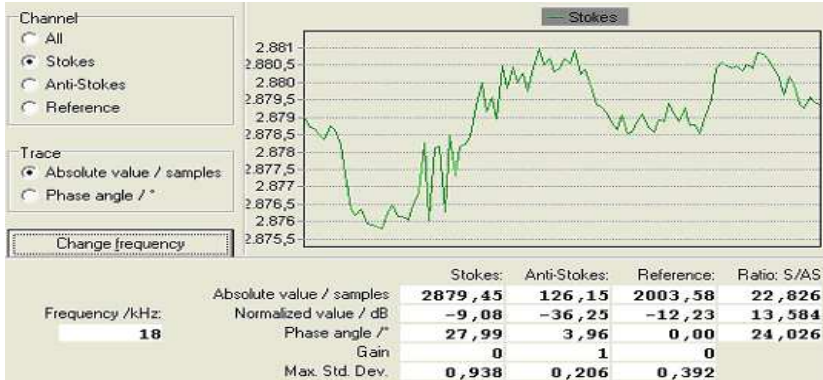


**Figure F.2:** Samples of sine-modulated signal over a period of time. Note the maximum standard deviation of the Stokes channel is 0.938.



**Figure F.3:** Samples of square-modulated signal with 50% duty cycle over a period of time. Maximum standard deviation of the Stokes channel is 0.589.

Because the modulation frequency is very low, the modulated signal is not superimposed on a constant DC level. The measurements are very unstable, but do show qualitative decrease in the standard deviation of the detected signal when square wave modulation is applied.

Problems with interference of higher order harmonics were also evident. At the modulation frequency $f_m = 11kHz$, the standard deviation of frequency response was exceptionally higher than at other frequencies,
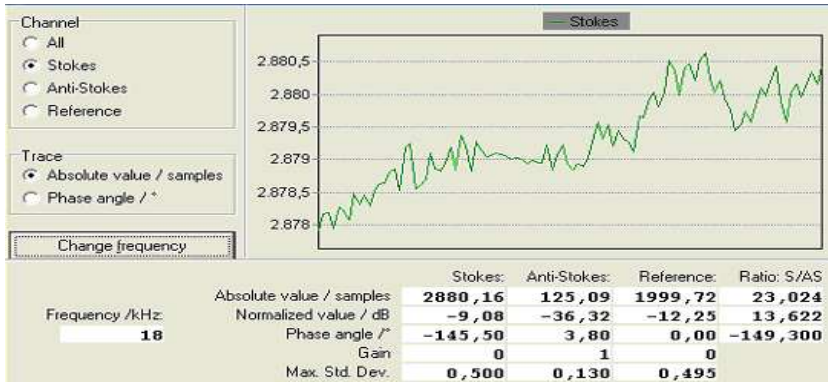
**Figure F.4:** Samples of square-modulated signal with 37% duty cycle over a period of time. Maximum standard deviation of the Stokes channel is 0.500.
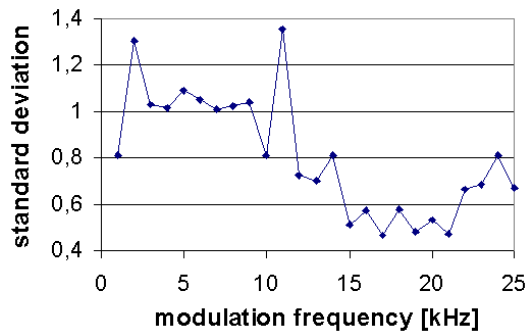
as shown in figure F.5. An increase at $22kHz$ is also visible. At frequencies higher than approximately $30kHz$, there was a significant relative difference between the modulation frequency of the pump laser and the reproduced frequency of the signal laser, resulting in a slow sinusoidal variation of the samples, thus making the long-term STD measurements invalid.



**Figure F.5:** Standard deviation of signal samples as a function of modulation frequency. Due to interference of different harmonics, there is a local peak at $11kHz$.

# Appendix G

# Matlab Code: Implementation of SSFM

This is the main program for simulation of the detected back-scattering in a fibre whose characteristics are loaded form a file. The program is built in modules to make the recurring calculations and procedures faster.

```
% Statistics on computer model of temperature calculations
% The module finds the standard deviation of temperature
% when different filtering is used

intensity          % calculates the ideal frequency response
APDgain            % calculates the SNR of desired setup

clear Tn; clear Ta; clear Tw; clear TWW; clear TAW; clear TT;

runda=60;               % number of samples for STD
aver=4;                 % number of averagings
Tn=zeros(runda,aa);
Ta=zeros(aver,aa);

for ii=1:runda

    for gg=1:aver
```

```matlab
  intensityI;
  Ta(gg,:)=T(aa+1:2*aa);
  Tw(gg,:)= wden(T(aa+1:2*aa),'heursure','s','mln',1,'db1');
  end

  Tn(ii,:) = mean(Ta);
  TM(ii,:) = median(Ta);

 TWW(ii,:) = mean(Tw);
 TAW(ii,:) = wden(Tn(ii,:),'heursure','s','mln',1,'db1');
end

ar = mx.*(exp(- i*ph ));
arS = mxS.*(exp(- i*phS ));
arc = conj(ar);
arcS = conj(arS);
ars =[ fliplr(arc) ar(2:aa) 0];
ab=length(ars)
arsS =[ fliplr(arcS) arS(2:aa) 0];

intensityII    % calculates the temperature profile

trend=T(aa+1:2*aa);
meanTemp=mean(Tn);
medianTemp=median(TM);

stdevTemp=std(Tn);
stdevTempTT=std(TT);
stdevTempAW=std(TAW);
stdevTempMed=std(TM);

figure
hold on

 plot(zz(aa+1:2*aa), mean(Tn),'k')
 plot(zz(aa+1:2*aa), mean(TAW),'b')
 plot(zz(aa+1:2*aa), mean(TT),'r')
```

```
figure
hold on
plot(zz(aa+1:2*aa), stdevTempMed,'m')
plot(zz(aa+1:2*aa), stdevTemp,'k')
plot(zz(aa+1:2*aa), stdevTempTT,'r')
plot(zz(aa+1:2*aa), stdevTempAW,'b')

figure
hold on
plot(stdevTemp./stdevTempW,'r')
plot(stdevTemp./stdevTempAW,'b')

% better on average by a factor of:
mean(stdevTemp./stdevTempAW)

 figure
 waterfall(zz(aa+1:2*aa), linspace(1,10,10),  X(1:10,:))
```

This module calculates the ideal frequency response with or without a simulated hot-spot.

```
% This Program calculates amplitudes of the backscattering
% for all applied frequencies.

clear mx; clear mxS; clear ph; clear phS;

sm_fiber;               % load the sensing fiber parameters

da=20000;               % time array length
c=3e8;                  % velocity of light in free space
m=1; 0.9;               % modulation index
bS=nS/c;                % propagation constants
bP=nP/c; baS=naS/c; b=(bP+baS); bSS=(bP+bS);

rez = 3;1;              % spatial resolution
d = 21;                 % length of the hot-spot
```

```
al=(ap+aas)*ones(1,da); alS=(ap+as)*ones(1,da);

wmax=2*pi*c/(4*nP*rez);
N=L/rez;
arw= 0 : wmax/N : wmax - wmax/N;
aa=length(arw)

hs = 11500;          % placement of the hot-spot

chi = [ones(1,hs) ones(1,d) ones(1,L-hs-d)];

chi1=1; chi2=1.1; chi1S=1; chi2S=1.01;

fani2= -1./al.*(exp(-al*L)-1);
nfun = 1./(al).*(1-exp(-al*L));
mx(1)= nfun(1);
nfun= 1./(alS).*(1-exp(-alS*L));
mxS(1) = nfun(1);
ph(1)=0; phS(1)=0;

Lact=10000;     % actual fibre length

for f=2:aa
    frek=arw(f);
    omg=ones(1,da)*frek;
    t=linspace(0,2*pi/frek-2*pi/frek/da,da);
     ob=omg.*b;
     obS=omg.*bSS;
     ot=omg.*t;
% *** no hot-spot ***
%  nfun = - m./(al.^2 + ob.^2).*(exp(-al*Lact).*
     (al.*cos(ot-ob*Lact) + ob.*sin(ot-ob*Lact)) -
     (al.*cos(ot)+ob.*sin(ot)) );
%  nfunS = - m./(alS.^2 + obS.^2).*(exp(-alS*Lact).*
     (alS.*cos(ot-obS*Lact) + ob.*sin(ot-obS*Lact)) -
     (alS.*cos(ot)+obS.*sin(ot)) );
% ***
```

```
% *** hot-spot case ***
 nfun = chi1*(m./(al.^2 + ob.^2).*(-exp(-al*hs).*(al.*cos(ot-ob*hs)
    + ob.*sin(ot-ob*hs))+(al.*cos(ot)+ob.*sin(ot)) ))
    + chi2*(m./(al.^2 + ob.^2).*(exp(-al*hs).*(al.*cos(ot-ob*hs)
    + ob.*sin(ot-ob*hs)) - exp(-al*(hs+d)).*(al.*cos(ot-ob*(hs+d))
    + ob.*sin(ot-ob*(hs+d))) )) + chi1*(m./(al.^2 + ob.^2)
    .* (exp(-al*(hs+d)).*(al.*cos(ot-ob*(hs+d))+ob.*sin(ot-ob*(hs+d)))
    - exp(-al*Lact).*(al.*cos(ot-ob*Lact)+ob.*sin(ot-ob*Lact)) ));
 nfunS = chi1S*(m./(alS.^2 + obS.^2).*(-exp(-alS*hs).*(alS.*cos(ot-obS
    + obS.*sin(ot-obS*hs))+(alS.*cos(ot)+obS.*sin(ot)) ))
    + chi2S*(m./(alS.^2 + obS.^2).*(exp(-alS*hs).*(alS.*cos(ot-obS*hs)
    + obS.*sin(ot-obS*hs)) - exp(-alS*(hs+d)).*(alS.*cos(ot-obS*(hs+d))
    + obS.*sin(ot-obS*(hs+d))) )) + chi1S*(m./(alS.^2 + obS.^2)
    .* (exp(-alS*(hs+d)).*(alS.*cos(ot-obS*(hs+d))+obS.*sin(ot-obS*(hs+
    - exp(-alS*Lact).*(alS.*cos(ot-obS*Lact)+obS.*sin(ot-obS*Lact)) ));
% ***

mx(f) = max((nfun)); mxS(f)= max((nfunS));

ph(f) = find(nfun>=mx(f));      % finds the phase of the signal
phS(f)= find(nfunS>=mxS(f));
end

mxS=mxS*chiS/mxS(1); mx=mx*chiAS/mx(1);

ph = 2*ph*pi/da; phS = 2*phS*pi/da;

% ****************************************
% ** Program continues in "intensityI.m" **
% ****************************************
% intensityI
```

The following module adds the noise, filters and completes the arrays
simulating the frequency response.

```
% ** addition of noise      **
 noiseAS = (mx./SNR).*randn(1,aa);
```

```
 noiseS = (mxS./SNRS).*randn(1,aa);
 mxN = (mx + noiseAS).*Coas(1:aa);
 mxSN = (mxS + noiseS).*Co(1:aa);
% ** Amplitude noise added **

% ** Filter function **
 cosfil;
% ** Filter end      **

ar = mxN.*(exp(-i*ph ));
arS = mxSN.*(exp(-i*phS ));

arc = conj(ar);
arcS = conj(arS);

ars =[0 fliplr(arc) ar(2:aa)];
ab=length(ars);
arsS=[0fliplr(arcS) arS(2:aa)];

% the program continues in
intensityII
```

This module calculates the temperature profile after the backscattering arrays are defined.

```
clear T;

zz_s = abs(arw(1)-arw(2));
zz_sp = 1/zz_s*(wmax)*rez;
zz = -zz_sp+rez : rez : zz_sp; bla=length(zz);

ft = (fftshift(ifft(ars)))/rez;
ftS = (fftshift(ifft(arsS)))/rez;

dkd = floor(Lact/rez+1);
 comp=ones(1,bla);
 compS=ones(1,bla);
 comp(bla/2-dkd+1:bla-bla/2+dkd)=
```

```
    exp(-(zz(bla/2-dkd+1:bla-bla/2+dkd)).*al(1));
 compS(bla/2-dkd+1:bla-bla/2+dkd)=
    exp(-(zz(bla/2-dkd+1:bla-bla/2+dkd)).*alS(1));

bcAS = abs(ft)./comp;
bcS = abs(ftS)./compS;

% ** Constants **
k=1.38066e-23; omgp=13.2e12*2*pi; hss=6.62618e-34/2/pi;
C2=k/(hss*omgp); R0 = bcAS(aa+100)/bcS(aa+100);
% ** End Const

% Temperature is calculated and plotted
T = 1./(1/300 + C2*log(bcS./bcAS.*R0 ) ) - 273;
plot(zz(aa+1:2*aa), (T(aa+1:2*aa)),'k')
```

An example of file containing fibre characteristics:

```
%%%%%%%%%%%%%%%%%%%%%%%%%%%%%%%%%%%%%%%%%%%%%%%%%%%%%
% FIBER CHARACTERISTICS OF SM FIBER FOR THE SIMULATION %
%%%%%%%%%%%%%%%%%%%%%%%%%%%%%%%%%%%%%%%%%%%%%%%%%%%%%

ap = 0.2e-3/4.343;    % attenuation of pump in dB/m
as = 0.18e-3/4.343;   % attenuation of Stokes in dB/m
aas = 0.28e-3/4.343;  % attenuation of anti-Stokes in dB/m

nS = 1.45; 1.4638;    % refractive indices
naS = 1.45;%+1e-3;
nP = 1.45; 1.4644;

L = 8192;             % fiber length

chiS = 5.18031E-10;   % Stokes scattering coefficient
chiAS = 1.42483E-10;  % anti-Stokes scattering coefficient
```

SNR is calculated here using typical parameters of an InGaAs APD:

```
% Finds: Optimum M for an APD and
% calculates SNR for S and AS
```

```matlab
clear SNR; clear SNRS;
P0=100e-3;
kA = 0.5;
kB = 1.38066*1e-23;
T = 300;
Fn = 1;             % noise figure
q = 1.602*1e-19;
RL = 2000;          % Load resistance on AS
RLS = 2000;         % Load resistance on S
Id = 2e-9; R = 0.84; RS = 0.84;
Pin = P0*chiAS/(ap+aas)*(1-exp(-(ap+aas)*L))/2;
PinS = P0*chiS/(ap+as)*(1-exp(-(ap+as)*L))/2;
Psin = Pin *(mx)./mx(1);
PsinS = PinS *(mxS)./mxS(1);


Df = 160;
M = 13;
MS = 8;
Fa = kA*M + (1-kA)*(1-1/M) % excess noise factor
FaS = kA*MS + (1-kA)*(1-1./MS) %excess noise factor

opt = inline('kA*Mo.^3 + (1-kA).*Mo
    - 4*kB*T*Fn./(q*RL*(R*Pin+Id))');

Ns = (2*q*M*M*Fa.*(R*Pin + Id)*Df).*RL.^2;
NsS = (2*q*MS*MS*FaS*(RS*PinS + Id)*Df)*RLS.^2;

Nth = ((4*kB*T/RL)*Df*Fn)*RL.^2;
NthS = ((4*kB*T/RLS)*Df*Fn)*RLS.^2;

Nv = (4.8e-9).^2*Df; Ni = (1.3e-15).^2*RL^2*Df;

N = sqrt(Ns + Nth + Nv + Ni);
NS = sqrt(NsS + NthS + Nv + Ni);

SNR = (RL*R*M*Psin)./(N);
```

```
SNRS = (RLS*RS*MS.*PsinS)./(NS);

SNRs = (RL*R*M*Psin)./(Ns);
SNRth = (RL*R*M*Psin)./(Nth);

dB = 20*log10(SNR); dBS = 20*log10(SNRS);

  plot(arw/2/pi,dB,'b'), hold on
  plot(arw/2/pi,dBS,'r')
```

# Appendix H

# Installation of FBG sensors

This appendix describes some more practical issues concerning the FBG sensor. Encapsulation, mounting of the sensors and some details about the control software are presented.

## H.1    Encapsulation of the gratings

The FBGs need an adequate encapsulation before they can be installed on a smart structure. Stainless steel tubes can be used to house sensors which are designed for strain measurements on concrete buildings [53]. The packaging has to protect the fibre from breaking and chemical dissolving, and at the same time allow the sensor to perform repeatable measurements. Furthermore, it has to make it possible for the sensor to withstand mechanical stress.

The utilised design confines the fibre into the gap between three stainless-steel (SS) rods (or wires) as sketched in figure H.1. Rods with diameter of $1.5mm$ allow the maximum fibre diameter of $464\mu m$. This gives enough space to accommodate the coated fibre, and at the same time keeps the fibre straight and in well-defined place. The rods are rigid enough to protect the fibre from braking.

The encapsulation design is shown in figure H.3. On two stainless steel $0.80mm$ thick plates, two stainless steel $170mm$ long, $\phi = 1.5mm$ rods are soldered so that they are tightly next to each other. The fibre with $50mm$ long FBG is put into the gap created by the two rods. Firstly, one end of the fibre is glued (Loctite 480) to secure the position,
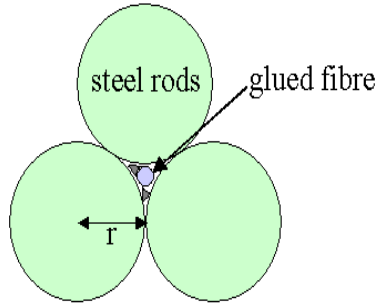
**Figure H.1:** Cross-section of encapsulated fibre with inscribed FBG. The fibre is glued between the three stainless-steel rods.

and then entire gap is filled with the glue. The fibre must be stretched at this stage. The third stainless steel rod is finally put in position to hold the fibre. The glue is hard and forces the fibre to follow the expansion as well as contraction of the steel rods.

Both ends are fixed with epoxy glue (Araldite), using a plastic tube. Hot-shrink tubes are put, so that transition from the (yellow) fibre protection to the glued section is smooth.
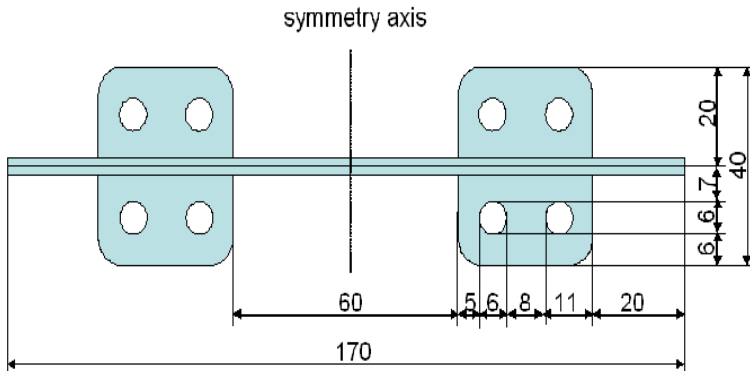


**Figure H.2:** Top view of the stainless steel holder with dimensions.

Four such sensor-heads with non-overlapping Bragg wavelengths are made and connected in line.
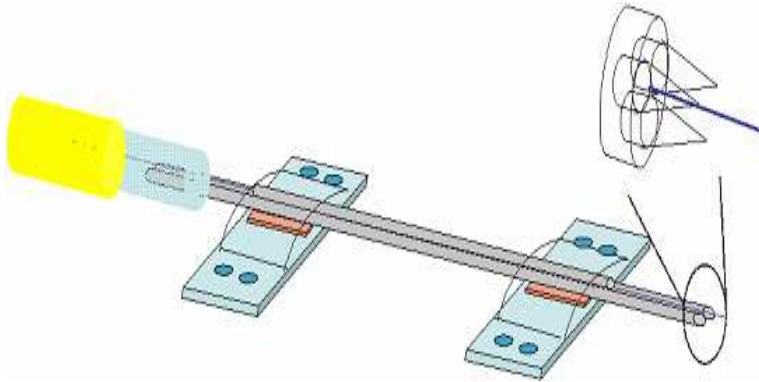
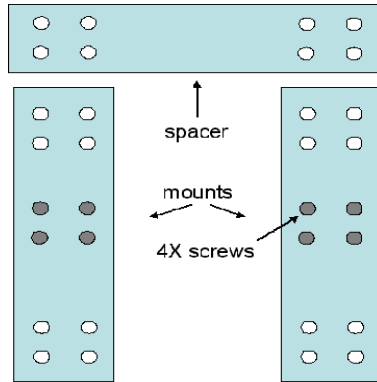**Figure H.3:** Sketch of the FBG sensor head.



**Figure H.4:** Photograph of the assembled sensor.

## H.2   Installation of the sensor array

In order to install the sensor on a bridge, and later be able to remove and reuse the sensor-head, mounts (or holders) for the sensors are made. A sketch of the holders is in figure H.5. The steel mounts are glued on marked places to the concrete structure. After gluing, FBG sensors are screwed onto the mounts. These holders remain on the structure even after the sensor is removed.

The spacer makes sure that the sensor will fit on the mount. Once the mounts are glued in place, the spacer is removed. The mounts have four screws each soldered onto them so the FBG sensor can be fastened to the mounts by nuts in place of the spacer. It is the friction between the mounts and the sensor pods that holds the sensor in place. Therefore, the contacting surfaces are made rough. Four screws on each side proved to be enough to fix the sensor.

**Figure H.5:** Sketch of the mounts used to install FBG sensors on concrete structure.



**Figure H.6:** Installing the mounts on a bridge-girder.

The first field trial of the described sensor is conducted on April 15, 2005, on a bridge made of novel reactive powder concrete at Shepherd's Creek, Lake Macquarie, NSW. An array of four FBG sensors is installed in the middle of a girder of the bridge. The sensors are installed as shown in figure H.7. FBG2 is not attached at both ends and acts as a temperature sensor. The temperature is assumed to be same at all four points, so that it is possible to compensate temperature effects on the other three sensors.
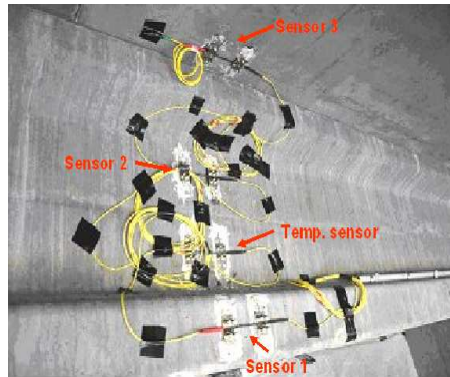
Figure H.7: Surface-mounted sensor array at the Shepherd's Creek Bridge.

## H.3  Flow diagram

Flow-diagram of the LabView program is given in figure H.8.